POLYTECHNIC OF MILAN
Faculty of Engineering
Course of Nuclear Engineering




The LEP Spectrometer Project

# HIGH ACCURACY MAGNETIC FIELD MAPPING OF THE LEP SPECTROMETER MAGNET

Federico Roncarolo, Academic Year 1999-2000

# Abstract

The Large Electron Positron accelerator (LEP) is a storage ring which has been operated since 1989 at the European Laboratory for Particle Physics (CERN), located in the Geneva area.
It is intended to experimentally verify the Standard Model theory and in particular to detect with high accuracy the mass of the electro-weak force bosons. Electrons and positrons are accelerated inside the LEP ring in opposite directions and forced to collide at four locations, once they reach an energy high enough for the experimental purposes. During head-to-head collisions the leptons loose all their energy and a huge amount of energy is concentrated in a small region. In this condition the energy is quickly converted in other particles which tend to go away from the interaction point.
The higher the energy of the leptons before the collisions, the higher the mass of the particles that can escape. At LEP four large experimental detectors are accommodated. All detectors are multi purpose detectors covering a solid angle of almost $4\pi$ .

The first period of operation of LEP (1989-1995) has been dedicated to the scan of the Z boson energy range, and the electrons and positrons beams were accelerated up to about 45 GeVper beam (see section 1.3.1). Since the end of 1995 LEP is devoted to operate at higher energies, up to more than 100 GeVper beam in the 1999-2000 runs. It was thus possible to investigate the W boson properties and the Higg's particle existence, in case its mass reveals to be at this energy level.

The types of event (i.e. the fundamental particles) which can be detected depends on the lepton energy before colliding (see Fig. 1.2). The particle beams energy calibration is thus a focal point for a successful operation of the collider.
During normal operation electrons and positrons are bent inside the ideal circular trajectory by mean of a number of dipole magnets. The energy of the leptons depends on the total dipole field along their trajectory.
The bending field around LEP is monitored by Nuclear Magnetic Resonance (NMR) probes which sample the field in twenty locations. Such measurements provide part of the data for the energy calibration model (see chapter 2).
In 1999 a spectrometer has been installed in a section of the LEP ring as a new tool for the beam energy determination. The spectrometer layout mainly consist in an iron-core bending magnet and six Beam Position Monitor (BPM) stations.

The main subject of this thesis work relates to the design, development and application of a special system which is able to measure with high accuracy the total integral field of the spectrometer bending dipole.
The dissertation begins with a short introduction to CERN and its accelerator complex. Further on the LEP collider is described in detail and the basics of the beam energy calibration are included.
Chapter 3 describes the LEP spectrometer, starting from the concept and layout, outlining the dipole magnet characteristics. The chapter ends with the presentation of some measurements

performed on the LEP injection magnets in order to investigate the possible thermal effects to be foreseen on the spectrometer magnet.
Chapter 4 introduces basics concepts about magnetic measurements techniques, mainly concentrating on the NMR theory and application.
Chapter 5 provides the detailed description of our measurement setup based on a travelling mole equipped with magnetic field detectors and monitored with a laser interferometer. The design, realization and test of the whole system is considered.
The following chapter gives the results of the first field mapping with the mole system, performed on an standard LEP iron-concrete core dipole, located in a laboratory at ground level.
Chapter 7 finally describes the mapping campaign on the LEP spectrometer dipole magnet with a full analysis of the achieved results.

# Contents

# Chapter 1

# Preface

## 1.1 Introduction to CERN

CERN is the European Organization for Nuclear Research, the world's largest particle physics center. Founded in 1954, the laboratory was one of Europe's first joint ventures, and has become a shining example of international collaboration. From the original 12 signatories of the CERN convention, membership has grown to the present 20 Member States.
CERN explores what matter is made of, and what forces hold it together. The Laboratory provides state-of-the-art scientific facilities for researchers to use. These are accelerators which accelerate tiny particles to a fraction under the speed of light, and detectors to make the particles visible.

## 1.2 The Accelerator Complex

The subject of this thesis regards the LEP storage ring. In order to show how LEP is linked to the other CERN accelerators, an overview of the accelerator complex and an outlook at the future of this research facility is given.
In Fig. 1.1 the accelerator configuration is displayed. The *Linear Injector for LEP* (LIL) and the *Electron Positron Accumulation* (EPA) are a linear accelerator and a circular storage ring respectively, which act as electron-positrons pre-accelerators before injecting the particles in the Proton Synchrotron.

#### The Proton Synchrotron

The PS is the oldest of CERN's accelerators. It was commissioned in 1959 and it is working continuously ever since. It has a diameter of 200 m and maximum electron beam energy of 28 GeV. Designed to accelerate protons it has been modified during the years to fit the different exigencies of the activities at CERN, related to the different experiments and colliders built after it.
Today the PS can accelerate all the stable and electrically charged particles (electrons, protons), their anti-particles (positrons and anti-protons) and some kinds of heavy ions (oxygen, sulfur, lead).

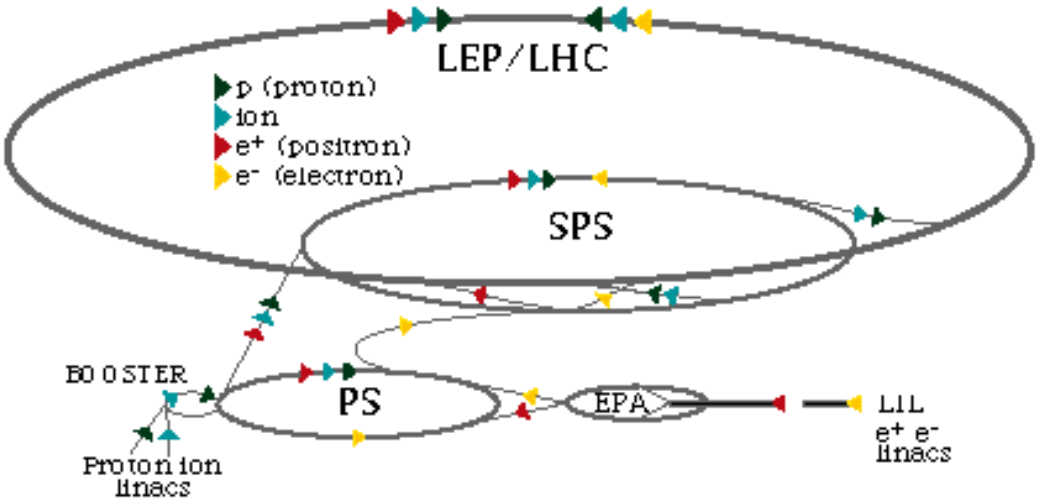


**Figure 1.1**: Topography of the CERN accelerator complex.

### The Super Proton Synchrotron

The SPS is a circular accelerator with a circumference of 6 km. It has been designed to accelerate protons, but like the PS changed functionality in time. It has been operated as proton/anti-proton collider, can accelerate heavy ions and works as electron-positron injector for LEP . As collider ($p - \overline{p}$) it provided in the 1980s the first detection of the weak force carriers (W and Z).

### The Large Hadron Collider

Both the PS and the SPS will be used in the pre-injection chain of the *Large Hadron Collider* (LHC). PS will provide protons with an energy of 26 GeV/c to the SPS which will be the last LHC pre-injector accelerating them to 450 GeV/c before the extraction to the main collider. In this contest many modifications and developments will be necessary (hardware changes on the RF system, upgrade of the beam instrumentation, etc...).
LHC is a large scale project which plans the installation in the LEP tunnel of a completely new machine which will be able to accelerate and collide proton-proton beams at an energy of around 7 TeV per beam and push the high energy particles research to reach new goals.
All the project has been developed to allow LEP working until the year 2000. LHC injection tests will take place in 2003, and in 2005 injection into the LHC is planned.

## 1.3 LEP

The *Large Electron Positron collider* (LEP) is the largest $e^+ - e^-$ storage ring existing in the world. In 1976 a study group was formed at CERN to investigate the feasibility of such a complex machine. In August 1979 a first design was presented for a ring having a circumference of about 30 km. Some modifications on the design were later discussed, mainly due to the need of staying as far as possible from the feet of the Jura mountains which are surrounding the Geneva area, avoiding in such a way the tunneling of a hard kind of rocks.
In 1981 a final design was completed for a machine of about 27 km circumference. The energy per beam of the LEP Phase I should have reached 60 GeV, with the possibility of increasing it up to 100 GeVadding super-conducting RF cavities[1] to the copper ones.
The project was approved and between 1983 and 1988 LEP was the largest civil-engineering undertaking in Europe, of which the 26.67 km Main Ring tunnel represented the most impressive part of the work. Great effort was put in the precision necessary for the trajectory of the tunneling machines, which was achieved through the use of geodesic networks. For example the 1 cm precision (later measured with the particle beams) on the 26.67 km of the circumference is worthy of note.
The tunnel lays on a plane between 50 and 150 m underground and has an inclination of 1.42 % compared to the horizontal plane, in order to be supported by a stable stratum of material. The beam trajectory is designed to have eight straight sections of about 500 m each and eight arcs of about 2800 m, with a radius of 3096 m.

Four detectors were installed in the straight sections to measure the elementary particles out coming from the $e^+ - e^-$ colliding beams (see Section 1.3.1).
The first injection into the LEP collider took place on $14^{th}$ July 1989 and one month later the first collisions between electron and positrons were provided. On the $20^{th}$ of September the first physics run started.

### 1.3.1 Particle Physics Program at LEP

LEP has been built to verify experimentally the theory which is trying to describe the ultimate structure of matter, the fundamental particles and their interactions (Standard Model). The choice of having $e^+ - e^-$ colliding particles beams was based on the fact that the beams can be accelerated to an energy measurable in a reasonably easy way with a good accuracy and that the state of the particles before the collisions is well known.
During the first phase of LEP the beam energies were such that the center of mass energy of the interaction was in correspondence of the Z boson resonance peak (see Fig. 1.2), neutral carrier of the weak force. Being under a resonance peak means having a high probability of events production. The dominant reaction is:

$$e^+ + e^- \rightarrow Z \rightarrow f\overline{f}\,,$$

where $f\overline{f}$ indicate a fermion-antifermion pair.
The accuracy of the boson mass determination is a combination of a statistical error of the

[1] Radio Frequency accelerating cavities.

hadronic cross section (i.e. resonance peak and width) and the uncertainty of beam energy. The particle production rate at LEP was high enough to allow the first error to be comparable to the energy measurement uncertainty after one year of machine operation.

Since the autumn of 1995, the energy has been increased to almost double its earlier value. In the summer of 1996, LEP ran at the exact value needed to produce pairs of the charged carriers of the weak force, the W+ and W- particles.

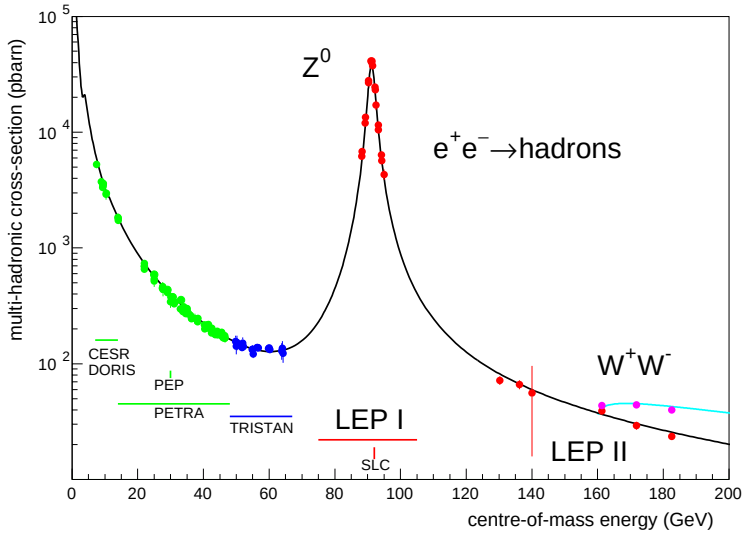


**Figure 1.2**: Hadronic cross section as function of beam energy, for different lepton colliders.

**The Particle Physics Experiments**

Four facilities are present at LEP hosting the experimentals areas where the aim is to record the events from the $e^+ - e^-$ collisions: ALEPH, DELPHI, L3 and OPAL.

They are situated in the 4 equidistant interaction points located along the accelerator ring. Each of them has been optimised to study different physics aspects.

The beams are strongly focused before they reach the collision regions in order to maximize the event rate (see Sec. 1.3.1) of the process. Electrons and positrons collide head-on and disappear with the consequent burst of energy. Immediately after such energy is transformed back into matter, through the production of new particles.

A complex detector has the function of determining the boson energy and momentum, catching and recording the events outcoming from the collision. The general structure of a LEP detector is presented in Fig. 1.3. A powerful solenoidal magnet is bending the tracks of the produced particles in order to measure their curvature and thus their momentum. Several tracking detectors surrounds the collision point in order to optimize the position measurement accuracy.

The energy of the particles is determined by their penetration depth in matter. The electromagnetic and the hadron calorimeters are used for such energy measurements.

The only charged particles which can penetrate this matter are muons, which are detected by the external muon chambers. Knowing a particle energy and momentum allows the calculation of the particle mass and thus the identification of the particle.

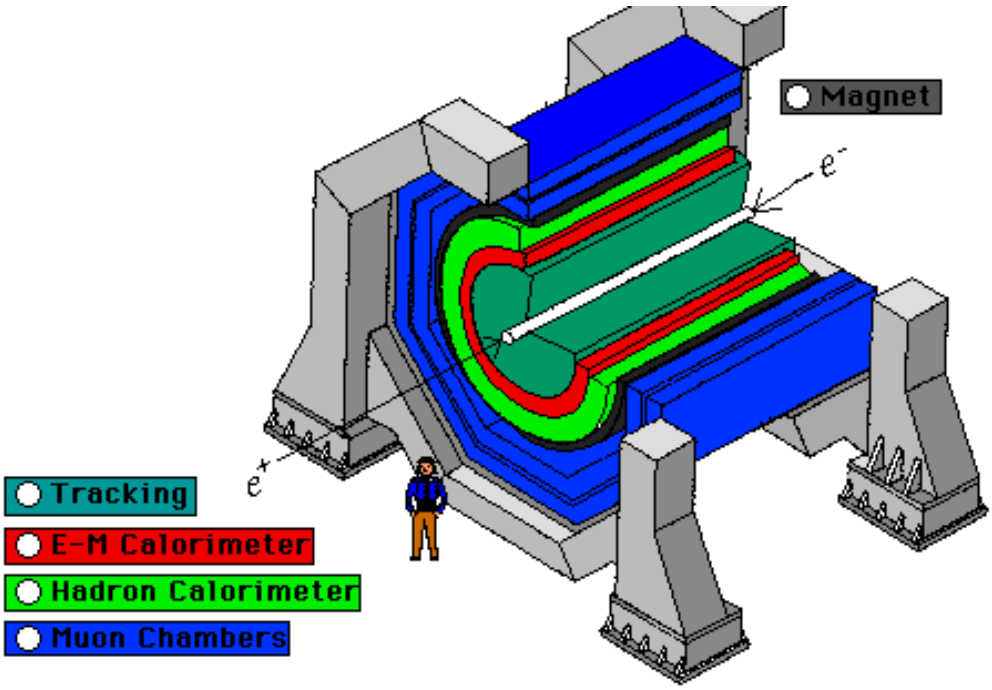


**Figure 1.3**: General structure of a LEP detector.

**Luminosity**

A fundamental parameter for a collider design, commission and operation is the particle production rate dN/dt, relative to the colliding beams at the interaction points. It is given by

$$\frac{dN}{dt} = \sigma \mathcal{L}, \tag{1.1}$$

where $\sigma$ is the cross section of the process and $\mathcal{L}$ is the *luminosity*, which is a function of the beams parameters

$$\mathcal{L} = \frac{N_{e^+} N_{e^-} k_b f_{rev}}{4\pi \sigma_x^* \sigma_y^*} \tag{1.2}$$

in which $N_{e^+}$ and $N_{e^-}$ are the number of positrons electrons per bunch, $k_b$ the number of bunches, $f_{rev}$ is the particles revolution frequency and $\sigma_x^* \sigma_y^*$ is the cross section of one bunch at the collision point. The integrated luminosity achieved at LEP during the different years is showed in Fig. 1.4.

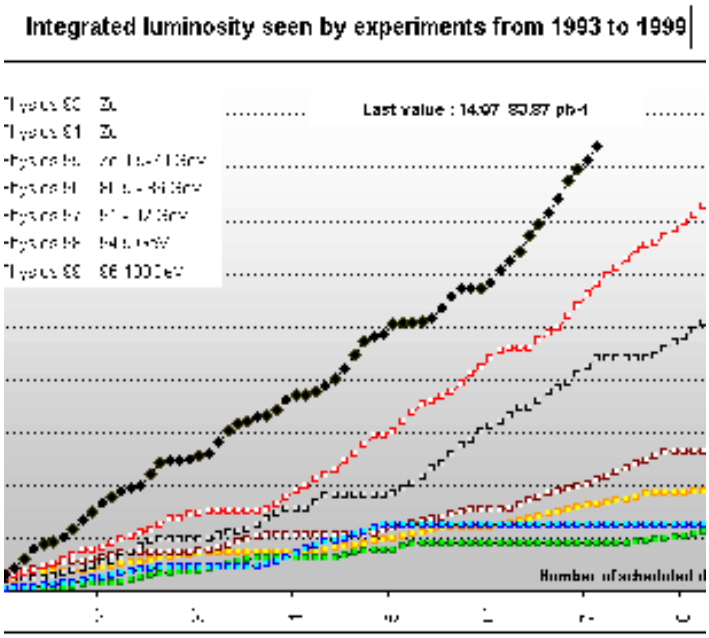


**Figure 1.4**: Integrated luminosity at LEP .

# Chapter 2

# Energy Calibration

Several interesting informations, as the mass of the $Z$ for example, can be inferred studying the relations between the cross section of selected events and the energy of the colliding $e^+ - e^-$ beams. At LEP the extremely high rate of profitable events allows the measurement of those relations to a very precise level. The maximum effort in the knowledge of the energy of the particles in the colliding beams is therefore required. The target relative accuracy is of the order of $10^{-5}$ for energies around 45 GeV and $10^{-4}$ for higher energies. These accuracies are defined by the maximal achievable accuracy at 45 GeV, resulting in the same uncertainty for the beam energy error and the physics experiments statistical error. At beam energies between 90 and 105 GeV the limit is fixed, such that the uncertainty in the beam energy is only marginally influencing the measured parameters and the main error component is due to statistics and calibration errors in the four giants detectors used in the analysis of the collisions.

## 2.1 Energy Calibration Basics

The relation between the particle momentum and its energy is (general relativistic case):

$$E^2 = (pc)^2 + (m_o c^2)^2 \tag{2.1}$$

where $E$ is the energy, $p$ the momentum and $m$ the mass of the particle. For ultra relativistic particles the rest energy is much smaller than the kinetic energy, hence:

$$\frac{dE}{E} = \frac{dp}{p} \tag{2.2}$$

In a storage ring the particles have to go back after each turn to the same average location, their path is a *closed orbit*.
The *close orbit* is a solution of the equation of motion for particles travelling in a storage ring, under periodic constrains. During one turn around the ring each particle must cover an angle of $360^o$,

$$\oint \frac{1}{\rho(s)} ds = 2\pi, \tag{2.3}$$

where *s* is the curvilinear coordinate along the path, $\rho(s)$ is the local *curvature radius* and the integral is performed along the close orbit. The equilibrium of the Lorentz force and the centripetal force leads to the relation between the particle momentum, the local transversal B-field and the

local curvature radius: $|\vec{p}(s)| = q|\vec{B}(s)|\rho(s)$ being *q* the particle charge. This means that Eq. (2.3) becomes:

$$\oint \frac{qB(s)}{p(s)} ds = 2\pi. \tag{2.4}$$

The transverse magnetic fields are the dipole, the quadrupole and higher order fields. In LEP they are produced by separate function magnets placed along the ring (see section 2.1.2).
During normal operation, the particles motion around the ring has to be kept synchronous to the radio frequency (RF) phase of the accelerating cavities. For this reason the length of the close orbit (L) is always a multiple of the RF wavelength:

$$L = \beta h \lambda_{RF} \approx h \lambda_{RF} \tag{2.5}$$

being $\beta = \frac{v}{c}$ ,v=particle velocity, c=velocity of light, h=harmonic number, $h = 31320$ for LEP .
The length of the closed orbit is not changing as long as the RF frequency is constant, like actually happens during stable operation of the machine.
Eq. (2.4) and Eq. (2.5) define the equilibrium momentum in a storage ring [1]. The particle momentum during normal operation is thus determined by the transverse magnetic field B(s) and the RF frequency $f_{RF}$.

A further step can be done assuming a relative circumference[1] variation of the storage ring when the magnetic field is ideally constant. From Eq. (2.4) we can thus derive [2]:

$$p = q\rho_0 B_0 \left(\frac{C}{C_0}\right)^{1/\alpha_C} \tag{2.6}$$

$$\alpha_C \equiv \left.\frac{\Delta C/C}{\Delta p/p}\right|_{B=B_0}. \tag{2.7}$$

The quantity $\alpha_C$ is called *momentum compaction factor*. The differentiation of Eq. (2.6) leads to:

$$\frac{dp}{p} = \frac{1}{\alpha_C}\frac{dC}{C} + \frac{dB_0}{B_0}. \tag{2.8}$$

To summarize:

– during the normal operation of the collider the length of the closed orbit is not changing, since $\lambda_r f$ is constant (Eq. (2.5));

– the particle momentum can then change only due to a variation in the ring circumference or in the bending field (Eq. (2.8));

– at LEP the momentum compaction factor is $1.8 \cdot 10^{-4}$ , therefore even a small change in the circumference causes a large particle momentum variation;

[1]The ring circumference (C) is slightly different from the close orbit length (L).

When considering the lepton beams, the energy value depends on the *total* transverse field along the ring, again assuming the length of the closed orbit constant. The determination of the total bending magnetic field is very difficult. Not only because for the 3000 dipole cores each 6 m long (see section 2.1.2), the integral B-field has to be determined with high accuracy. But also for the fact that the field in these cores is slightly changing over the years and large stray fields are present all over the ring, making the task of mapping the magnetic field along the beam path impossible, at least with a relative accuracy of $10^{-5}$.
Furthermore, when the beam is not travelling along the ideal trajectory, the quadrupole magnets give a contribution to the bending field. Due to ground motion, the magnets change their radial position and the particles go off-centered through the quadrupoles. The radial quadrupole displacement causes an additional deflection of the particles. Since the length of the orbit $L$ is a constant, the particle has to alter its energy in order to fit the distorted machine. Dipole magnets do not add to this effect, because the dipole field does not depend on the radial position.

A method called *resonant depolarisation* (see section 2.2.1) is used for the measurement of the beam energy with an accuracy of $1{\cdot}10^{-5}$ in the range of 40-60 GeV. This method uses some properties of the beams themselves for estimating the integral of the magnetic field around the ring.
The resonant depolarisation has two drawbacks:

i. it can only be applied during dedicated experiments and can thus not be used to monitor the time evolution of the energy during physics fills;

ii. it does not work at the energies actually exploited of the order of 100 GeV.

The first problem can be compensated by monitoring all the parameters that can possibly influence the beam energy during the fills and developing models to estimate their effects. One of the most important monitored parameters is the bending field. The monitoring is achieved by means of $\approx 20$ nuclear magnetic resonance magnetometers (NMR) uniformly distributed in the LEP magnets (see section 2.2.2). The sampling precision is of the order of $10^{-6}$ [3]. The accuracy of the model is few $10^{-5}$ and typical variations of the order of $10^{-4}$.
The model is regularly calibrated using the depolarisation method. At operational energies of 100 GeV the model is extrapolated using the calibration with the resonant depolarisation method in the range between 40 and 60 GeV.
The basic question is whether the model takes all parameters into account and whether that model valid in the small range where cross calibration with the resonant depolarisation is possible is still valid for large variations of the parameters.

To have an independent determination of the beam energy a spectrometer (chapter 3) has been thought, designed and installed. The spectrometer is intended to measure the difference in energy between the energy points where the resonant depolarisation method is applicable and the operational energy of 100 GeV.
In the next sections the mechanism of beam energy increase (*acceleration*) will be described and later the many elements which determine the beam energy operational level (the *magnets*) will be discussed.

### 2.1.1 Particles Acceleration

The LEP storage ring is the last accelerator in a chain of five (see Fig. 1.1). The LIL (*Linear Injector for LEP* ) accelerates thermoelectric produced electrons up to an energy of 200 MeV . These electrons hit a target of heavy material producing photons which have enough energy to cause pair production of positrons and electrons. Beyond the target the LIL accelerates the particles up to 600 MeV. They are then stored in the EPA (*Electron Positron Accumulation* ring) which collects the particles of the rapid cycling LIL (100 Hz) in bunches. Eight bunches of positrons and electrons are accelerated in the PS and SPS and stocked into the four positron and four electron bunches of LEP, every 14 s. The particles injected into the PS are accelerated up to 3.5 GeV and then reach 22 GeV in the SPS. Eventually the eight LEP bunches are stored and the beams are accelerated to the operational energy (i.e. 100 GeV).

Each charged particle with a non-zero acceleration looses energy emitting photons along its trajectory. In a storage ring this is always true, also at operational energies, when the magnitude of the particle velocity can be almost constant, but its direction is continuously changing (transversal acceleration). The increase of the particles kinetic energy (during acceleration) and the compensation of the energy losses are supplied by longitudinal oscillating electric fields.
The energy loss $\Delta E$ of a beam with energy E, on a circular path with a radius $\rho$ is

$$\Delta E \propto \frac{E^4}{\rho} \tag{2.9}$$

At LEP between the two energies 22 GeV (end of injection) and 100 GeV (physics) the energy loss is increasing of a factor 426. Each turn a particle is loosing 3.4 % of its energy. This energy (carried by the photons) is deposited on the materials surrounding the beam pipe, where the photons are stopped. At LEP, at the operational energy of 100 GeV the amount of energy deposited is of the order of 700 W per meter.
The oscillating electric field which is used to accelerate the particles is produced in dedicated structures of *cavities*. Inside each cavity the voltage is oscillating with a frequency of 352 MHz and in every cavity of the structure the particle is experiencing the same potential difference. About 7 MV per meter are applied in order to perform the acceleration.
The increase of the bean energy is done by increasing the bending magnetic field. This will cause the particles to circulate on a shorter trajectory, with a smaller radius. Consequently these particles reach the cavities structure a bit earlier. In this case the particles see a larger accelerating voltage and gain kinetic energy. The change in the particle velocity is very small, since they can be considered already relativistic at a beam energy of 22 GeV. This process is continuing until when the increase of the magnetic field is finished.
When the beams circulate at a certain nominal energy, the potential difference which is seen by the particles is regulated in such a way to compensate the energy loss due to photon radiation. If during a turn a particle gains a bit more energy than needed, it will go on a slightly larger trajectory, arriving in the cavities a bit later. The potential difference experienced by the particle is thus smaller and the energy increase also reduced. This self-adjusting mechanism keeps the particles energy oscillations to about 100 MeV around the nominal beam energy value.

### 2.1.2 The Magnet System

The particle beams in LEP are guided by electromagnetic fields produced in several kind of magnets:

- dipoles,
- quadrupoles,
- sextupoles,
- horizontal and vertical dipole correctors,
- rotated quadrupoles,
- electrostatic dipole deflectors.

About 75 % of the ring is occupied by magnetic elements which are structured in "cells". Each of the eight arcs of the circumference (*octants*) contains 31 of these cells which consist of the following elements:

- horizontal focusing half cell (HC): one half of a horizontal focusing quadrupole, one horizontal dipole corrector, a group of six bending dipoles (the cores are excited in groups of two by the same coil, two dipoles form one *bending magnet*), one vertical sextuple, one half of a vertical focusing quadrupole;
- vertical focusing half cell (HC): one half of a vertical focusing quadrupole, one vertical dipole corrector, a group of six bending dipoles, one horizontal sextuple, one half of a horizontal focusing quadrupole.

In LEP one full standard cell is 79.11 m long.
The statement "half a quadrupole" is just a way to indicate that one quadrupole in the layout of the beam line belongs for one half to a vertical focusing half cell and for the other half to a horizontal one.
With this nomenclature it is possible to describe the beam transfer line as a periodic lattice where each cell has a focusing structure called FODO (Fig. 2.1) which consist in a horizontal (or vertical) focusing quadrupole (F), a region of drift space (or with a bending magnet) (O), a horizontal (or vertical) defocusing quadrupole (D), and another drift space (or bending magnet) (O).
The figure shows a horizontal focusing half cell, the previous and the following will be vertical focusing.
The electron and positrons are kept in the (ideally) circular trajectory by the dipole magnets. The large bending radius, chosen to reduce the amount of synchrotron radiation emitted by the beams, allows the use of a low bending field (about 0.1 T at 100 GeV). The dipoles were designed to have a 4 mm gap between the steel laminations (1.5 mm thick) filled by mortar, instead of full iron cores. With this solution the costs of the dipole sets was reduced of about 40 %. A transversal cross section of a dipole with the beam pipe inserted in the gap is shown in Fig. 2.2.
The quadrupole magnets (Fig. 2.3) act as magnetic lenses, producing a magnetic field proportional to the transversal position of the beam. The sextupoles compensate the dependence of the quadrupole strength on the beam energy (chromaticity), producing a field quadratically changing with the particles offset from the ideal orbit.
The vertical and horizontal dipole correctors are individually powered magnets able to steer the

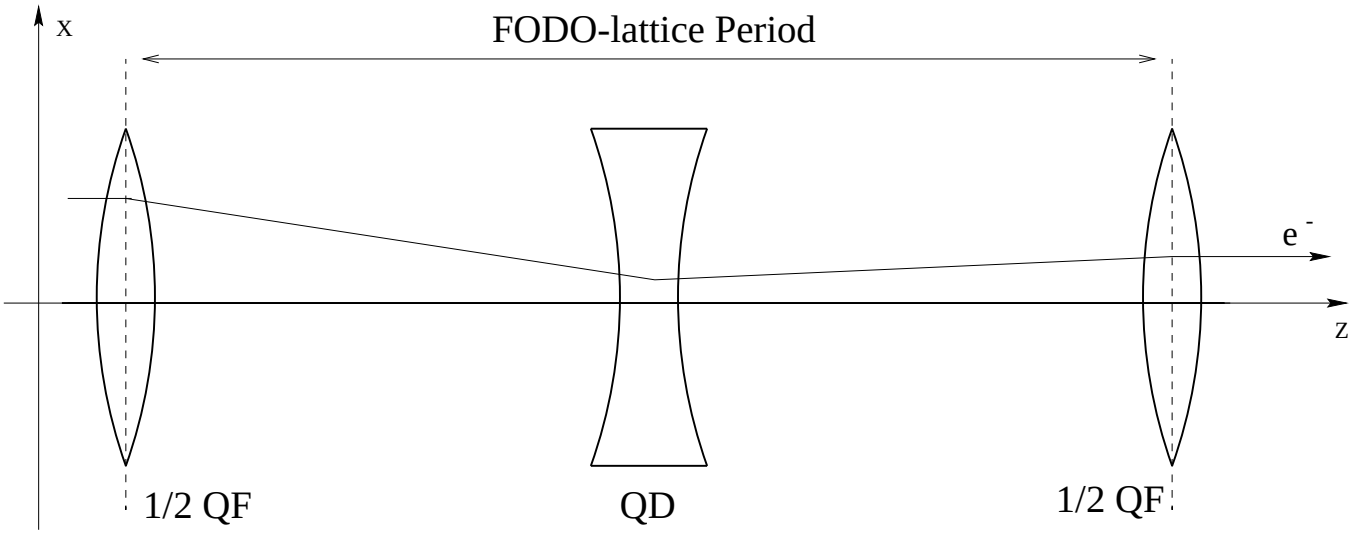


**Figure 2.1**: FODO lattice for a beam line half cell (QF:focusing quadrupole, QD: defocusing quadrupole).

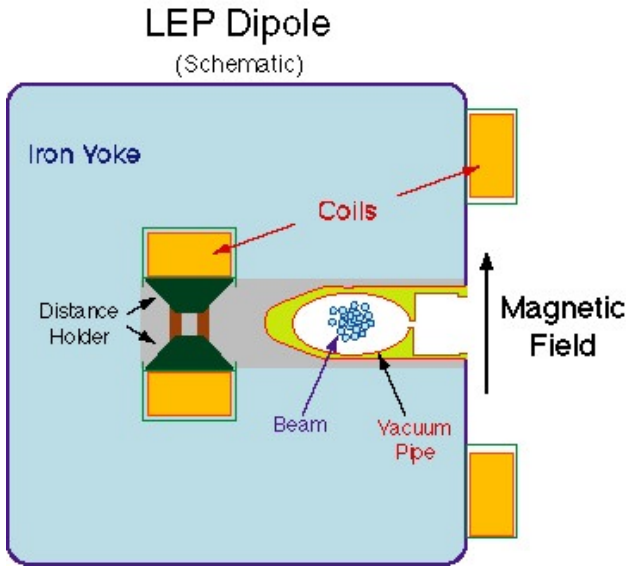


**Figure 2.2**: Cross section of a LEP bending dipole.

beam through the center of the beam pipe.
The beam bunches must reach the center of the experiments detectors (see Section 1.3.1) with very small dimensions, in order to increase the particle production rate (luminosity) when the beams approach each other head on. Hence some super-conducting quadrupoles were inserted in the proximity of the interaction points. They have a strong field gradient and guarantee a reduction of the beam dimensions to about $4\ \mu$m and $250\ \mu$m in the vertical and horizontal planes.
The strong solenoidal magnets which surround the experiments cause a coupling of the horizontal beam oscillations in the vertical plane, which is compensated by the insertion on the beam line of some standard quadrupoles with the axis rotated of $45^o$.
The beams could in principle cross each other in all the eight straight sections of the ring, but that

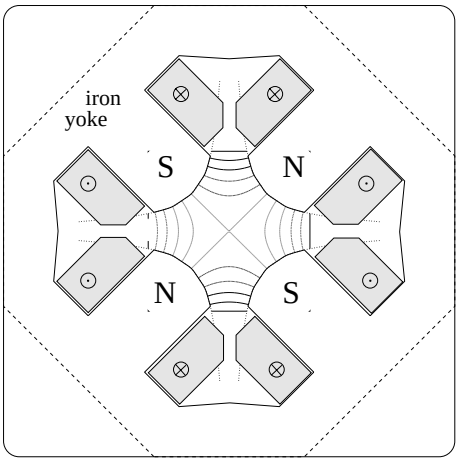


**Figure 2.3**: Cross section of a LEP focusing quadrupole with its field lines.

is not desirable in the four ones where there are not detectors installed. Hence some electrostatic dipole deflectors are inserted, in order to keep the beams separated. Such separators are also installed around the four experiments with the aim of avoiding collisions during the filling of LEP and to better align the beams before the run into the physics period (see Section 1.3.1).

## 2.2 Energy Calibration Tools

In this section an introduction to the beam energy calibration methods will be given.

### 2.2.1 Resonant Depolarisation

One of the degrees of freedom of the leptons circulating in the collider is the *spin*. For a charged particle with angular momentum $\vec{L}$, the spin is described as vector $\vec{S}$ aligned with $\vec{L}$ and having magnitude dependent on the particle type (electrons, protons and muons have spin 1/2).
The behaviour of polarised beams in a storage ring is governed by the interaction between the spin of the single particles and the external electromagnetic field. For each particle a magnetic momentum $\vec{\mu}$ is expressed as:

$$\vec{\mu} = \frac{ge}{2m_0}\vec{S} \tag{2.10}$$

where *g* is the gyromagnetic ratio[2]. Charged particles with a magnetic momentum $\vec{\mu}$ in a magnetic field $\vec{B}$ experience a torque $\vec{N} = m\vec{u} \times \vec{B}$ which causes a precession of the spin $\vec{S}$ around $\vec{B}$ (Fig. 2.4). The spin precession frequency is proportional to the magnetic field experienced by the particle.
When turning around LEP the particles emit photons due to the synchrotron light. This photon emission tends to align the spins parallel to the external magnetic field. This mechanism, known as Sokolov-Ternof effect, is based on the different probabilities for a particle to flip its spin during the emission of the photon depending on the orientation of the spin itself compared to the magnetic field. Such *transverse polarisation* builds up naturally and can be described with an ideal asymptotic level $P_\infty$, to which the polarisation levels exponentially tends with a time constant $\tau_p$.

[2]g=2(1+a), being *a* the gyromagnetic anomaly, typical of the particle. a=1.159652$\cdot 10^{-3}$ for electrons.

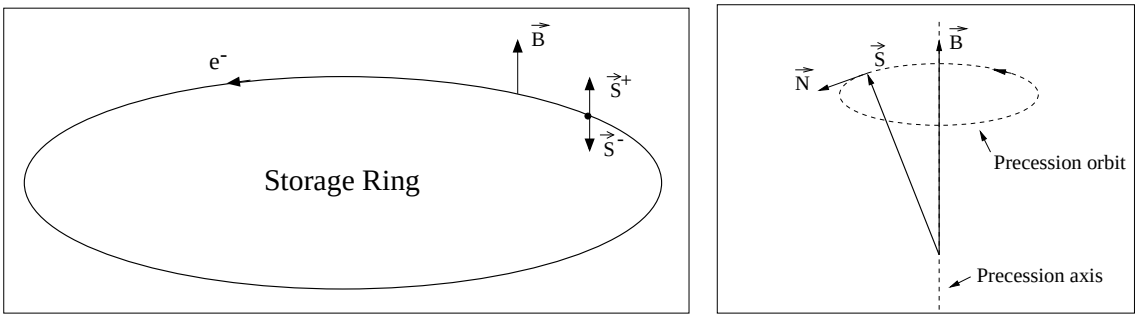


**Figure 2.4**: Particles of a polarised beam in a storage ring orientate their spin aligned to the main bending field.

$P_\infty$ is $92.4\,\%$, which means that even after an "infinite" time and ignoring any depolarising effect, there is a probability larger than zero to have particles with spins of opposite orientation. The transverse polarisation build-up rate is increasing with the beam energy, being $\tau_p \propto E^{-5}$.

Unfortunately many other effects (for example the interaction between the particles spin and non-vertical magnetic fields presents along the path) tend to destroy the alignment of the spins with the B-field vector, in a way which increases with the energy in a way faster than the polarisation build up.[3].
The combination of the two leads to a function for the alignment which reaches a maximum at a beam energy of around 44 GeV and then starts to decrease again.
The equilibrium can be expressed as:

$$P(E,t) = \frac{P_\infty \left(1 - e^{-\frac{t}{\tau}}\right)}{1 + \frac{\tau_p}{\tau_d}} \qquad (2.11)$$

$$\text{being } \frac{1}{\tau} = \frac{1}{\tau_p} + \frac{1}{\tau_d}$$

The polarization is defined as the mean spin vector:

$$\vec{P} = \frac{1}{N} \sum_i^N \vec{S}_i. \qquad (2.12)$$

where the sum is taken over all the *i* particles of the bunch.
Since the spin precession frequency is proportional to the magnetic field experienced by the particle, the precession integral or spin-tune $\nu$ (the number of precessions over one revolution period) is proportional to the integral of the magnetic field over the beam path. If we could measure the spin-tune we could deduce the field integral and thus the mean beam energy.

By placing an RF coil at an arbitrary position in the ring and selecting the right excitation frequency it is possible to force the particles to flip their spin (change the spin vector direction).

[3]The characteristic time constant of these depolarising effects $\tau_d$ is decreasing faster than $\tau_p$.

If the RF coil frequency is synchronous with the mean spin revolution frequency, all the spins of a bunch are changing their direction until the beam is depolarised ($|\vec{P}| = 0$) or even turned in the opposite direction ($|\vec{P}| = -1$).
The Resonant Depolarisation method consist of scanning small frequencies ranges with the excitation signal until the polarisation is destroyed (or flipped).

The measure of the beam polarisation is accomplished by the polarimeter. This device is based on a powerful laser with polarised light. The photons from the laser collide with beam particles and the scattered $\gamma$ (the back scattered photon are high energetic) are detected with a silicon strip detector. The average scattering angle is influenced by the polarisation of the photons and the polarisation of the particles. By alternatively changing the polarisation of the laser light[4] and measuring the distance between the mean angular distribution for the two laser light polarizations with a strip detector, the value of the beam polarization can be calculated.

In reality the procedure is rather complicated, as firstly one has to adjust the parameters of the machine in order to optimise the polarisation level. This is mostly a try and error procedure with many parameters to play upon and every trim takes several minutes to produce the effects. When the polarisation level is sufficient ($> 5\,\%$) the energy calibration starts. Several depolarisations are required in order to obtain an unambiguous spin-tune (it is possible depolarise at frequencies different from the spin-tune and one has to investigate if the one found is the right one or not). Many hours are thus required to do a full measurement (what is called an energy point). For cross calibration of other methods or models several energy points may be required in one LEP fill (one beam accelerated to diferent energies) and calibration experiments lasting more than 24 hours are not uncommon.

During LEP I operation the calibration via the resonant depolarisation method were initially performed at the end of normal physics fills and sometimes at the beginning. Starting from 1995 dedicated periods were used, since the increase of the operational energy required to perform the energy calibration at different points. The magnitude of the excitation of the focusing magnets (optics) is also a critical parameter, too strong focusing on the vertical plane causes strong spin kicks in the vertical plane leading to a depolarisation of the beam. Hence a different optics setup is normally adopted during the calibration time. Furthermore non-colliding beams (or even better one beam operation) reduce the probability of depolarising effects. Details of the energy calibration at LEP with the resonant depolarisation method are described for example in [4] and [5].

### 2.2.2 Magnetic Field Monitoring

The dipole magnetic field around LEP has been initially (1989) only monitored in a reference magnet. This special magnet was electrically connected in series with the other dipoles in the LEP tunnel, but positioned at ground level in a thermal controlled room. It is a full iron core dipole magnet in which a flip coil and some NMR probes have the aim of monitoring directly the magnetic field and its changes. The magnet current is measured with several instruments (DCCTs)

[4] From right to left circular polarization and vice-versa.

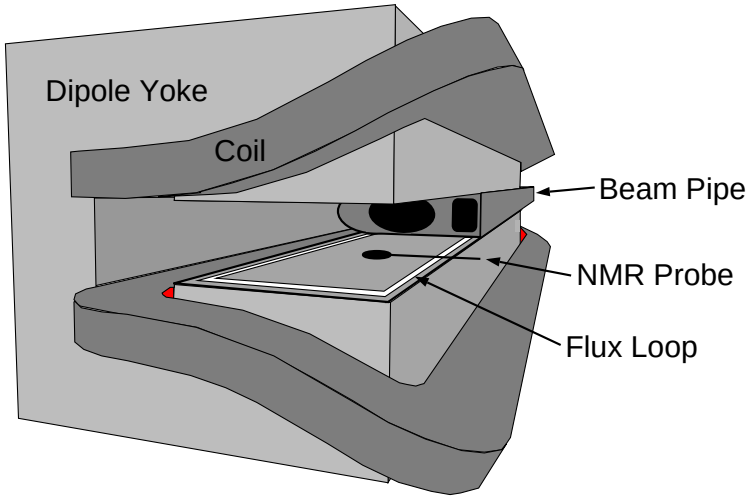


**Figure 2.5**: Section of an iron-concrete LEP bending dipole, with the NMR probe and flux-loop coil positioning.

with a relative accuracy of $1.5 \cdot 10^{-5}$ .
The measurement was also performed inside a short section of vacuum chamber, inserted in the dipole gap in order to reproduce carefully the conditions experienced by the beam.
In 1995 two NMR probes (see Chapter 4) were installed between the vacuum chamber and the pole tip of two LEP dipoles (Fig. 2.5). In 1996 14 additional NMR probes were installed, allowing the sampling of the magnetic field in each octant of the ring.

### 2.2.3 Flux-Loop

A loop covering the horizontal plane cross section of the bending field dipoles is installed in the LEP dipoles. Cycling the magnets an induced voltage can be detected across the coil, leading to a measurement of the dipole integral field. This operation has been performed almost every two weeks during 1993 and 1994, but its frequency was reduced in 1995 when the confidence in other magnetic measurements was increased (see Section 2.2.2) and the repeated cycling[5] of the magnets could affect the dipole characteristics and the accelerator operation.
The flux-loop measurements remained anyway one of the tools for the energy calibration at LEP II. In Fig. 2.5 the positioning of the flux-loop cables is indicated.

[5]The normal flux-loop procedure includes also a change in the voltage polarity.

## 2.3 Energy Calibration Model (ECM) at LEP I

The energy calibration through the resonant depolarisation method (see Section 2.2.1) allowed a very precise estimate of the beam energy at the $Z$ resonance peak (around 45 GeV per beam). However it has to be performed with non colliding beams (or with a single beam), while the information needed has to be related to the accelerator *physics* conditions. The average beam energy (as measured by RD) is determined by the integral around the ring of the vertical component of the magnetic field seen by the beam. As earlier explained, there are several contributions to this field integral: the main one is the field produced by the LEP dipoles which is sensitive to temperature and parasitic currents (see section 2.3.1); the second is the bending field from off-centered quadrupoles which is affected by variations in the LEP circumference, in particular changes due to terrestrial tides; and finally, the additional fields generated by the quadrupole-current imbalance compensation loop and horizontal-orbit correctors must be taken into account. New understanding has been accumulated over the years about the behaviour of the dipoles, of the geology of the Geneva area and the LEP civil engineering structures. A model was thus created drawn up to correct the direct energy measurements both for effects depending on the machine operation and time variations of the energy due to environmental regular or random events. Such model is included in [6] and can be summarized by the following formula:

$$\begin{aligned} E_{\mathrm{beam}}(t) &= E_{\mathrm{norm}}(fill) \\ &\cdot(1 + C_{\mathrm{rise}}(t_{\mathrm{day}}, t_{\mathrm{fill}})) \\ &\cdot(1 + C_{\mathrm{T-dipole}}(t)) \\ &\cdot(1 + C_{\mathrm{tide}}(t)) \cdot (1 + C_{\mathrm{orbit}}(fill)) \\ &\cdot(1 + C_{\mathrm{h.corr.}}(t)) \cdot (1 + C_{\mathrm{QFQD}}(t)) \end{aligned} \tag{2.13}$$

The model takes care of the different possible changes of the $E_{\mathrm{norm}}$ which is the nominal beam energy computed as the mean value of the calibrated energies with resonant depolarisation at the same energy point. The meaning of the terms of equation 2.13 is described below.

– $E_{\mathrm{norm}}$ is different depending on whether or not the fill in question was calibrated using the RD method. If it was, then this normalization factor ensures that the energy of the model at the moment of the calibration equals the value of the calibration for this fill. If it was not, this term is equal to the mean normalization factor of all the calibrated fills at that energy point.

– $C_{\mathrm{rise}}(t_{\mathrm{day}}, t_{\mathrm{fill}})$ is the term accounting for the rise of the bending field due to the parasitic currents flowing along the beam-pipe. It is parametrized as a function of the time-of-day, $t_{\mathrm{day}}$, and time since the magnet reached the final field, $t_{\mathrm{fill}}$

– $C_{\mathrm{T-dipole}}$ is the temperature correction for the ensemble of ring dipole magnets [7].

– $C_{\mathrm{tide}}$ is the correction due to the effect of the Earth tides [8].

– $C_{\mathrm{orbit}}$ is the correction for the deviation of the horizontal position of the orbit from a *central orbit* with no quadrupole bending component. This effect is calculated using an average orbit position for each fill after the expected variations for tide have been removed.

– $C_{\mathrm{h.corr.}}$ is the correction due to the setting of the horizontal correctors (see section 2.1.2).

– $C_{\mathrm{QFQD}}$ is the correction for current in the QFQD compensation loop[6].

It was thus possible to estimate the center-of-mass energy at each interaction point as

$$E_{\mathrm{CM}}^{\mathrm{IP}}(t) = 2 \cdot E_{\mathrm{beam}}(t) + \Delta E_{\mathrm{RF}}(t) + \Delta E_{\mathrm{disp}}(t) + \Delta E_{\mathrm{e^+}} \tag{2.14}$$

where further corrections for local changes of the RF frequency, dispersion effects and possible differences between the electron and positron beams are taken into account. All this allowed to provide the LEP experiments with a mean value of the beam energy for each fill with the correspondent error.

### 2.3.1 Environmental Influences

By investigating the behaviour of the magnetic field read by the NMR probes installed in the LEP tunnel, it was discovered that a current up to few amperes was circulating on the walls of the beam pipe and on all parallel conductors in the LEP tunnel, like the ground cables connected to earth at all the eight interaction points [1, 9].
The French railroad line between Geneva and Lyon is powered with a 1500 V DC voltage (Fig. 2.6). A clear correlation exists between the voltage changes on the railroad supply lines, the parasitic currents detected along the LEP vacuum chamber and the field changes measured by the NMR probes installed in the tunnel dipole magnets. The current input and output locations in the LEP ring are at IP6[7] and IP1. A fraction of the current (3/5) is reaching IP1 passing IP7 and IP8 and the remaining fraction (2/5) is passing through IP5, IP4, IP3, and IP2.
The phenomenon is related to a well-known problem related to DC railroad tracks [10]. The current supplied by the power stations to the trains should come back to the generators via the railroad tracks. A significant part of it, up to 25 %, can however flow back through alternative paths in the earth. In this sense the conductors in the LEP tunnel represent a “preferential path”. The currents flowing along the beam pipe can then modify the magnetic field in the dipoles.

During the work for this thesis some measurements were performed on the full-iron core dipoles in the injection region of the LEP ring (see Section 3.4.1) and the influence of the train induced current had to be taken into account.
In Fig. 2.7 an example of such phenomenon is shown. The current indicated in the middle plot is detected measuring the voltage drop along the beam pipe. Two possible effects of the train current influence are present:

i. a field drift after which the magnet is not coming back to its original working point; that means there is a shift on the magnet hysteresis cycle (see Fig. 2.7 at t = 5h.58m);

ii. a field jump after which the magnet is returning to the previous field value (see Fig. 2.7 at t = 4h.24m).

[6]The optics in LEP is sometimes set to have a different phase advance in the vertical and horizontal planes. This means that the current in the focusing and defocusing quadrupoles is slightly different. A compensating loop (the QFQD loop) was installed to balance the effect of additional bending due to such asymmetry, but remaining effects have to be considered.

[7]IP = Interaction Point, numbered anti-clockwise from 1 to 8, Fig. 2.6.

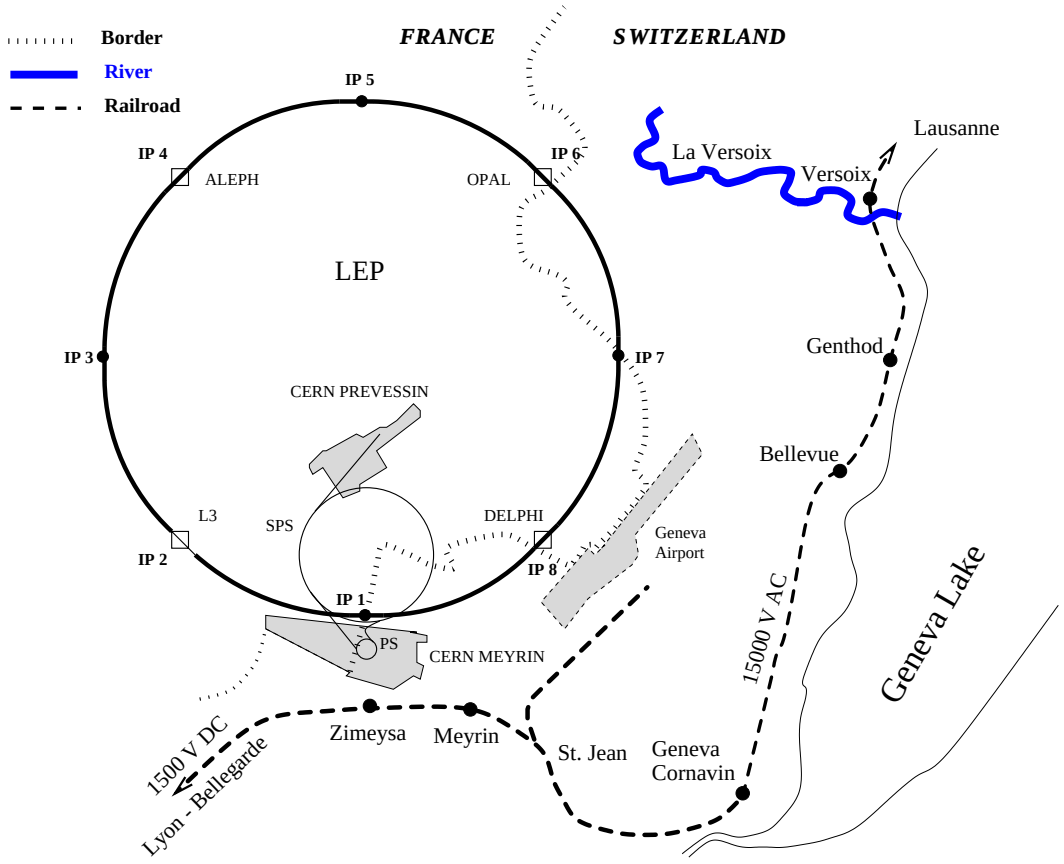


**Figure 2.6**: Map of the Geneva area, with the two main railroads (Geneva-Lyon and Geneva-Lausanne) indicated.

This is an example of why the energy calibration model has to take care of the daytime and of the different locations in the ring: the train current influence is in fact depending on both.
Concerning the LEP spectrometer which will represent the main topic of this thesis, the choice of the ring section where to insert it (LEP IP 3) was also done observing the less influence of the trains travelling with respect to other sections (see Fig. 2.6).

In the energy model (Eq. (2.13)) a correction for the iron-concrete dipole cores thermal behaviour is included. The major heat sources are resistive-loss heating of the excitation bars and the synchrotron radiation emitted by the beams along the vacuum chamber.
A temperature variation produces a distortion in the dipoles geometry. Depending on the temperature gradient the gap of the C-shaped cores tends to open or close, changing the field lines distribution. The thermal expansion of the materials increases the pole area. Thermal induced stresses change the pressure between the iron laminations and the concrete which is between them, causing a relative change in the iron permeability and introducing thermal hysteresis effects on the magnetic field.
In a laboratory facility at CERN several tests have been carried out on a LEP spare dipole, allowing the development of a *thermal model* which includes a parameterization of the effects described above [7].

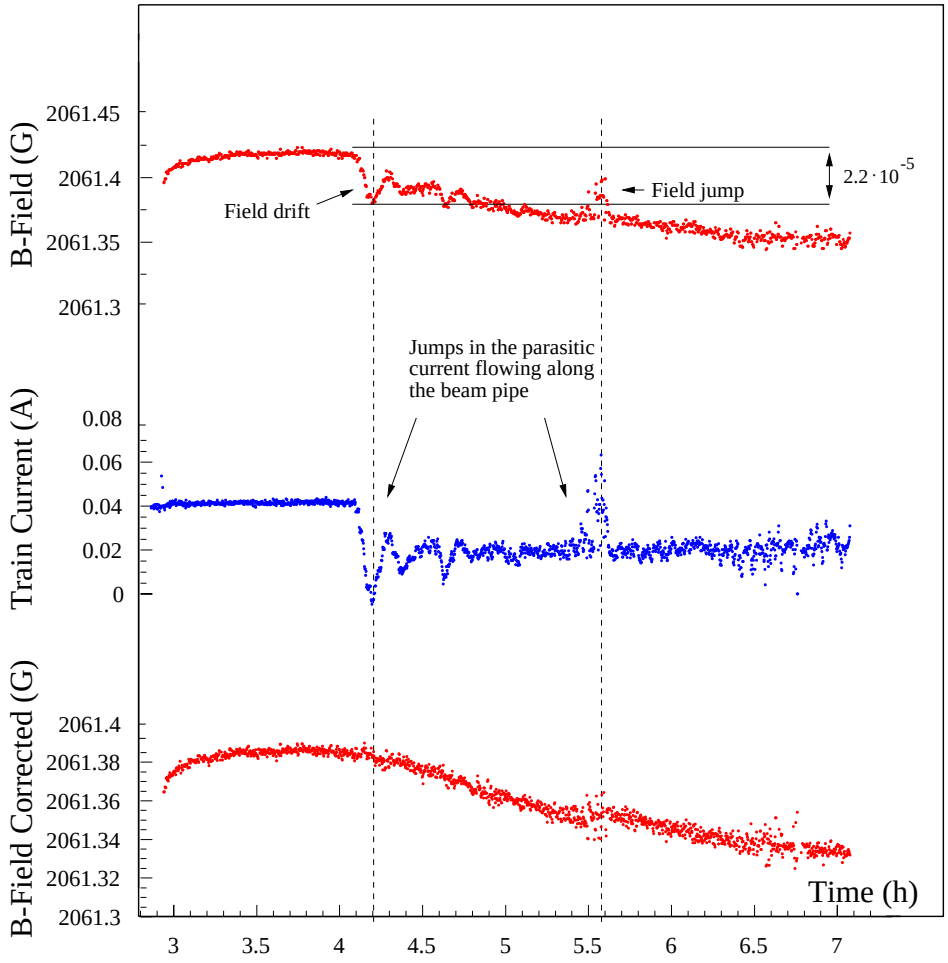


**Figure 2.7**: The current due to the railway DC voltage (middle) affects the dipoles magnetic field (top). The excellent correlation allows the field correction (bottom) in order to plot the pure dipole field.

## 2.4 Energy Calibration at LEP II

Resonant depolarisation (see Section 2.2.1) is available at LEP only up to beam energies of 60 GeV [11] until the 1998 run, at higher energies depolarising effects are such increasing to avoid the build up of a sufficient transversal spin polarisation of the beam.

During the LEP II operation, commissioned in 1996, the beam energy is pushed above the W-pair production threshold, which corresponds to about 80 GeV per beam. The beam energy measurement is carried out by the monitoring of the bending field along the ring. Sixteen NMR probes are placed on a number of bending dipoles distributed in all the octants, in order to give a sampling of the total bending field.

The probes are read continuously during both the physics periods and the periodical times dedicated to the machine for the calibration of the beam energy. During these periods the particles are accelerated at energies between 41 GeV and 55-60 GeV where the energy is estimated with

high accuracy via the resonant depolarisation procedure. In this way a precise reference calibration between the NMR probes and the beam energy is given for each energy point measured by the resonant depolarisation. For each probe two parameters $a^i$ and $b^i$ are calculated in order to satisfy the relation:

$$E^i_{pol} = a^i + b^i \cdot B^i_{nmr} \qquad \begin{cases} i & = 1 \ldots 16, \\ E_{pol} & = 41 \ldots 60\, GeV. \end{cases} \tag{2.15}$$

The two parameters are changing between different probes, but they are reproducible along the different calibrations carried out during the year. The residuals to the energy measurement with the resonant depolarisation of the energy prediction with the 16 NMR probes are plotted in Fig. 2.8 for different calibration fills. The test of the linearity between NMR probes and beam

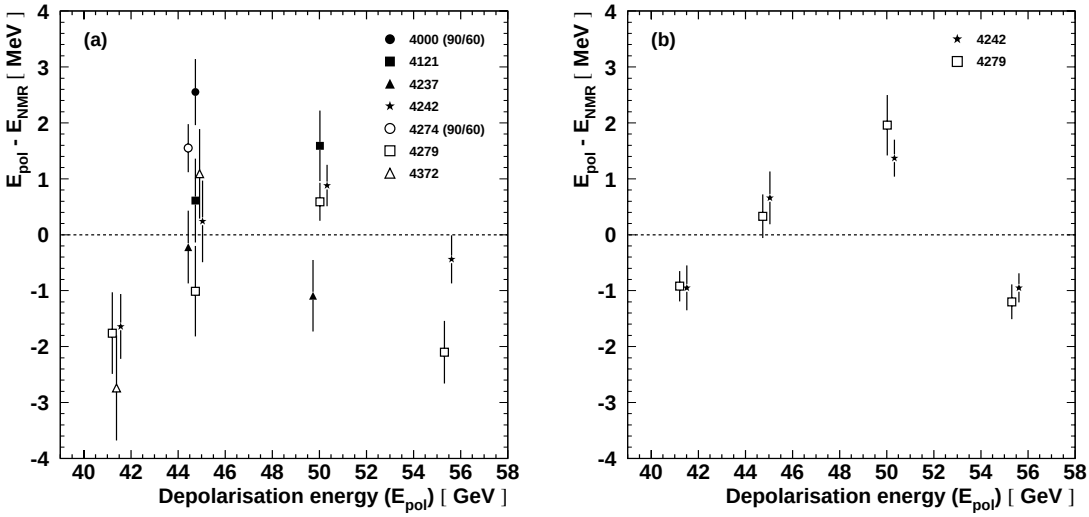


**Figure 2.8**: Residuals of the fit comparing RD energies to the energies predicted by the model (a) for a simultaneous fit to all fills and (b) for individual fits to each four point fill. For clarity, the points for different fills have been plotted at slightly displaced depolarisation energies (plots taken from [12]).

energy is also checked monitoring the field in the sixteen fixed locations during some periods in which *flux loop* measurements are performed (see Section 2.2.3). The local field is monitored during the steps of the magnet cycling typical of this measurements, giving a test of the linearity between the NMR readings and the total bending field. A second independent calibration of the NMR probes is thus given, according to:

$$E^i_{flux-loop} = c^i + d^i \cdot B^i_{nmr} \quad i = 1 \ldots 16. \tag{2.16}$$

In Fig. 2.9 the expected correlation between the slopes and the offsets estimated with the two methods is shown.

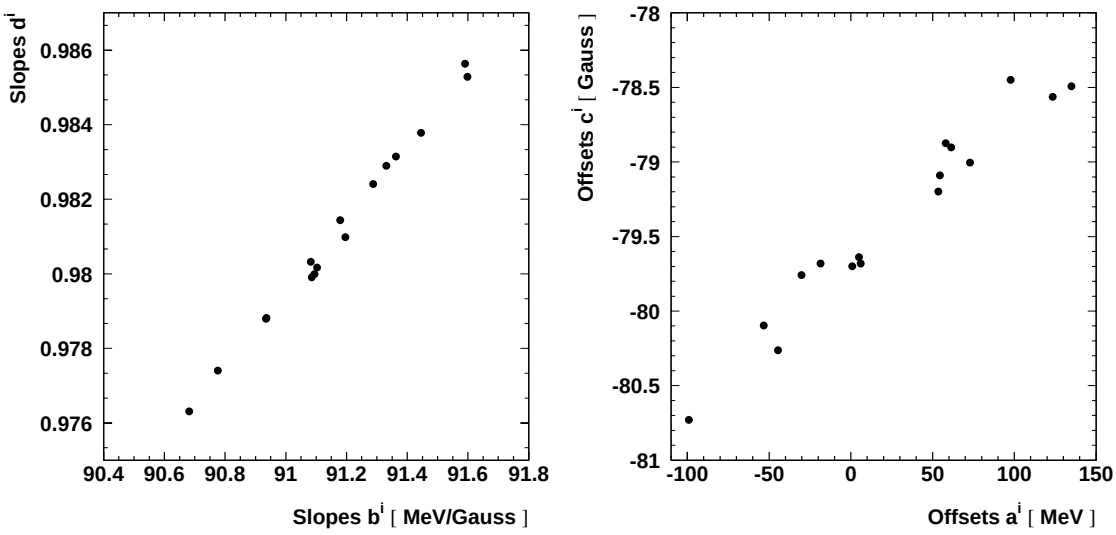


**Figure 2.9**: Correlation between the 16 NMRs slopes and offsets of Eq. (2.15) and Eq. (2.16). There is one entry for each NMR probe, averaged on several flux-loop measurements and resonant depolarisation calibrations [12].

**Table** 2.1: Summary of contributions to the 1997 beam energy uncertainty at 82 GeV, taken from [12].

| Source | Error [MeV] |
|---|---|
| Extrapolation from NMR–polarisation: | |
| NMR rms/$\sqrt{N}$ at physics energy | 10 |
| Different $E_{\rm pol}$ fills | 5 |
| Flux-loop test of extrapolation: | |
| NMR flux-loop difference at physics energy | 20 |
| Field not measured by flux loop | 5 |
| Polarisation systematic | 1 |
| $\mathrm{e^+e^-}$ energy difference | 2 |
| Optics difference | 4 |
| Corrector effects | 3 |
| Tide | 1 |
| Initial dipole energy | 2 |
| Dipole rise modeling | 1 |
| IP specific corrections ($\delta E_{\rm CM}/2$): | |
| RF model | 4 |
| Dispersion | 2 |
| Total | 25 |

The measurements with the flux-loop cycles are not used to correct the coefficients of Eq. (2.15), but just taken as a linearity test. The relation between the field measured by each NMR probe and the beam energy is then considered to be linear and the beam energy in physics conditions is therefore extrapolated like:

$$E^i_{nmr} = a^i + b^i \cdot B^i_{nmr}\,, \quad i = 1 \ldots 16. \tag{2.17}$$

The monitoring of the bending magnetic field during the beams collision is not enough to give an accurate evaluation of the beams energy. Time variations of the energy has to be taken into account. For this purpose an energy calibration model like the one for the LEP I operation (Eq. (2.13)) is used. A detailed description of the LEP II energy calibration procedure, analysis and results until 1998 is included in [12]. In table 2.1 a summary of the systematic uncertainties related to the energy calibrations for the 1997 LEP run is shown. The table is subdivided in five parts. The first includes error contributions estimated by comparing the resonant depolarisation (RD), called polarisation in the table, with the NMR measurement system. The second contains error estimated from the flux-loop measurements ant the NMR measurements. The following terms include small errors which result from the RD method itself. The fourth part contains model errors and the last term refer to errors which result from the transfer from *mean beam energy* to *local beam energy* at each LEP interaction point.
The total error on the energy is estimated from the comparison between the flux-loop measuring system and the NMR based system.

**Conclusions**

The ultimate estimate of the error on the statistical evaluation of the W mass is around 25 MeV. The uncertainty on the beam energy determination for 1997 is also 25 MeV as stated in [12]. An improved calibration of the beam energy is thus desirable in order to reduce its relative weight in the total error on the W mass determination. More accurate models are currently developed to extrapolate the beam energy from the magnetic field monitoring during the 1998 and 1999 LEP runs.
The commissioning of the LEP spectrometer represent an alternative method to evaluate the beam energy with different kind of systematic errors and the following parts of this thesis will mainly focus on that.

# Chapter 3

# The LEP Spectrometer

Before the 1999 LEP run a new device has been installed in the storage ring in order to measure the average particles momentum at the highest energy value used for physics studies (i.e. where resonant depolarisation is not available)

## 3.1 Spectrometer Concept

The LEP spectrometer has been conceived to be an alternative method for the beam energy determination, providing a *direct* energy measurement. The concept consists in detecting the change in the bending angle $\theta$ through the beam position monitors (BPM) and evaluating the total integral B-field seen by the particles while travelling inside the spectrometer magnet (see Fig. 3.1). The beam energy is then calculated, being

$$\Delta\theta \propto \frac{\int_L Bdl}{E_{beam}} \tag{3.1}$$

A top view of the spectrometer layout in the LEP tunnel is given in Fig. 3.2.

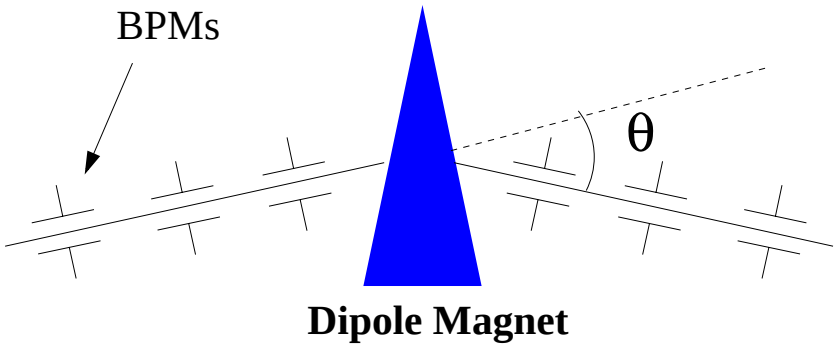


**Figure 3.1**: LEP Spectrometer schematic layout

Among the 16 possible places in the LEP ring with enough drift space to host a spectrometer, the one in the proximity of IP3, between the quadrupoles Q17 and Q18 has been chosen. The two standard iron-concrete bending magnets have been replaced by a single full-iron dipole (see Section 3.2) providing the same bending angle[1] of 3.8 mrad.

[1]This dipole has thus roughly two times the strength of one iron-concrete core

The required accuracy on the extrapolation of the beam operational energy is $1 \cdot 10^{-4}$ (relative error), i.e. 10 MeV for a beam energy of 100 GeV. In order to fulfill such requirements, the integral magnetic field of the dipole magnet has to be determined with a relative accuracy of $3 \cdot 10^{-5}$, while the orbits on both sides of the magnet has to be measured with an accuracy of $5 \div 7 \cdot 10^{-5}$. With the BPM placed on both sides of the magnet along arms of 7 m each, the required accuracy on the beam position is of the order of $1 \cdot 10^{-6}$ m.

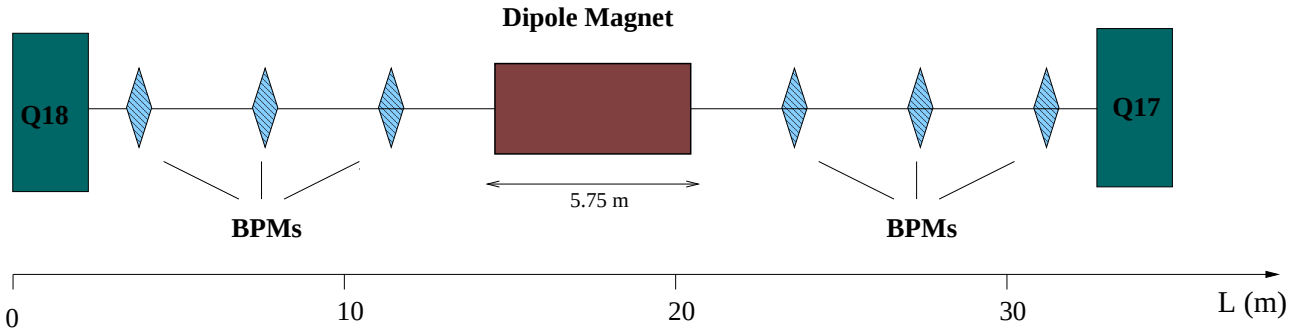


**Figure 3.2**: Top view of the LEP Spectrometer layout.

### Wire Position Sensors

The accuracy on the determination of the beam bending angle due to the spectrometer magnet is strongly depending on the relative stability of the BPMs positions. Each station, mounted on a limestone block, can shift its position or expand, mainly due to thermal gradients, thus compromising the calibration of the monitors. In order to correct for these possible displacements, a system of *wire position sensors (WPS)* has been added in the spectrometer setup.
The wire system consist of three wires; the first extends over the whole spectrometer and is intended to to observe movements of the arms of the spectrometer with respect to each other. The other two wires are installed one on each arm, for redundancy and to distinguish between shift and expansions of the BPMs.
Eighteen WPS are then mounted at different locations in order to monitor the movement of the BPMs with respect to the wire and of the wire with respect to the supporting limestone blocks.
The wire is passing in between two electrodes of the sensor and principle of measurement consist in determining the capacitance between the electrodes and the wire. This is achieved by measuring the current from the electrodes while an alternating voltage of 10 V peak to peak is applied at 4 kHz. The capacitance is, to the first order, inverse proportional to the distance in this geometry.
The system was tested and calibrated by changing the temperature of the BPM stations[2] while observing the movements read by the WPS [13]. This test revealed a temperature coefficient consistent with the expansion material of the BPMs materials (aluminium). Another kind of test based on a laser interferometer setup[3], provided a credible calibration by comparing the wire position monitoring of the capacitive sensors and of the laser interferometer.
The use of the WPS system during the LEP operation allowed interesting discovers about a correlation between the sensor outcome and the beam current intensity. Such effect was attributed to

[2]Operation possible thanks to the dedicated temperature regulation system.
[3]The same instrumentation used for the travelling mole position monitoring, described in Section 5.1.2.

the synchrotron radiation interaction with the position monitoring apparatus. The most trustable theory explains how the photons ionize the air molecules in between the sensor electrodes, giving rise to a charge collection and a spurious signal, not related to a real wire movement.
Special lead shieldings were thus put around the capacitive sensors and a sensible reduction of the effect was observed.
The WPS represent an important tool for the global accuracy of the LEP spectrometer operation.
In Fig. 3.3 a sketch of one BPM station together with the wire system position monitors are shown.

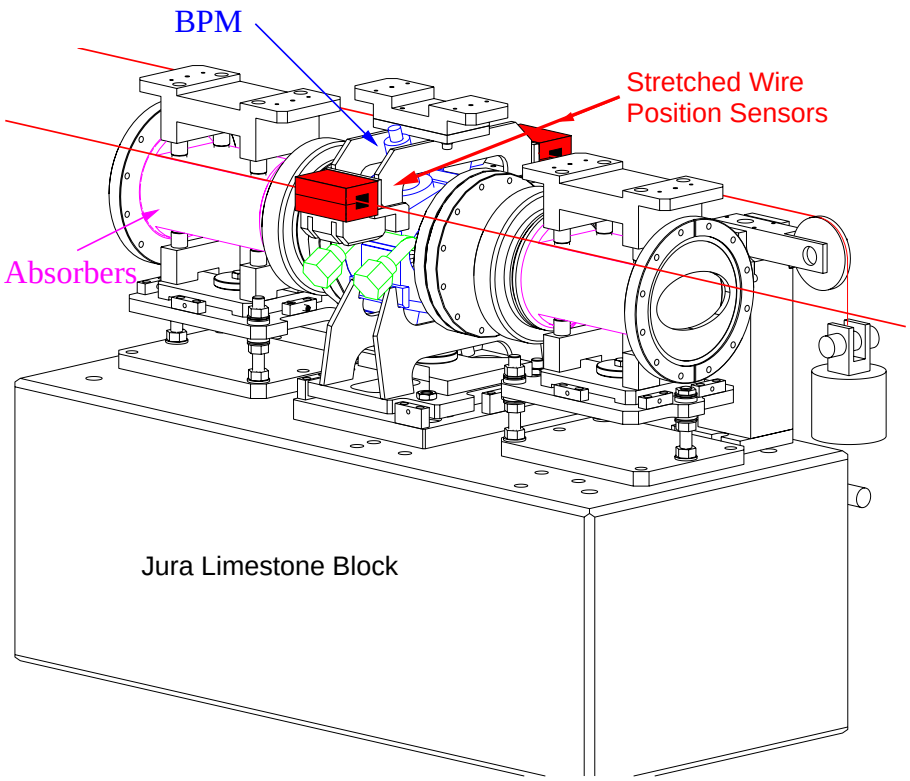


**Figure 3.3**: One of the six BPM stations with the attached wire system.

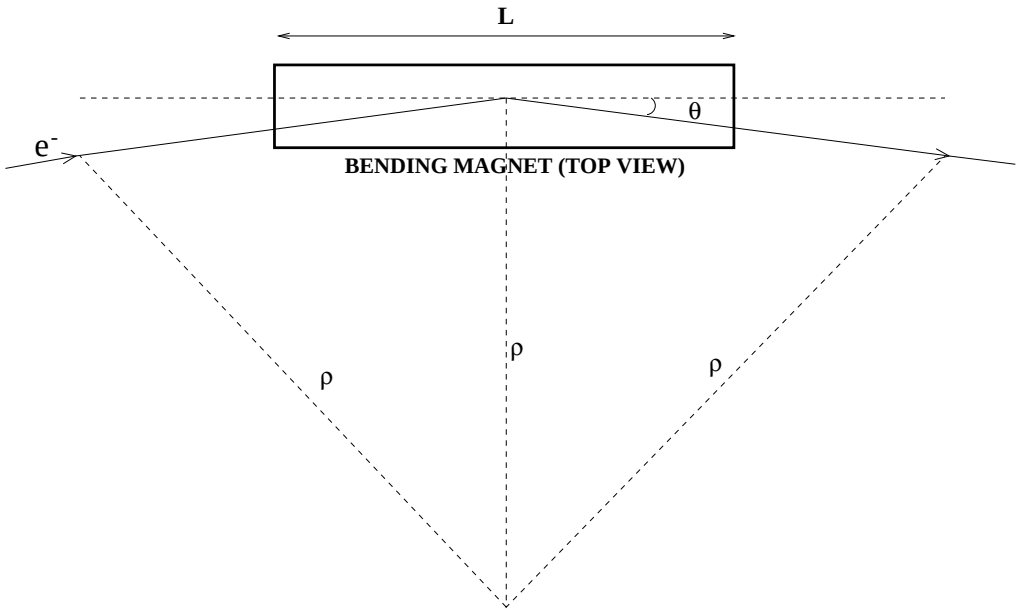


**Figure 3.4**: Particles horizontal bending under the influence of a dipole magnetic field.

## 3.2 The Dipole Magnet

A fundamental element of the Spectrometer is the dipole magnet which is used to bend the particles. The main purpose of the spectrometer is the determine the energy increase from a low level to the operational energy (see Section 3.1 Therefore the magnitude of the beam energy increase has to be determined. There are two extreme cases how a spectrometer can be designed: the magnet can be kept at a constant field and the beam movement is measured; alternatively the beam can be kept at a constant position and the magnetic field is ramped in a well-known way. In the first case the magnetic properties must be known only at one current level. The bending angle changes at different beam energies and consequently the beam position. In this case there would be large beam position displacements also in the regular LEP structure, event that would be unacceptable. Furthermore this would imply a high accuracy over a large dynamic range of the beam orbit monitors.
The choice of the magnet was mainly depending on the following criteria:

1. the possibility of determining the B-field with the highest possible accuracy;
2. having low perturbations in the LEP machine global parameters and characteristics;
3. available time for the commissioning, building and installation.

Fixing the bending angle of the magnet to 3.75 mrad the best choice was limited between two standard 6 meters long LEP iron-concrete cores and one full-iron injection magnet. The latter did not exist and had to be built, while a number of spare concrete-iron cores were available. In Table 3.1 the advantages and disadvantages of the two possibilities are listed. The iron-concrete magnet design causes high and complicated dependence of the magnetic field on temperature changes. This feature would perturb the integral field prediction by mean of the local NMR probes. The place occupied by the magnet is also important, because the length of an half cell in LEP is

| Full-iron core | | Iron-concrete core | |
|---|---|---|---|
| PROS | CONS | PROS | CONS |
| | Non existent | Existent | |
| Only iron | | | Iron-concrete (aging) |
| Small temperature coefficient $C_T$ | | | Large and complicated $C_T$ |
| Short (longer BOMs lever arm) | | | Long |
| Higher synchrotron radiation from the magnet | | Lower synchrotron radiation from the magnet | |
| Only one iron yoke | | | Need of two cores (difficult mapping of the fringe field on the contact region) |
| | New cables | No need to change cables | |
| | Dedicated Power converter | Powered in series with the other magnets | |
| Possibility to require a high field quality for the new core | | | |
| | Special cooling system | Even more important to adopt a special cooling system due to the complicated $C_T$ | |

**Table** 3.1: Pros & Cons in choosing an iron-concrete or a full-iron core for the spectrometer magnet.

fixed (see Section 2.1.2). The longer the magnet, the shorter the lever arm of the Beam Position Monitors. Hence the requested accuracy could be compromised. The best choice in terms of high field accuracy and enough space for the orbit monitors is given by the iron magnet design adopted in the LEP injection region (MBI) and for the spectrometer the decision taken was to commission a new magnet, with a special request for a smooth profile of the magnetic field longitudinally, transversally and vertically.
The magnet is 5.75 m long which is 5.50 m shorter than a LEP iron-concrete bending magnet.[4] As mentioned above one of the problems is the larger power irradiated by the charged particles with a smaller bending radius. The radiated power as function of the beam energy E, the length of the

[4]There is sometimes confusion in the definitions: in LEP one *bending magnet* is composed of 2 *cores* excited by the same coil.

magnet L and the bending angle $\Theta$, reads:

$$P \propto \frac{E^4 \Theta^2}{L^2} \tag{3.2}$$

If the angle $\Theta$ is kept constant and the length L is decreased of a factor two, the radiated synchrotron power is increased of a factor 4 for a given beam energy.
Such photon energy power is hitting the same location and spreads over the same area of the vacuum chamber since the bending radius is the same. The location where the photons interact with the beam pipe are outside the spectrometer influence. The higher power dissipation outside the spectrometer is not critical because it is demonstrated that, in the other ring locations where the magnets of the same type (MBI) are used, the cooling system is sufficient.
The critical energy is also increased by a factor two, passing from 0.724 MeV to 1.45 MeV, but the absorption coefficient does not change (being the same for most of the absorbers at energies around 1 GeV)[5].
The English firm Tesla was chosen as supplier of the magnet.

### 3.2.1 Magnet Description

The MBI magnet is a C-shaped iron laminated magnet 5.75 m long. The yoke is built from 1.5 mm thick laminations made of low carbon steel [15], two end plates (30 mm thick) keep the laminations stacked together. Some 20 mm thick steel rods are placed along the longitudinal dimension of the magnet, connecting the end plates. These rods provide a stabilization against twist. Two racetrack shape coils surround the higher and lower pole of the magnet, they are composed of 3 layers, with 6 windings each. The layers are connected electrically in series and hydraulically in parallel. This scheme ensures the same current in every winding and a low temperature across the coil cross section.
The coil heads contain the layer to layer transition and the 6 tails for hydraulic and electrical connections.
Tests on the existing injection magnets show that the rigidity of such magnet was not sufficient. The twist along the longitudinal axis was up to two degrees, when wrongly supporting the magnet. In order to avoid changes of the magnetic field shape, caused by internal stress, displacement of the laminations or changes in the magnet dimensions, a special support ("girder") was constructed. The girder was mounted before the beginning of any of the field mappings, including in such a way in the measurements some possible effects on the field strength and distribution. A description of the simulations of the girder influence is presented in Section 3.2.2.
The magnet was placed in the ISR IP8 (where a test bench was previously prepared) in October 1998. At first the vacuum chamber was not installed in the gap in order to allow the mapping with a first method based on a movable arm inside the yoke, described in Section 3.2.3.
Only two vacuum chamber parts ($\approx$ 50 cm long) were mounted with special supports on both sides outside the magnet. They were shielded with a $\mu$-metal material, wrapped around the pipe at a precise location. This guarantees that the magnetic field is negligible at 50 cm from both the longitudinal ends of the yoke. This is important to set a "zero field" location which is not dependent on the environmental conditions. To provide the same conditions between the laboratory and the LEP tunnel (i.e. operational conditions), it was foreseen to put the same $\mu$ -metal wrapped first around the dummy vacuum chamber installed for the mole measurements and eventually on the final vacuum pipe.

[5] A quantitative comparison of the two cases at 100 GeV was presented by M.Placidi [14].

### 3.2.2 Field Calculations

In order to predict the magnetic field shape and properties, some simulations were carried out [15]. Both a two-dimensional and a three-dimensional model were developed. The first is enough to study the field locally at different transversal and vertical positions. The 3-D model was necessary to investigate the effect of the end field region shims[6] and the $\mu - metal$ influence.
From the simulation of the original MBI magnet (whose design is in [16]), it was that evident quite an important non homogeneity of the field in the transversal direction, even in the central region of the magnet, where no edges effect are present. Two asymmetric shims and a slope in the pole design surface would have meant a relative field change of the order of several $10^{-4}$, along the $\approx 130$ mm in the transversal pole length. Negligible would have been the relative change of the $\int Bdl$ for 1 mm displacement of the beam in the central part of the gap of $\approx 1 \cdot 10^{-5}$ .
The simulation showed that this was mainly due to the pole slope. It was consequently decided to design parallel pole faces. The 3D model allowed the evaluation of the total effect of a transversal shift of the beam on the $\int Bdl$ . End and central field changes are of opposite signs, so partially cancel each other. A residual gradient consisting of a relative change of 0.4 ppm/mm on the $\int Bdl$ was predicted.
Some calculations were done to investigate the possible influence of the girder on the magnetic homogeneity (see Section 3.2.1), since the girder itself has a magnetic permeability similar to the one of the magnet laminations. The girder attract part of the stray field, modifying the return path of the field lines ([15],Chapter 4.4). The transversal homogeneity of the dipole field is not changing of a relevant amount, while the magnitude of the field is increasing of a factor $2 \cdot 10^{-5}$ at 100 GeV. The girder breaks the top-to-bottom symmetry, leading to an additional transversal component on the field, whose magnitude in the transversal and vertical center is $\approx 1 \cdot 10^{-5}$ T at 100 GeV.
This is the same if the magnet would be tilted of $4.5 \cdot 10^{-2}$ mrad, equivalent to 0.02 mm along the transversal dimension of the magnet. Such difference is considered negligible.
The presence of the $\mu$-metal shielding of the vacuum chamber was also studied. Choosing a distance of 50 cm between the end of the magnet and the beginning of the screen, considering three layers of 0.2 mm thick $\mu$-metal, the calculations give a factor 10 of attenuation.

### 3.2.3 Measurements in the Laboratory with a Carbon Movable Arm

A dedicated measurement setup has been developed in order to accurately map the magnet in the laboratory facility at ground level. The system is based on a carbon-fiber arm equipped with NMR probes and hall plates able to scan the magnetic field profile. An electronic ruler monitoring the arm position allows the evaluation of the integral field. Such system performed several field maps before the installation of the beam pipe and is not transportable. Therefore it could not guarantee any check of the B-field after the the magnet equipment with the beam pipe and its transportation in the LEP tunnel. The final chapter (Chapter 7 of this thesis will include an important part about the comparisons between the results of these measurements with the mole ones in the laboratory and in the LEP tunnel.

[6] Where the longitudinal field component due to the coil is not negligible

## 3.3 Reference NMR Probes

The positioning of the four reference NMR probes has been carefully studied by scanning locally the B-field, in the region between the dipole lower pole and the beam pipe. A device able to move an NMR probe in the three dimensions in a small region has been used and an example of the field behaviour is shown in Fig. 3.3.
The reference NMRs have been placed following such analysis, choosing four locations where the field has the smallest gradients in all directions (dB/B $< 10^{-5}$ per mm). In such a way the error due to possible small misplacements of the probes after their removal and/or substitution (during all the spectrometer operation) is negligible. After choosing the optimal locations, some special supports have been designed and mounted in order to guarantee a high precision of every probe's repositioning, since for the aim of the spectrometer project as a whole it is important to monitor the local field always at the same locations.

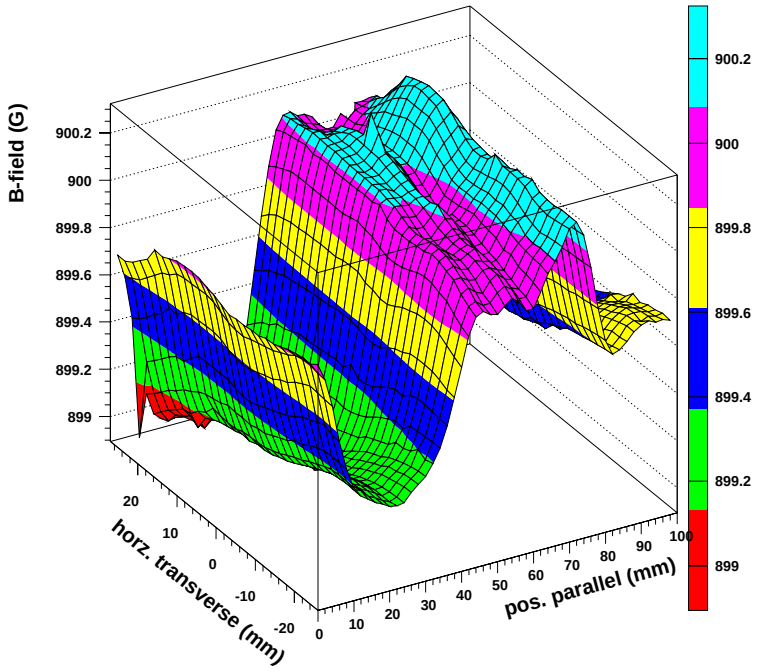


**Figure 3.5**: Example of the local field monitoring around the reference NMR probes: the B-field is scanned at different horizontal positions for 100 mm in the longitudinal direction.

Among the other components, a small variable ferromagnetic capacitor is inserted in the probes body, to allow the auto-tuning of the instrument around the resonance signal. Interference between two NMR probes has been observed when the head of one probe is less than 10 cm away from the body of the other probe. Such was the case during the LEP spectrometer magnet mapping, every time that the movable probes were passing by the fixed ones (see Fig. 3.3). During the data analysis average values of the reference probes were calculated, not taking into account the peaks due to the aforementioned disturbances.

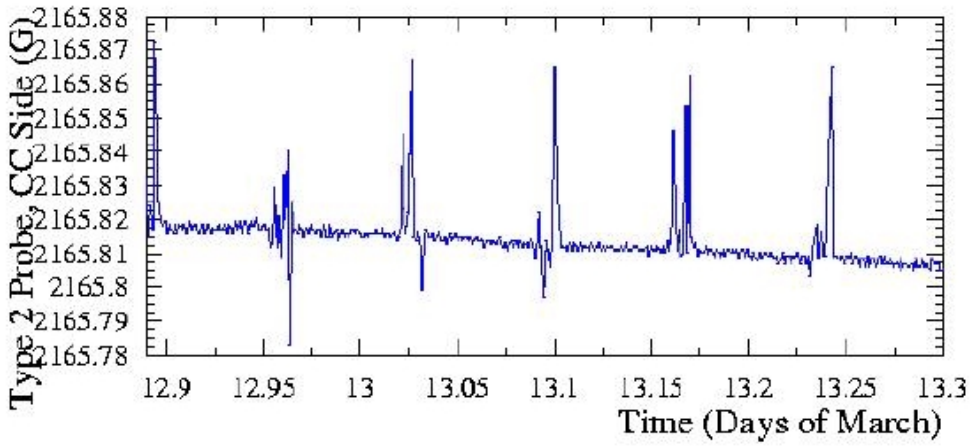


**Figure 3.6**: In the readings of the reference probes it is possible to distinguish the peaks (one for each map) due to the interference between the movable and fixed probe.

## 3.4 Temperature Behaviour

To predict the integral field of the spectrometer magnet during operation, four fixed NMR probes are used. The coefficient between integral field and reference probes was evaluated during the mapping campaign. In principle a change in the environmental conditions, such as temperature or humidity which can modify the magnetic field, are observed by the probes, leading to a change of the integral field at a given current supplied to the dipole.
In fact such effects are not uniformly distributed. A change in the conditions at a certain location of the magnet, is not necessary the correct indication of the average change on the magnet. In this contest keeping the temperature as constant as possible is important.
During a physics cycle in LEP the magnetic field in the dipoles is changing and is monitored by several NMR probes (see Section 2.2.2). Small oscillations or spikes are related to external factors like TGV currents (see Section 2.3.1) or noise on the power converters.
Instead, a constant slope in the field can be usually related to a temperature increase. The amount of heat dissipated is of course increasing with the energy. The rise is not linear with the working point, since two contributions take part in the heating:

- the Joule effect of the current flowing in the magnet;
- the synchrotron radiation photons emitted by the beam.

The first scales with the second power of the coil current (i.e. with the second power of the energy). The SR instead increases with the fourth power of the beam energy. This means that the two contributions have different weights at different energies. Furthermore they linearly depend on the beam current.
Accordingly the power is dissipated on the vacuum chamber (due to SR) and in the iron of the magnet (due to the current in the coil), with a relative importance which is not constant with the energy.
For this reason the LEP main components, magnets, radio frequency accelerating cavities and vacuum pipe are cooled each with a dedicated system consisting in de-mineralized water flow. The aim of the cooling system is to control the temperature excursion on the different components.

### 3.4.1 Field Variation with Temperature

The ratio between the spectrometer magnet integral field at different energies is depending on the thermal behaviour of the magnet. Let us take two beam energies $E_1$ and $E_2$; the corresponding magnetic field integrals will depend on several parameters, in particular they will be function of the temperature of the coil, the temperature of the yoke, the heat flux between coil and yoke, whose direction will be given by the temperature gradient:

$$\int B_1 \cdot dl = I_1(T_1^{core}, T_1^{coil}, \Phi_1^{core}, \Phi_1^{coil}, \dot{\Phi}_1^{core}, \dot{\Phi}_1^{coil}) \quad (3.3)$$

$$\int B_2 \cdot dl = I_2(T_2^{core}, T_2^{coil}, \Phi_2^{core}, \Phi_2^{coil}, \dot{\Phi}_2^{core}, \dot{\Phi}_2^{coil}) \quad (3.4)$$

where
$\Phi_j^k$ is the heat flux and
$\dot{\Phi}_j^k$ is the heat flux variation.
If

$$\begin{aligned} T_1^i &\simeq T_2^j \\ \Phi_1^i &\simeq \Phi_2^i \\ \dot{\Phi}_1^i &\simeq \dot{\Phi}_2^i \qquad \text{i=coil,core} \end{aligned}$$

it is likely achievable that

$$\frac{\int B_2 \cdot dl}{\int B_1 \cdot dl} = \frac{I_2}{I_1} \simeq \text{CONSTANT or slightly changing with } T, \Phi, \dot{\Phi} \quad (3.5)$$

The last equation express the aim of the MBI mapping and calibration, as the bending angle and thus the energy will depend only on the ratio between the integrals, whatever their values are.

### 3.4.2 Studies on the Injection Magnets

To get in advance some informations about full-iron core magnets used in the LEP environment, the temperature behaviour of the cores in the injection region was investigated.
Previous studies on a iron-concrete magnet, placed on a test bench in the former ISR tunnel [7], showed a temperature coefficient of the order of $1.2 \cdot 10^{-4}$ $^{o}\mathrm{C}^{-1}$ [7]. With the choice of an iron magnet, one would have expected a much smaller thermal dependence and the presence of some temperature and NMR probes on the injection dipoles was a method to check this point.
In two half cells (see Section 2.1.2 for the definition of half cell) in proximity of the LEP injection region some meaningful temperatures are monitored:

[7] The model developed by E.Bravin et al. is rather complicated, but here it is enough to cite the larger of the coefficients included in the field-temperature dependence.

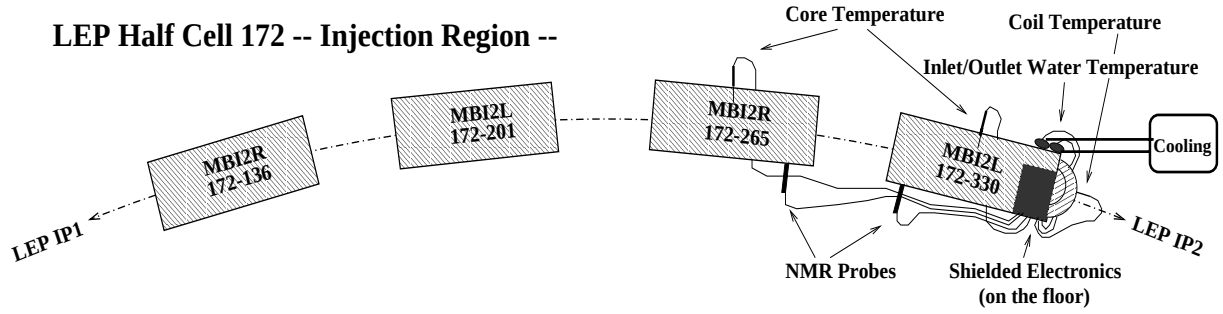


**Figure 3.7**: Layout of the instrumentation for monitoring the magnetic field and some temperatures in one LEP half cell in the Injection region.

1. the inlet water;
2. the coil cooling water at half the circuit;
3. the outlet water;
4. the iron in the core of two dipoles;
5. the air temperature.

Four NMR probes are placed on the lower pole of four iron magnets, two for each Half Cell. The layout of the instrumentation is showed in Fig. 3.7 for one half cell, the other half is symmetric.
The field and temperature monitors were read for a few weeks, collecting several LEP fills of different durations.
A typical plot (Fig. 3.8) shows the magnetic field and the corresponding temperatures versus time. The coil water is following the jumps of the outlet water; that is correlated with the heating of the coil due to the Joule effect caused by the excitation current. The inlet water temperature is slightly increasing, it is regulated in order to keep the temperature of all the cores in the arc constant.
The aim is to find a relation between the temperature and local field changes. Before analyzing such a correlation, it is worth pointing out another factor which was important in these studies. From the first plot of Fig. 3.8 it is evident how the magnetic field in the second fill is much more "noisy" than the first. In fact in Section 2.3.1 the influence of the train current was explained. During this temperature analysis it was possible to verify that effect (Fig. 3.8) after five in the morning.
In Fig. 3.9 the magnetic field change during a fill is displayed together with the measured TGV current and the same magnetic field compensated for the train current [8].
Once this effect is compensated, it is possible to study the correlation between the magnetic field and the core temperature.
The normal operation of LEP consist in repeated filling-physics taking-dumping cycles that lead to thermal cycles too. Usually the machine is "cold" before the injection and the temperature is increasing until the dumping of the beam. The study on the injection magnets shows that the field is increasing for about half an hour after the ramp and then decreasing until the end of the physics period. The temperature coefficient is thus changing sign, from positive to negative during a cycle. The positive correlation is not clearly understood. It can depend on transient effects taking place

[8] A magnetic field proportional to the train current is subtracted from the measured field.

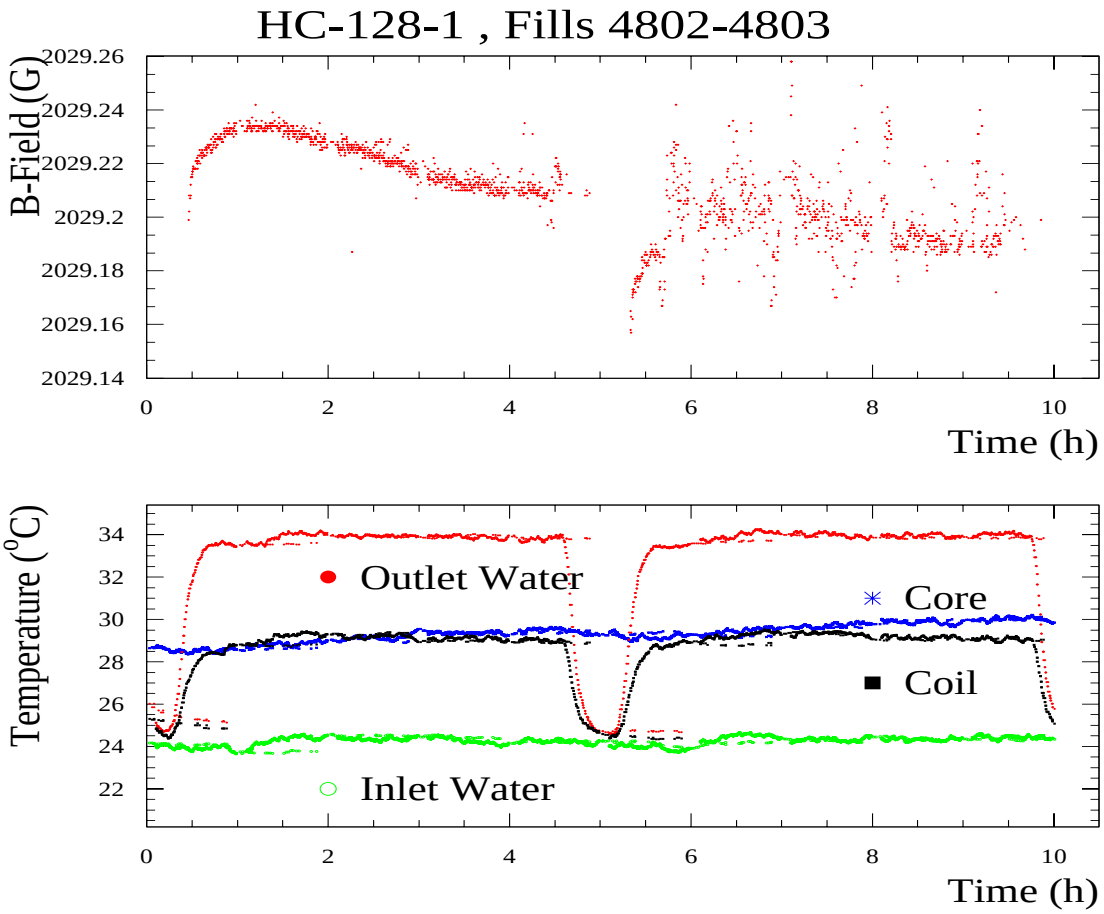


**Figure 3.8**: Typical trend of the magnetic field (top) and four characteristic temperatures (bottom) during two LEP physics cycles.

after the ramp, like temporal changes in the gap aperture due to the change from cold to warm magnet. Another transient effect can be related to the amount of synchrotron radiation which is escaping from the vacuum chamber , even with the lead shielding around the beam pipe [17]. During the ramp between the injection and the physics energies the power dissipated by the photons is increasing of a factor $10^4$ and the temporary relationship between such power, the heating due to Joule effect and the power absorbed by the cooling system can take some time to reach a stable point.
The negative coefficient, in the second and larger part of every physics cycle, can be surely linked to the iron core of the MBI magnets. In particular temperature variation effects on a dipole are:

- variation of the iron permeability;
- variation of the gap of the magnet;
- variation of the length of the magnet.

For example the field decrease can be addicted to an increase of the gap aperture due to the thermal expansion of iron.
The mentioned correlation is visible, looking at the second part of a fill (Fig. 3.10). Hence the aim of the measurement is to determine the typical temperature coefficient, following a classical

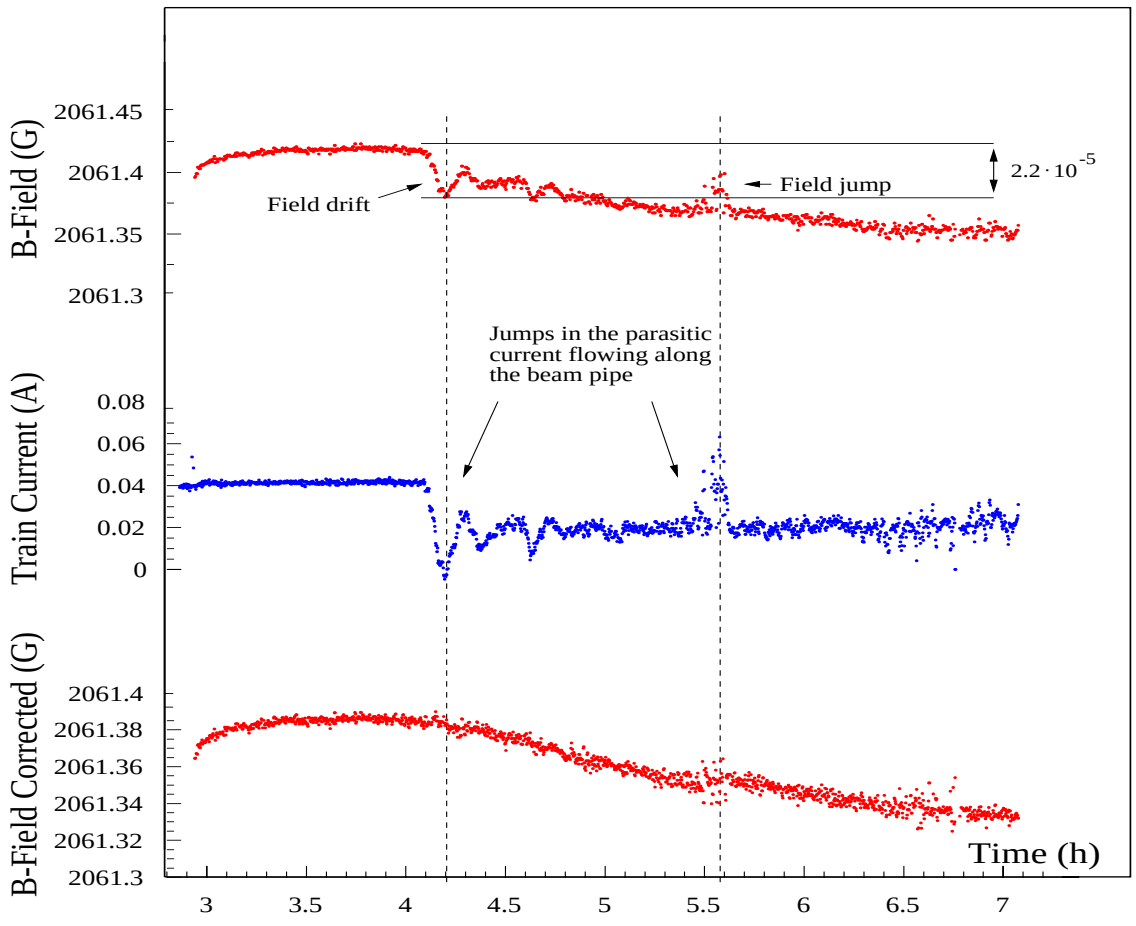


**Figure 3.9**: Example, over a physics fill, of the leakage currents due to the *train effect*.

parameterization. Assuming $t_0$ as the time at the beginning of the period, $T_0 = T(t_0)$ the initial temperature and $B_0 = B(t_0)$ the initial magnetic field, it is possible to predict:

$$B(t) = B_0 \cdot \{1 + C_T \cdot [T_0 - T(t)]\} \quad [G] \tag{3.6}$$

According to this model the temperature coefficient is:

$$C_T = \frac{1}{B_0} \cdot \frac{B(t) - B_0}{T(t) - T_0} = \frac{1}{\Delta T} \cdot \frac{\Delta B}{B_0} \; [^oC^{-1}] \tag{3.7}$$

To evaluate such a coefficient from the measurements on the injection magnets, a linear fit was performed between the two variables, dividing each fill into two parts [9]. Which gives:

$$B(t) = a + b \cdot T(t) \quad [G] \tag{3.8}$$

where $a$ and $b$ are the two fit parameters.
Combining Eq. (3.6) and Eq. (3.8), it is immediate to express the coefficient like:

$$C_T = \frac{b}{B_0} \; [^oC^{-1}] \tag{3.9}$$

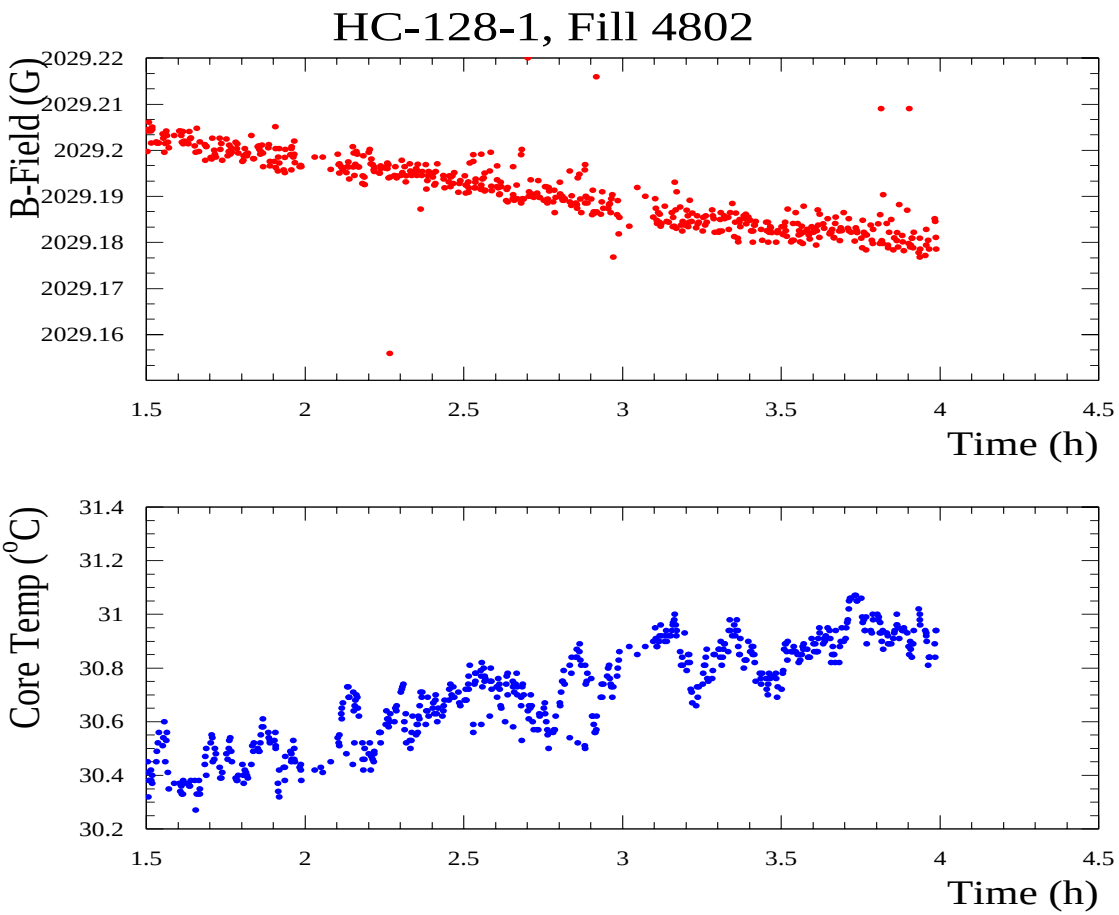


**Figure 3.10**: B-field and Core temperature trend during the second part of every fill

Using this procedure several LEP fills were analyzed, a graphical example is given in Fig. 3.11.

The bottom of the figure is an indicator of the quality of the fit; it shows the residual of every measured point from the linear fit, normalised to the absolute value of the field. The order of such scatter is few $10^{-6}$.
For this particular example [10], the temperature coefficient $C_T$ is $-1.62 \cdot 10^{-5}$ $^o$C$^{-1}$. The same procedure was used for the other fills, obtaining quite consistent results (Table 3.2).
From these measurements a dependence of the order of $1.7 \cdot 10^{-5}$ $^o$C$^{-1}$ can be extrapolated. Independently from an accurate value, it is important outlining the order of magnitude. For each degree of change in the temperature, the field is changing of a factor $10^{-5}$.
Following this philosophy it was possible to estimate the temperature coefficient after the ramp, where the field is still increasing for about half an hour. The results are summarized in Table 3.3.

[9] Chosen arbitrarily every time, identifying a region of about half an hour after the ramp and another one covering the second part of the fill.
[10] Fill 4802, Half Cell 128-1.

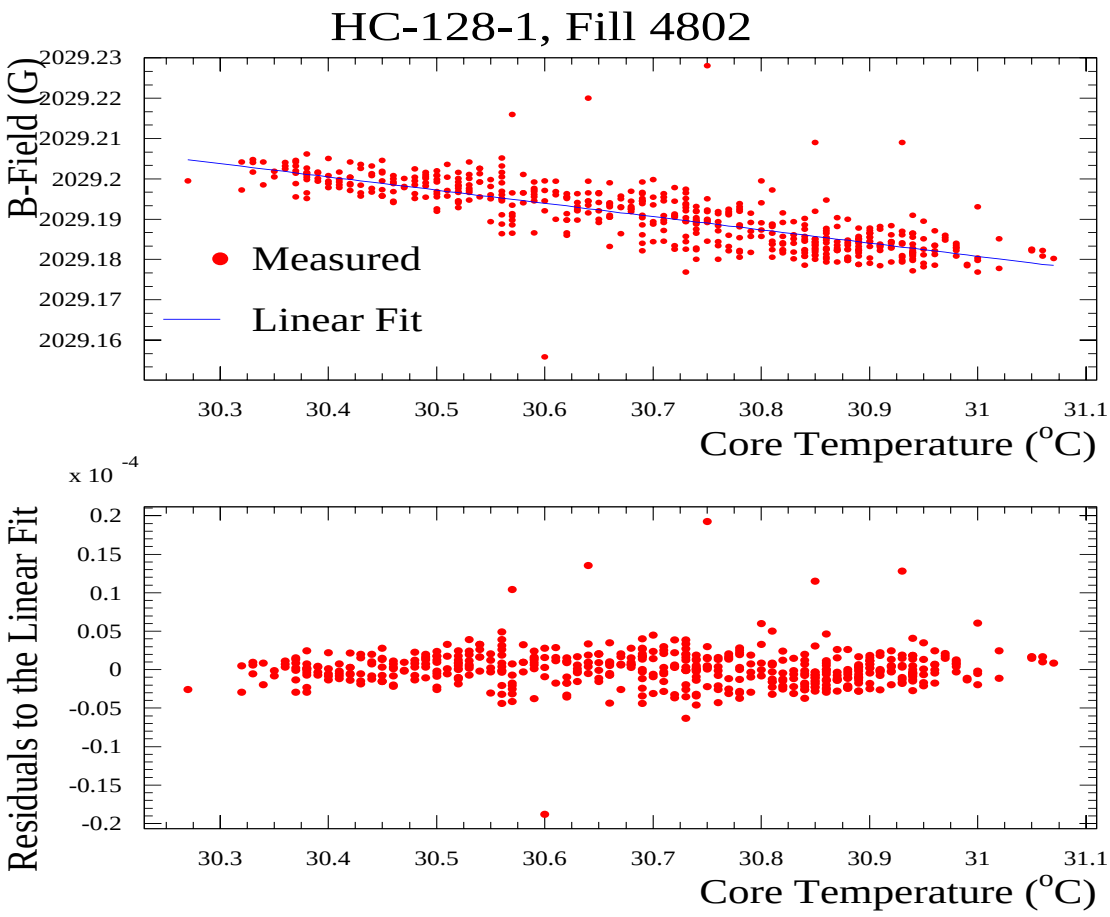


**Figure 3.11**: Linear fitting between temperature and B-field (top) and Residuals to the Linear Fit (bottom).

| LOCATION | FILL # | SLOPE OF THE LINEAR FIT $(G \cdot^o C^{-1})$ | $C_T$ $(^oC^{-1} \cdot 10^{-5})$ |
|---|---|---|---|
| HC-128-1 | 4762 | -0.03509 | -1.729 |
| HC-128-1 | 4766 | -0.04716 | -2.324 |
| HC-128-2 | 4766 | -0.04525 | -2.230 |
| HC-128-1 | 4802 | -0.03286 | -1.620 |
| HC-128-1 | 4803 | -0.03418 | -1.684 |
| HC-128-1 | 4806 | -0.03263 | -1.608 |
| HC-172-4 | 4802 | -0.03621 | -1.783 |
| HC-172-4 | 4803 | -0.03478 | -1.713 |

**Table** 3.2: Temperature coefficient in the "negative" region, for some 1998 LEP fills. The third column represents the first order coefficient of the linear fit.

| LOCATION | FILL # | SLOPE OF THE LINEAR FIT $(G \cdot {}^{o}C^{-1})$ | $C_T$ $({}^{o}C^{-1} \cdot 10^{-5})$ |
|---|---|---|---|
| HC-128-1 | 4762 | +0.03230 | +1.590 |
| HC-128-1 | 4766 | +0.07466 | +3.670 |
| HC-128-1 | 4802 | +0.04345 | +2.112 |
| HC-128-1 | 4803 | +0.02169 | +1.061 |
| HC-128-1 | 4806 | +0.01451 | +0.715 |
| HC-172-4 | 4802 | +0.02642 | +1.301 |
| HC-128-1 | 4973 | +0.04578 | +2.256 |

**Table** 3.3: Temperature coefficient in the "positive" region, for some 1998 LEP fills.

### 3.4.3 Conclusions

The field-temperature correlation is not unambiguously described with one model for all the variations of the magnet temperatures and current excitations during the LEP operation. For example the *initial* point of every fill is very important. Depending on how long the machine remains "cold" before the ramp, the temperature reached after the ramp and the time constant for the following thermal drift can change. Since it is not possible to monitor the temperature of the magnet yoke "everywhere", a complete prediction of the integral magnetic field using variable temperature and excitation values of the magnet is not feasible. The prediction of the integral using several B-field measurement locations (NMR probes) has the advantage that the B-field changes due to local temperature variations result as taken into account. It is still possible that the correlation between the integral B-field and the local B-field is ambiguous because the field is sampled only in few locations which may not represent the average B-field variation. The thermal behaviour of the magnet is not uniform or linearly changing along its dimensions, due to the asymmetric shape and geometry. The results from the temperature-field studies underline the strong influence of the temperature variation on the ambiguous B-field changes.

i. the thermal response of the magnet is not uniform or linearly changing along the magnet dimensions, due to its asymmetric shape and geometry;

ii. the temperature gradient in the core can be estimated as $\approx 0.8 \div 1\ {}^{o}C/h$;

iii. the absolute value of the core temperature[11] can range from 26 to 31 ${}^{o}C$.

Taking these observations into account and, on the other hand recalling the requirements for the energy calibration with the spectrometer, means that

I. determining the energy difference (or ratio) between 41 GeV and the operational LEP energy (98 GeV in 1999);

II. measuring the relative energy changes during a fill,

[11] Considering several initial conditions.

leads to the conclusion that the temperature behaviour of the magnet is critical.
These requirements lead to an estimate of the period during which it is necessary monitoring the magnetic field, and in particular about 2 hours for case I, where the energy at 41 GeV has to be calibrated with the resonant depolarisation method, and a time of 5-10 hours for case II.
Such considerations take to the conclusion that the temperature increase in an iron core magnet cooled by the normal LEP temperature regulation system would be at least of $1 \div 1.5\,^oC$ during the energy calibration. That means some $10^{-5}$ of relative change in the magnetic field. Without an efficient temperature regulation, would mean having calibration field maps in the the temperature range within $6 \div 7\,^oC$ with a resolution of $1\,^oC$ for each energy. A large number of mappings would have been necessary.

It was so decided to install a dedicated temperature regulation for the spectrometer magnet. The idea is to keep the temperature gradient of the magnet inside $\pm 1\,^o$C for the whole energy calibration period, at different energy levels, maintaining the secondary water temperature constant and modulating the water flux during the energy ramps, keeping in such a way the heating extraction proportional to the power dissipated.

# Chapter 4

# Magnetic Measurements

In the particle accelerators technology magnetic measurements concern two main branches: beam guiding focusing magnets and solenoids magnets.
Different measurement techniques have been developed in the years, mainly based on Faraday's law about electromagnetic induction, the Hall effect and the nuclear magnetic resonance properties of some materials.
Each method can be alternative to an other, and very often also complementary in the field range where more than one method is available. High accuracy requirements on the measurement can in fact suggest to use different instruments in order to optimize the operational ranges and to reduce the uncertainties on the results.
An overview of the accuracy and range of the different methods is shown in Fig. 4.1.
The following two paragraphs will introduce the searching coil and the Nuclear Magnetic Resonance (NMR) methods, since they are used for this thesis work. Further information on magnetic measurements can be found for example in [18].

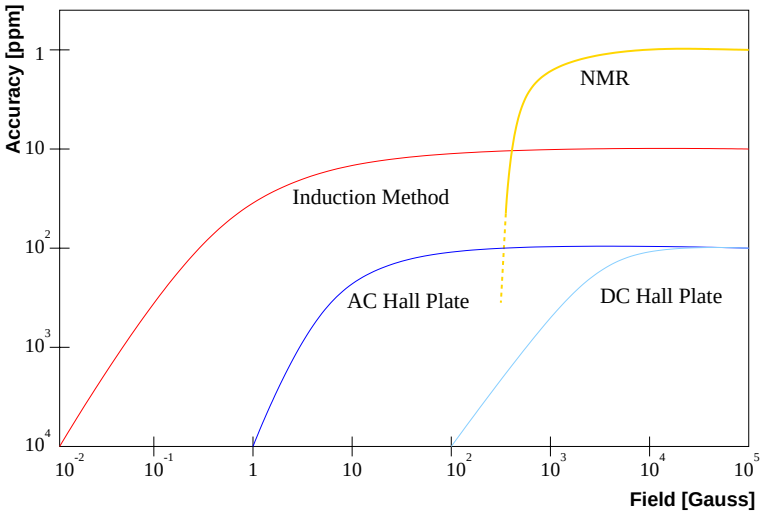


**Figure 4.1**: Accuracies and ranges of the different magnetic field measurements methods.

## 4.1 Search Coils

The magnetic field measurement can be traced back to a magnetic flux. Any magnetic flux meter can thus be considered a mean for the magnetic field detection. A *search coil* represent a practical way to perform this kind of measurement.
The principle of operation is based on Faraday's law which is asserting that the time integral of the voltage induced in a coil subjected to a change in magnetic field is a measure of the change of the flux linking the coil (Fig. 4.2):

$$\Phi = \int_S \vec{B} \circ \vec{ds} = \int_S B\, ds\, cos\theta \quad [Vs] \tag{4.1}$$

$$\Delta V = -\frac{d\Phi}{dt} \quad [V] \tag{4.2}$$

Such flux variation can be produced in different ways:

i. the coil is static and the magnetic field is changing (i.e. ramping the current of an electromagnet);

ii. the coil is moving (sliding or rotating) in a static field;

iii. the magnetic system is changing (i.e. flipping of a permanent magnet).

In any case the sensor can be a coil acting as *flux loop*. The two basic requirements for the operation are that the coil must not contain conductor materials and that it must remain rigid.
The first point insures that the flux change is not affected by the sensor itself and the second guarantees that the the relation between flux and magnetic field, Eq. (4.2), does not change due to variations in the surface to which the flux is linked.
Several methods have been developed to use this kind of measurements for the mapping of the particle accelerator magnets. They can be divided in point, gradient, harmonic and period coils [18].

For the mapping of the spectrometer dipole magnet a sensor of the type *point coil* has been mounted on the travelling mole. Such coil is suitable in homogeneous fields, where the field lines are parallel. The measurement has been performed in the end-field region where the magnitude of the dipole field is changing from zero to the nominal field inside the magnet. In

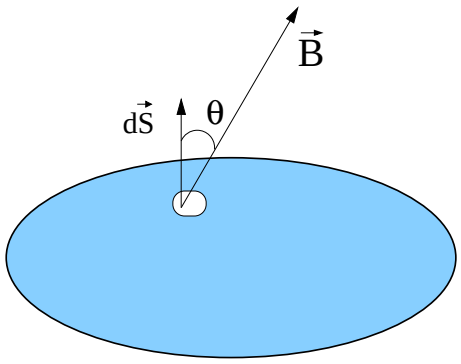


**Figure 4.2**: A search coil forms a loop to which the flux is linked.

each step the detected voltage was thus proportional to the magnetic field change according to Eq. (4.2) and Eq. (4.2).
In order to get an induced signal

$$\Delta\Phi = S \cdot B \cdot \frac{\Delta B}{B} \tag{4.3}$$

high enough to be properly integrated by the electronics (digital integrator), about 1000 turns have been made on the same frame, as described in chapter 5.
From the electrical point of view it is important to give few fundamental points to be followed during the measurements:

a) the initial and final point of the *time integration* must be known with an high accuracy, since they affect directly the error of the measurement;

b) possible *noise* coming from the wires and connections between the sensor and the electronics must be checked and in case reduced to the minimum;

c) the so called *drift* must be compensated or corrected.

This last point refers to the fact that some noise in the electronics (included the thermal noise) can produce a spurious signal even when there is not any change in the magnetic flux and thus any induced voltage signal. The correction for the drift can be done with

i. a linear correction with time;

ii. a repetition of the measurement reversing the role of the initial and final points.

In the first case one must assume that the drift is constant, at least for the time in which the same correction factor is used. In the second case the assumption is that the defect is reproducible during the two measurements.
In the travelling mole setup (see chapter 5) the drift was continuously measured and compensated by an external DAC which was producing a voltage equal to the drift but with opposite sign. The drift has been anyway recorded before and after each measurement step and a correction of the type i has been included in the data analysis.

## 4.2 NMR Probes

The first experiments on *nuclear magnetic resonance* (NMR) have been carried out in the same period by F. Bloch [19] at Stanford University and E.M. Purcell [20] at Harvard University beginning from 1946. Since that time magnetic resonance became a method worldwide used to investigate the properties of magnetic fields.
Furthermore it is nowadays one of the most fruitful tools for basic research in chemistry and is commonly used in medicine in the form of *magnetic resonance imaging* [1] (MRI) which provides non invasive pictures of the soft tissues of living beings.

### 4.2.1 The NMR Effect

The magnetic resonance is an effect which occurs if a particle (proton, deuteron, electron, muon) with spin $\vec{S}$ and angular momentum $\vec{L}$ is exposed to a stationary and a time dependent magnetic fields superimposed. The spin precession is disturbed if the spin precession frequency and the frequency of the time dependent field are identical. A particle has a magnetic moment given by:

$$\vec{\mu} = \gamma\hbar\vec{S} = \gamma\vec{L} \tag{4.4}$$

where $\hbar = h/2\pi$, *h* is the Planck's constant and

$$\gamma = \pm\frac{|\vec{\mu}|}{\hbar|\vec{S}|} \tag{4.5}$$

is the gyromagnetic ratio, typical of the particle. The sign of $\gamma$ in Eq. (4.5) is + or - according to whether $\vec{\mu}$ is parallel or anti-parallel to $\vec{S}$ respectively.
A sample of a material with magnetic moment and angular momentum in a magnetic field $\vec{B}$ exhibits a precessional motion [2] whose precession frequency (*Larmor frequency*) is

$$\nu_L = \frac{\omega_L}{2\pi} = \frac{\gamma}{2\pi}|\vec{B}\,|. \tag{4.6}$$

The principle of magnetic measurements via the NMR method resides in Eq. (4.6): measuring $\nu_L$ and using the well-known value of $\gamma$ it is possible to estimate $|\vec{B}\,|$.
There are two approaches to this type of measurement [21]:

i. a quantum mechanical spectroscopic absorption measurement;

ii. the classical precession of a particle with a magnetic moment and angular momentum in a magnetic field.

In the typical magnetic resonance measurement one considers the spins of an ensemble of particles (i.e. protons) in a magnetic field which has a large static component in the vertical direction ($B_0$) and a superimposed small oscillating component in the x direction ($2B_1 cos(\omega t)$).
There are two methods to perform a nuclear magnetic resonance experiment. Either by variation of the external vertical field $B_0$ or by changing the frequency $\omega$ of the superimposed transversal field. The latter is the method used at LEP, being the external field what one wants to measure and thus fixed. In both cases the resonance condition is fulfilled when the spin precession frequency and the frequency of the field varying with time are identical.

[1] The original denomination *nuclear magnetic resonance imaging* was deprived of the term "nuclear"
[2] It is something similar to a gyroscope in a gravitational field

### 4.2.2 Quantum Mechanical Description

The quantum mechanical analysis is a steady state absorption of energy measurement in the frequency domain, i.e. a spectroscopy experiment in which the frequency (or magnetic field) is varied through a narrow absorption line. The center of the line is then used to calculate the magnetic field. The quantum mechanical Hamiltonian operator **H** for a magnetic moment $\vec{\mu}$ in a magnetic field $\vec{B}$ $(2B_1 cos(\omega t), 0, B_0)$ is:

$$\begin{aligned} \mathbf{H} = -\vec{\mu} \cdot \vec{B} &= -\hbar\gamma[S_z B_0 + 2S_x B_1 cos(\omega t)] \\ &= -\hbar\gamma S_z B_0 - \frac{\hbar\gamma B_1}{2}(S^+ + S^-)(e^{j\omega t} + e^{-j\omega t}) \end{aligned} \tag{4.7}$$

being $S^+ = S_x + iS_y$ and $S^- = S_x - iS_y$. According to this representation (quantization along the z-axis) the first term on the right hand side of Eq. (4.7) determines the steady state energy levels of the system, while the second part describes the transition between different energy states.
Therefore the energy levels are

$$E_n = \hbar\gamma m B_0; \quad m = -S, -S+1, \ldots, S \tag{4.8}$$

For proton samples the possible spins are $\pm\frac{1}{2}$ and only two energy levels are possible (spin vector parallel or anti-parallel with respect to $\vec{B}$ ).
The energy difference between two steady states follows from Eq. (4.8) and Eq. (4.6):

$$\Delta E = \hbar\gamma B_0 = \hbar\omega_L \tag{4.9}$$

The energy levels depends thus only on the constant vertical field $B_0$. Within the framework of this description, the observation of a magnetic resonance signal corresponds to a spectroscopy measurement in which the system in a large magnetic field $B_0$ is irradiated by a small oscillating field ($2B_1 cos(\omega t)$). When $\hbar\omega$ matches $\Delta E$ resonant absorption can occur. In this case $\omega = \omega_L$ and $B_0$ can be calculated from Eq. (4.9).
The absorption signal always has a finite width $\Delta B$ in field and $\Delta\omega$ in frequency. One reason for that is the inhomogeneity of the field which has a width $\delta B$ over the volume of the sample, thus producing a broadening of the signal. A second reason can be the finite lifetime of a single spin state. This is due to interaction between the sample and the materials surrounding it (the so called *lattice*) or interactions with other spins, like the dipole-dipole interactions. This latter effect is normally the dominant factor in the width of the NMR absorption signal which is affecting the B-field measurement accuracy.

### 4.2.3 Classical Magnetic Resonance Precession

Despite the quantistic mechanical nature of the NMR effect, the time evolution of the measured signal can be described by classical equations. This is possible because the signal arises from the combination of a huge number of single magnetic moments. At thermal equilibrium the magnetic moments $\mu_i$ of the nuclei in a sample add up to a static macroscopic magnetic moment (also defined as *magnetization*)

$$\vec{M} = \sum_i \vec{\mu_i}. \tag{4.10}$$

When the sample is in the magnetic field $\vec{B}$ $(2B_1 cos(\omega t), 0, B_0)$ $\vec{M}$ results to be parallel and proportional to $B_0$. This vector obeys the following equation of motion:

$$\frac{d\vec{M}}{dt} = \vec{M} \times (\gamma \vec{B}\ ) \tag{4.11}$$

Bloch equations describe the evolution of $\vec{M}$ separating its components:

$$\begin{aligned} \frac{dM_x}{dt} &= \gamma(M_y B_0 + M_z B_1 sin(\omega t)) - \frac{M_x}{T_2} \\ \frac{dM_y}{dt} &= \gamma(M_z B_1 cos(\omega t) - M_x B_0) - \frac{M_y}{T_2} \\ \frac{dM_z}{dt} &= \gamma(-M_x B_1 sin(\omega t) - M_y B_1 cos(\omega t) - \frac{M_z - M_0}{T_1} \end{aligned} \tag{4.12}$$

in which $M_0$ is the magnetization in the z-direction at thermal equilibrium. The behaviour of $\vec{M}$ under the influence of the oscillating field of frequency $\omega \approx \omega_L$ is better described in a coordinate system rotating relative to the laboratory frame with frequency $\omega$, about the direction of $B_0$. This corresponds to a transformation which makes $x \to u$ and $y \to v$. In the new reference frame the Bloch equations become:

$$\begin{aligned} \frac{dM_u}{dt} - (\omega_L - \omega)M_v &= -\frac{M_u}{T_2} \\ \frac{dM_v}{dt} + (\omega_L - \omega)M_u - \omega_1 M_z &= -\frac{M_v}{T_2} \\ \frac{dM_z}{dt} + \omega_1 M_v &= -\frac{M_z - M_0}{T_1} \end{aligned} \tag{4.13}$$

where $\omega_L = \gamma B_0$ (Eq. (4.6)) and $\omega_1 = \gamma B_1$.

**Solution of Bloch equations**

An approximate solution of Bloch equations can be calculated assuming a slow passage through the resonance, where the magnetization is constant,

$$\frac{dM_z}{dt} = \frac{dM_u}{dt} = \frac{dM_v}{dt} = 0 \tag{4.14}$$

In such case the system is in constant thermal equilibrium, because the relaxation times $T_1$ and $T_2$ are very small, and the magnetizations result to be

$$\begin{aligned} M_u &= M_0 \frac{\omega_1 T_2^2(\omega_L - \omega)}{D + T_2^2(\omega_L - \omega)^2} \\ M_v &= M_0 \frac{\omega_1 T_2}{D + T_2^2(\omega_L - \omega)^2} \\ M_z &= M_0 \frac{1 + T_2^2(\omega_L - \omega)^2}{D + T_2^2(\omega_L - \omega)^2} \end{aligned} \tag{4.15}$$

with $D = 1 + \omega_1^2 T_1 T_2$. For the case of weak radio fields where $\omega_1^2 T_1 T_2 \ll 1 (\Rightarrow D \approx 1)$ the solution for the transverse magnetization $(M_u, M_v)$ is identical to the one for a classical harmonic oscillator. $M_v$ represent the absorption and $M_u$ the tangent of its phase. Displaying the transversal magnetizations as function of $T_2(\omega_L - \omega)$ (Fig. 4.3) it is visible how when the resonance applies $(\omega = \omega_L)$ $M_v$ has a maximum and its derivative $M_u$ has a minimum. Measuring in such way the Larmor frequency allows to calculate the B-field $B_0$.

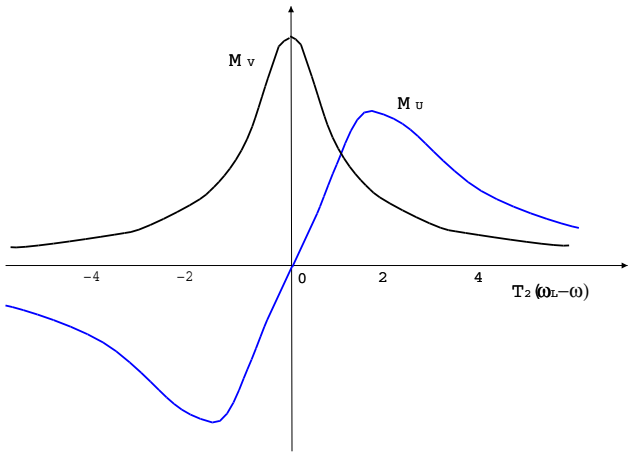


**Figure 4.3**: Transverse magnetization as function of the quantity $T_2(\omega_L - \omega)$.

### 4.2.4 NMR Probes at CERN

Two main layouts for the instrumentation architecture are commonly used for the nuclear magnetic resonance measurements: the typical absorption configuration and the pulsed NMR. Presently at LEP the NMR probes and instrumentation are provided by the firm Metrolab (Geneva) and are developed according to the first method described above (absorption).

The circuit concerning the NMR probe itself is presented in Fig. 4.4. The coil in the probe head

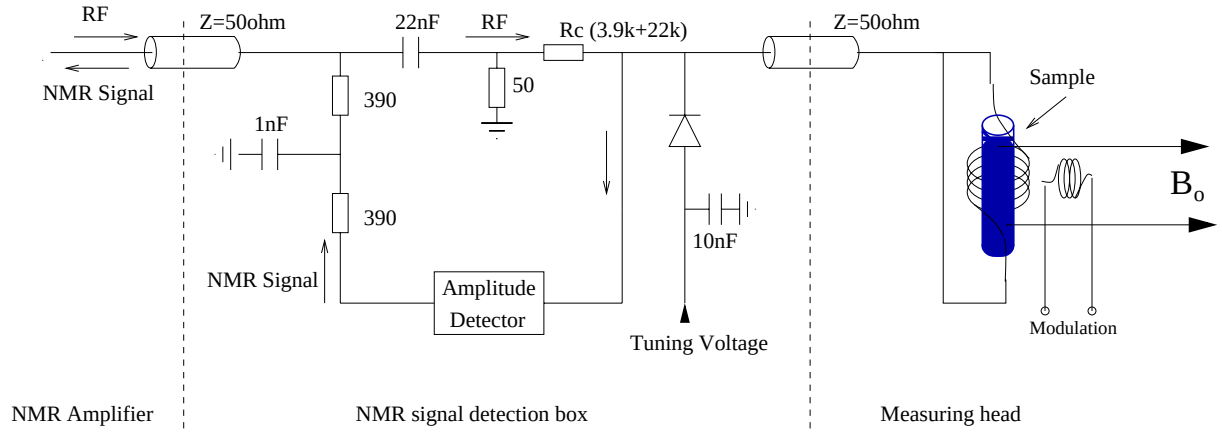


**Figure 4.4**: Circuit of the Metrolab NMR probe head.

is filled with a material which shows nuclear resonance when placed in a magnetic field. It can be a solid material or sometimes water. In each case the fundamental element is hydrogen which is providing the protons that orient their spin according to the magnetic field, as explained above.

The practical way to detect the magnetic resonance consist in tuning a parallel LC resonant circuit to the proton resonance frequency and to apply to this circuit a stable sine wave of that frequency via a resistor. When the coil is tuned to the proton resonance frequency the quality factor Q of the coil is slightly reduced. The reduction of the Q factor due to the proton resonance can be detected

as a small amplitude variation of the radio frequency voltage across the circuit.
Such signal is very small and very often masked by low frequency noise. This problem can be solved by adding a modulating magnetic field $B_M cos(\omega_M t)$ parallel to the static field $B_0$ and follow the amplitude detector with a lock-in (phase coherent) detector. The effect of the modulation is to shift the frequency of the detected signal up to $\omega_M$ where the signal to noise ratio is improved. When $B_M \ll \Delta B$ (modulation amplitude much smaller than the line-width), the output of the lock-in traces the derivative of the absorption.
In Fig. 4.5 both the absorption signal and its derivative are shown. The modulating field $B_{mod}$ is

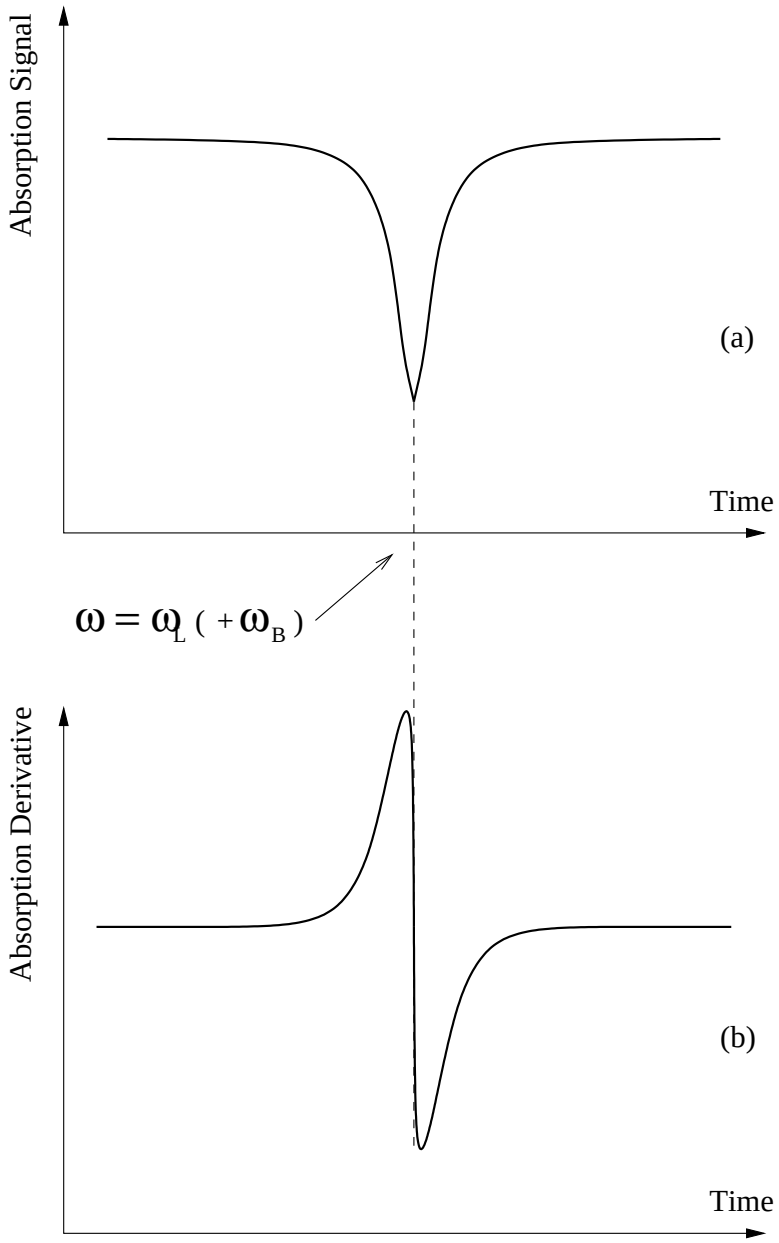


**Figure 4.5**: Absorption signal detectable when magnetic resonance occurs (a) and its derivative (b) which is the actual measured signal. Both plots are ideal (no noise) and not scaled. The advantage of a lock-in circuit is, in fact, the larger amplitude of the derivative with respect to the real absorption signal.

produced by a small, flat coil inserted in the probe. Its frequency is in the range $30 \div 70\,Hz$ and its amplitude in the range $100 \div 1000$ ppm of $B_0$. The NMR electronics detects and amplifies the nuclear resonances signals of the LC circuit and measures the current in the modulating coil at the instant when resonance occurs.
A voltage-controlled oscillator produces the radio frequency voltage. Its frequency is controlled by a high-gain feedback loop to ensure that resonance occurs at the instant when $B_{mod}$ crosses zero. Therefore this frequency equals the proton resonance frequency of $B_0$ (i.e. the Larmor frequency) and automatically follows any changes in $B_0$.
The LC circuit is automatically tuned to the applied frequency by means of a varicap diode.
Further detail about the instrument electronics and operation can be found in [3].

### 4.2.5 Accuracy and Limitations

Some considerations about the accuracy of the nuclear magnetic resonance can be estimated using Eq. (4.6). As mentioned above one source of uncertainty resides in the broadening of the absorption line typical of the magnetic resonance experiment. Such broadening effects (due to field non-homogeneity and finite spin life time, see section 4.2.2), are an important limitation on how accurate can be the measurement of the field $B_0$. The larger $\Delta B$, the poorer the accuracy with which $B_0$ can be measured.

In [22] some considerations are made about the potential accuracy of magnetometers based on NMR. Such analysis cites how the width of the resonance line $\Delta\omega_{1/2}$ (FWHH) is directly related to the transversal relaxation time $T_2$ introduced in the Bloch equations (Eq. (4.13)), being $\Delta\omega_{1/2} = 2/t_2$. The relaxation times for the proton magnetization in pure water at room temperature are $T_1 = T_2 \approx 3\,\text{s}$, corresponding to a line-width $\Delta\omega_{1/2} \approx 2\pi \cdot 0.1\,\text{Hz}$. In a field of 0.2 T[3] $\omega_L \approx 65\,\text{MHz}$, which gives a quality factor for this resonance

$$\frac{\omega_L}{\Delta\omega_{1/2}} \approx 1 \cdot 10^8 \tag{4.16}$$

The knowledge of the gyromagnetic ratio $\gamma$ does not introduce significant contributions to the error.

For the instruments used in the spectrometer magnet mapping, the guaranteed accuracy is better than $\pm 5$ ppm and the relative accuracy better than $\pm 0.1$ ppm in uniform fields [3]. The resolution is $1 \cdot 10^{-7}$ T (or 1 Hz). Larger errors are excluded since the teslameters automatically detect when the resonance signal is good enough to consider the field "uniform". Each measurement waits for such signal (NMR lock) before proceeding with the data taking.

[3] This is the order of magnitude of the B-field in the LEP spectrometer magnet at beam energies of about 100 GeV.

### 4.2.6 Radiation Damages

The several NMR probes installed along the LEP ring for the beam energy calibration aims (see Section 2.2.2) are subject to the synchrotron radiation emitted by the $e^+ - e^-$ beams circulating in the machine. This can cause the ionisation of the materials adopted as sensible samples in the NMR heads and a consequent broadening of the resonance. Some probe types using water were abandoned because the synchrotron radiation intensity caused the water almost to boil.
A new generation of NMRs using rubber-type material is the current solution adopted in the LEP machine.
The plots of Fig. 4.6 and Fig. 4.7 show the effect of synchrotron radiation on the NMR probe performance. The amplitude of the resonance signal is in fact heavily reduced (of about a factor 3) after the probes permanence in the LEP tunnel.

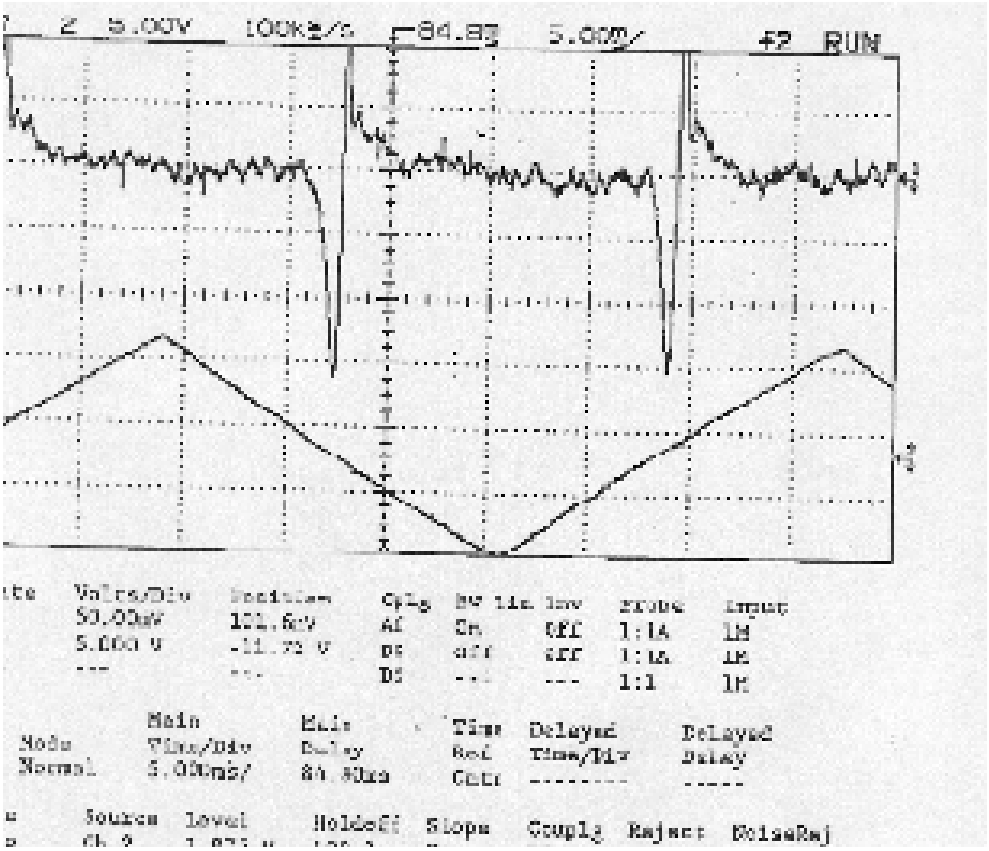


**Figure 4.6**: Resonance signal of a new Metrolab NMR probe.

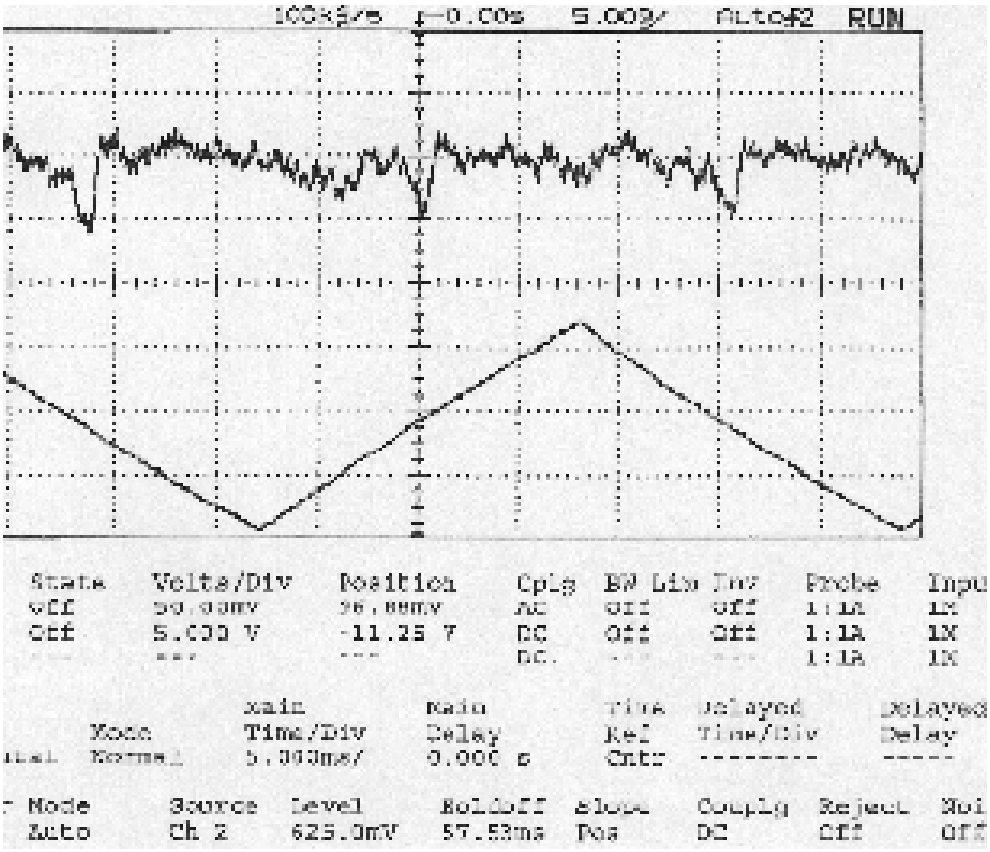


**Figure 4.7**: Resonance signal of the same probe of Fig. 4.6 after a permanence in the LEP tunnel under the influence of synchrotron radiation.

# Chapter 5

# Measurement System

This chapter will describe the measurement system developed for the mapping of the spectrometer dipole magnet.
The map of a dipole magnet is defined as the integral of the B-field along the length of the magnet, $\int_{s_1}^{s_2} Bds$, where *s* is the longitudinal coordinate[1]. The limits of the integration ($s_1$ and $s_2$) must reside outside the magnet core, where the field is sufficiently small (i.e. the non-measured field must have a relative contribution well below $1 \cdot 10^{-5}$ of the total integral B-field).
In order to determine the total $\int Bdl$ , two main categories of measurements can be identified:

i. a long coil system, evaluating directly the integral B-field;

ii. a system which measures the B-field at many well known locations.

The first method implies the integration of the voltage induced on the coil by its movement in the magnetic field. Such system needs frequent re-calibration during the measurements, to achieve the required accuracy of few $10^{-5}$. The other technique (5.5) can use NMR or Hall probe instruments which determine the average magnetic field on an area of few mm$^2$. Only NMR probes guarantee an absolute accuracy of $0.5 \cdot 10^{-5}$ and a relative reproducibility of better than $10^{-6}$ [3]. The measurement range of the commercially available NMR probes starts from 0.04 T, which excludes the determination of the fringe fields. the Hall probes instruments have a lower range of $1 \cdot 10^{-5}$ T, but their relative accuracy is not exceeding $1 \cdot 10^{-4}$ .
Applying the technique of the local B-field determination to calculate the total $\int Bdl$ , an accurate knowledge of the measurements location is needed. The integral is in fact approximated with a sum, like in the following equation:

$$\int_{s_1}^{s_2} B(s)ds \approx \sum_{i=1}^{N} B_i \cdot \delta s_i \tag{5.1}$$

where
$$\begin{cases} s = s_1 \Longrightarrow i = 1 \\ s = s_2 \Longrightarrow i = N \\ \sum_{i=1}^{N} \delta_i = \mathrm{L} \\ \mathrm{L} = \text{total length on which the field is integrated.} \end{cases}$$

[1] Such integral is sometimes indicated as $\int Bdl$ , with the implicit meaning that the integral is performed along the length of the magnet.

In order to keep the relative contribution of the position measurements small compared to the total error of the integral determination, the quantity $\Delta(\delta s)/\delta s$ must be smaller than $1 \cdot 10^{-5}$ .

For the determination of the spectrometer integral field two measurement systems have been set up. The first for a long mapping campaign in the laboratory, to scan all the accessible parameters of the magnet. The main components of this test bench were NMR probes, Hall plates and an electronic ruler to allow the length measurements. The NMR probe for the central field monitoring and the Hall plate for the fringe field were mounted on a carbon arm which was sliding on a marble bench. The ruler was fixed on the same marble bench and a sensor was sliding with the measurement arm (see also Section 3.2.3).
This system is not transportable and does not allow measurements inside the vacuum chamber[2].

In order to check the total integral value inside the vacuum chamber and, even more important, to investigate the magnetic field after the magnet transportation from the laboratory to the LEP tunnel, a second measurement system was designed and commissioned.
This system also uses NMR probes for the central region of the core, and a searching coil for the end field regions. Both instruments are mounted on a small wagon (*mapping mole*), see section 5.1.1, which is moving inside the beam pipe. The mole is pulled by a toothed belt driven by a stepping motor. The field monitors locations are measured by a laser interferometer (see section 5.1.2), through a retroreflector installed on the mole. The fringe field is evaluated integrating the voltage induced on the searching coil while moving in the end regions.

[2]The vacuum pipe was not mounted during such measurements.

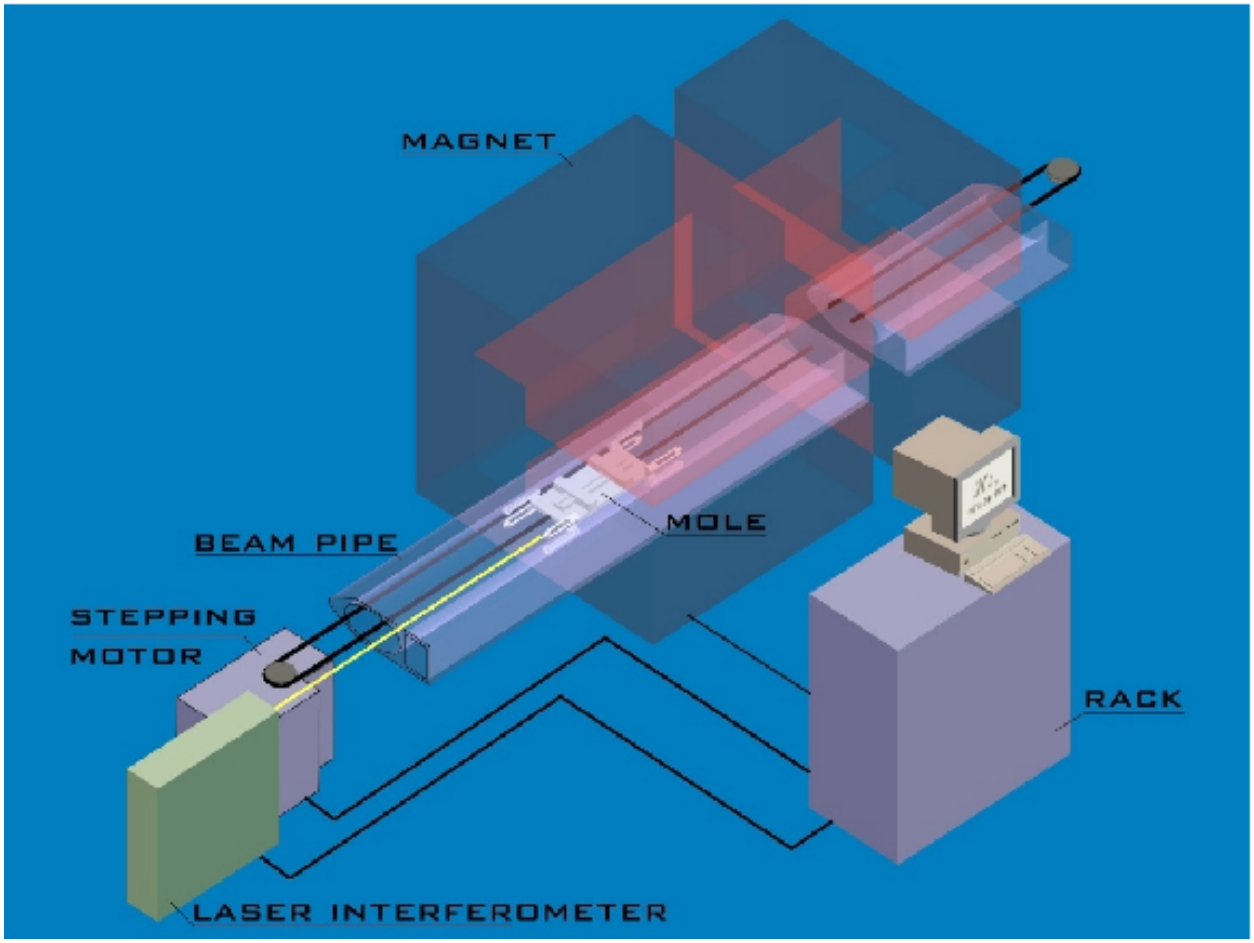


**Figure 5.1**: Test Bench layout

## 5.1 Test Bench

The measurement system was set up initially in the laboratory located at ground level in the former ISR accelerator tunnel, where some equipment was already installed for previous experiments on a normal iron-concrete LEP bending magnet, and the spectrometer dipole was placed for the mapping campaign before the transportation in the LEP tunnel. In Fig. 5.1 the test bench layout is displayed.

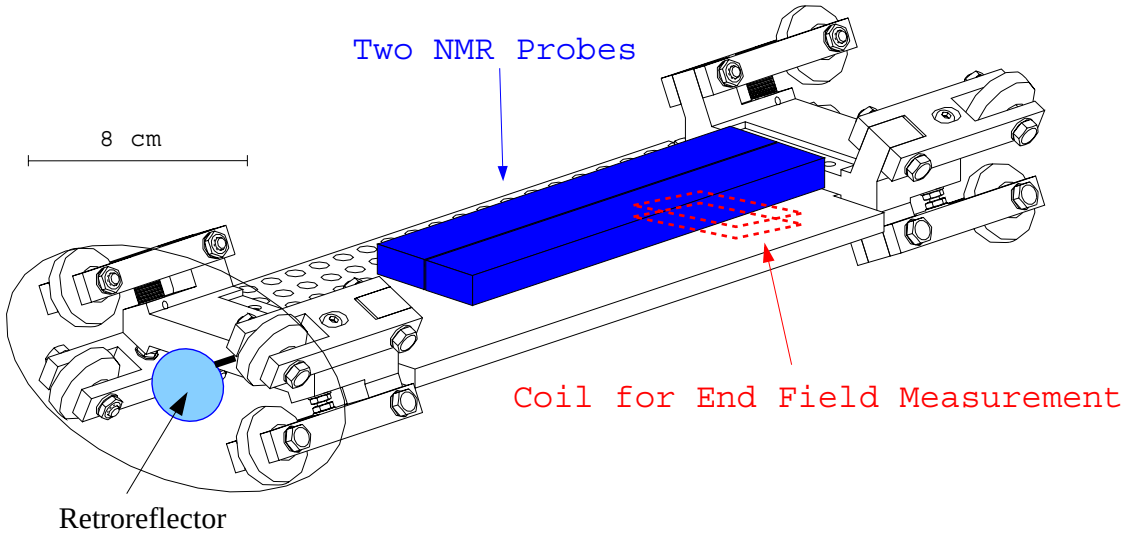


**Figure 5.2**: Schematic diagram of the mapping mole.

### 5.1.1 Mapping Mole

The chariot has been constructed with non-magnetic materials[3] .
Four bronze-beryllium springs are inserted in the upper wheels support, in order to keep the trolley stably pushed against the vacuum pipe walls. The vacuum chamber in the spectrometer magnet is lifted up of 2 mm from the center of the dipole yoke, in order to guarantee enough space between the lower pole tip and the beam pipe for the four fixed NMR probes. The alignment was carefully studied and the geometry was designed to put the NMR probes and the searching coil in the center[4] of the dipole gap, making them slide along the ideal beam trajectory.

The aperture between the wheels supports was studied in order to minimize the possible mechanical instabilities, in particular the torsion of the mole along the longitudinal axis. Taking the center of the transversal section of the beam pipe as center of rotation, the torsion would be along the tangent of the circumference passing through the contact points between the wheels and the vacuum chamber. The physical movement can take place only along the elliptical section of the chamber (Fig. 5.3). Looking at Fig. 5.5, the most stable condition appears when the difference between the slopes of the tangents to the circumference and to the ellipse (i.e. the angle $\alpha$) is minimum. The variations of the angles of interest is shown in Fig. 5.6. The choice of the aperture $\theta$ was therefore done in order to stay as close as possible to the maximum of $\alpha$, compatibly with the practical problems connected with the manufacturing of the mole. The points where the wheels touch the beam pipe correspond to $x = \pm 46$ mm (see Fig. 5.3). Two different views are included in Fig. 5.7, while a schematic diagram of the mole is shown in Fig. 5.2.

[3] Details on the magnetic behaviour of matter can be found for example in [23]

[4] More precisely: the two NMR probes are in the vertical center and symmetrically positioned with respect to the horizontal center.

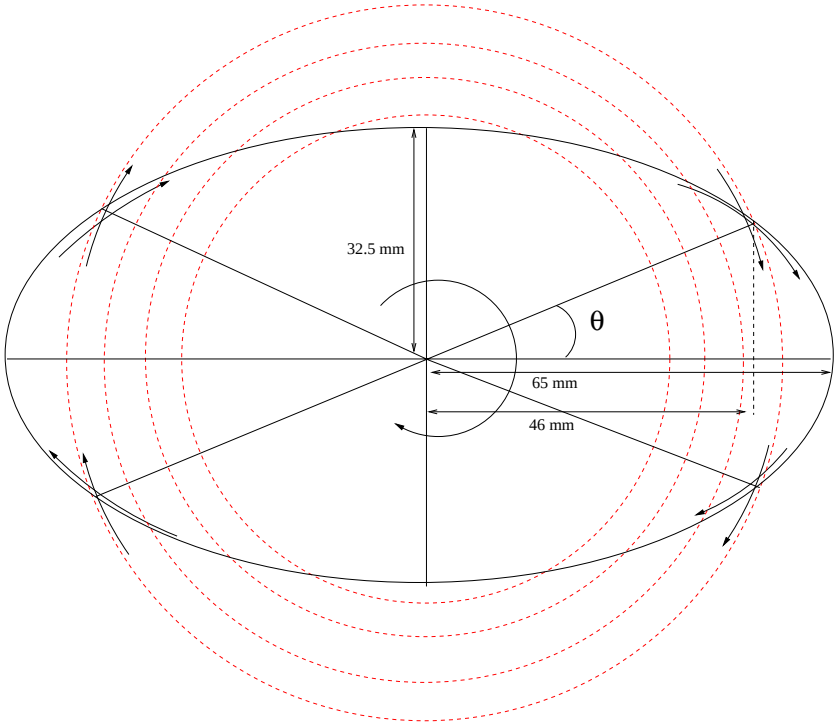


**Figure 5.3**: Diagram of the possible mole rotation.

The mole is pulled by a toothed belt driven by a stepping motor (see Section 5.3). The belt has been chosen to have good elastic properties and stable behaviour in time and temperature changes. A special internal structure in kevlar (non magnetic material) was preferred to the standard steel one. The profile of the belt is illustrated in Fig. 5.4. The two ends of the belt are clamped at the extremities of the mole and two pulleys (one fixed on the stepping motor axis) are mounted externally the vacuum chamber to make the belt turn and close the loop.

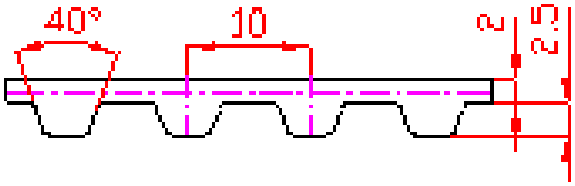


**Figure 5.4**: Profile of the belt used to pull the mole.

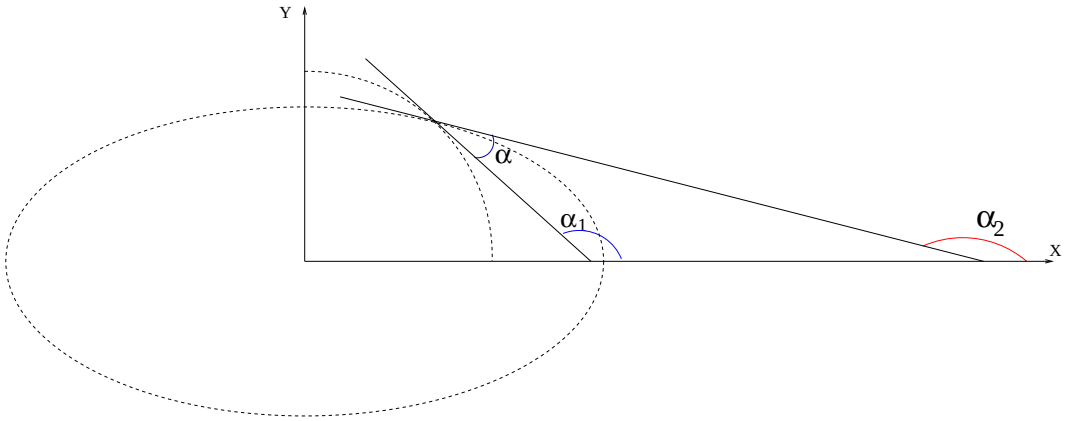


**Figure 5.5**: Closer look to the angles of interest of Fig. 5.3.

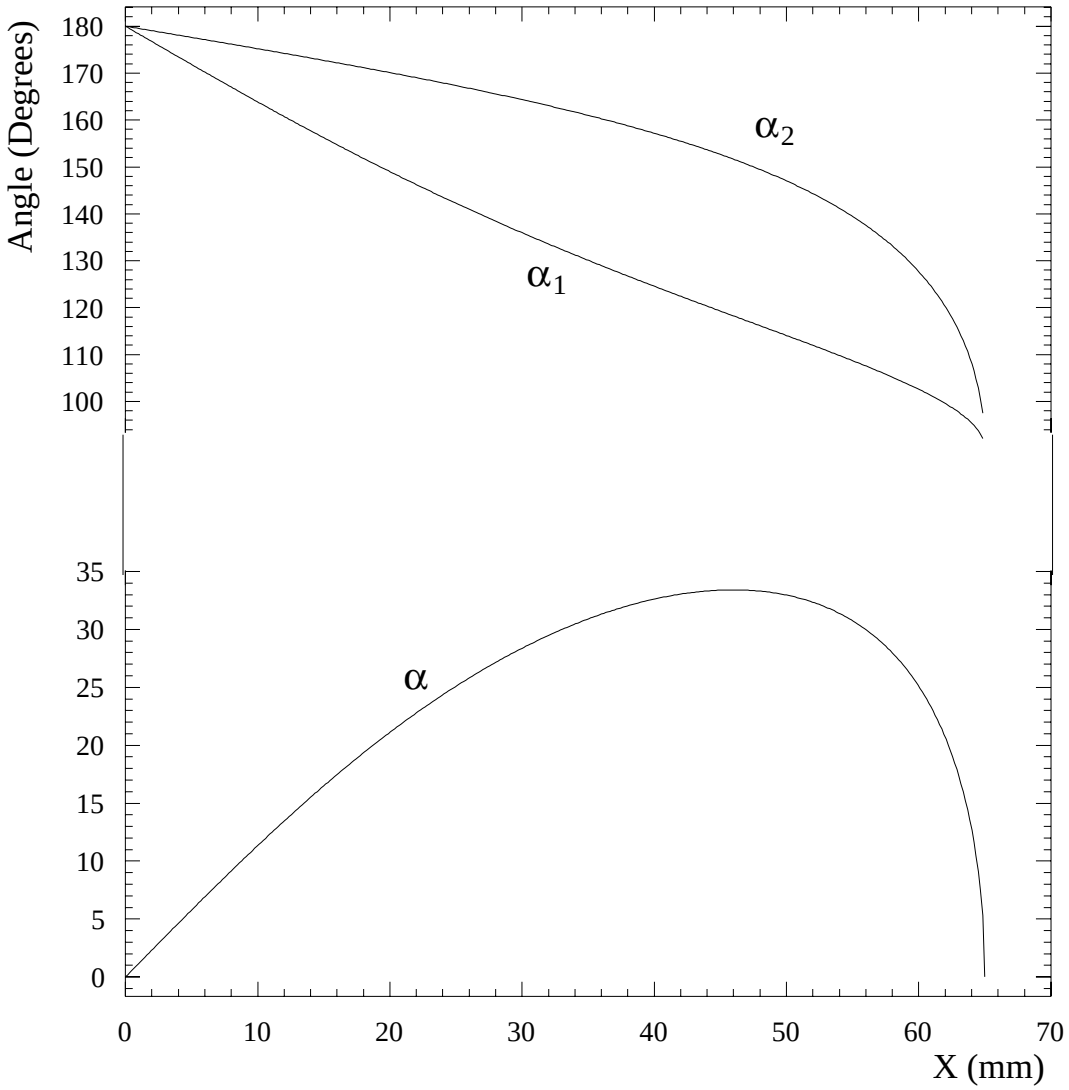


**Figure 5.6**: Angles variations as function of the position of the contact point between the mole wheels and the beam pipe wall.

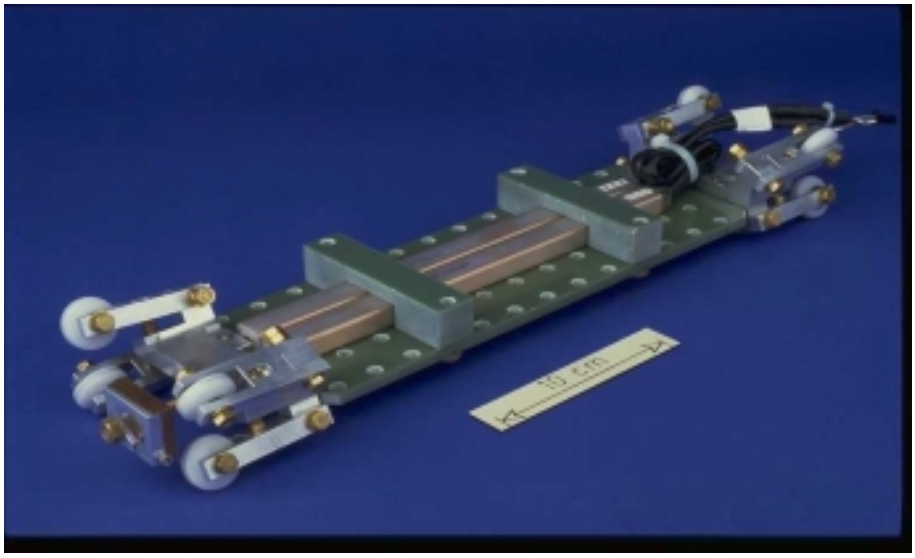

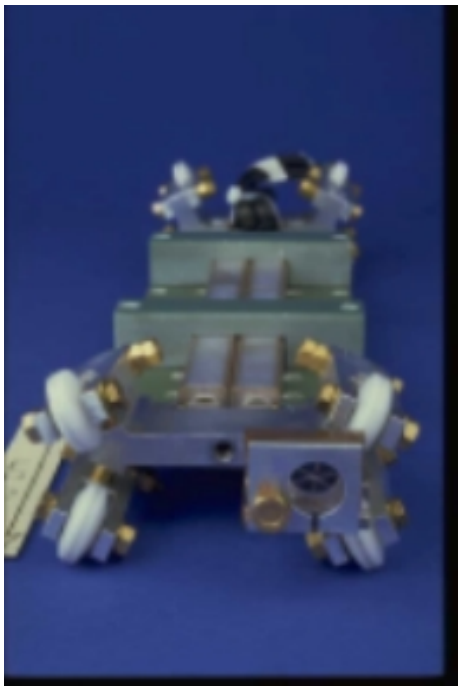

**Figure 5.7**: Pictures of the mapping mole.

### 5.1.2 Position Monitoring with an Interferometer

An accurate position monitoring is needed to evaluate the total integral field according to Eq. (5.1). For this purpose a laser source was adopted in order to perform a linear interferometer distance measurement. The diagram of the system is shown in Fig. 5.8.

The laser tube uses a helium-neon source which emits light with a well-known and stable wavelength($\lambda$ =632.8 nm). The beam is then passing through a magnetic field created inside the laser head to split the light into two frequencies ($F_1$ with right circular polarisation and $F_2$ with left circular polarisation) via the *Zeeman effect*. The difference between the two frequencies is about 2 MHz and the tube cavity is tuned in order to have equal intensity for the two components. The light beam is going through two plates which convert the polarisation of the two components from right and left circular to linear horizontal and vertical. At this point the beam has a diameter of 1 mm and goes trough a telescope collimator which expands it. An aperture at the output of the tube restricts the beam diameter to ≈7.6 mm.
A first beam splitter deviates about 20 % of the light to a reference detector. Within this detector another splitter is dividing the beam into two parts each of them containing both the frequencies. The *reference frequency* $F_1 - F_2$ is produced when $F_1$ and $F_2$ interfere. The outputs of the photodetectors have a frequency $F_1 - F_2 \approx 2\,MHz$; the DC component is used to send the *lock signal*[5], while the AC component is used to develop the *reference signal*.

The main light beam is transmitted to the interferometer, where a polarising beam splitter makes one frequency component ($F_2$) passing straight away and the other one ($F_1$) being deflected of 90 degrees. One of the two reflectors after the interferometer (see Fig. 5.8) is fixed and the beam is reflected with same frequency ($F_1$) which is used as reference. The other one is moving with a velocity *v* away from (or towards) the interferometer and the coming back beam has thus a Doppler

[5]This means that the instrument is ready to be read.

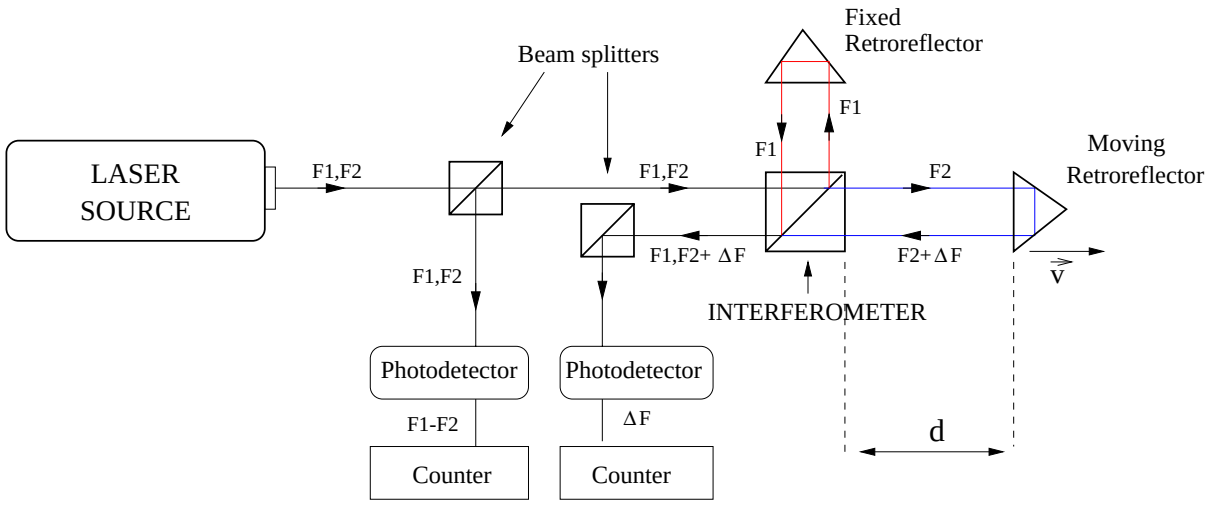


**Figure 5.8**: Laser interferometer diagram.

shifted frequency

$$F_2^I = F_2\left(1+\frac{v}{c}\right) = F_2 + F_2\frac{v}{c}. \tag{5.2}$$

The two light beams recombine again in the interferometer and go back to the main unit, where it is elaborated by a Doppler detector. Within it the signal is optically demodulated and sent to a photodetector whose output (*Doppler shifted signal*) has the frequency

$$\Delta F = F_1 - F_2^I = F_1 - F_2 - F_2\frac{v}{c} \tag{5.3}$$

The reference and Doppler shifted signals are converted into logical pulses and sent to two different counters. Each counter stores in a register the number of wavelengths, of frequency $F_1 - F_2$ and $\Delta F$ respectively. Analytically the signal processing is the following:

I. the reference detector determines the number of wavelengths of the signal with frequency $F_1 - F_2$ over a time period $\Delta t$:

$$\int_{\Delta t}(F_1 - F_2)dt = N_{F_1-F_2}^{\Delta t} \tag{5.4}$$

II. the second detector is processing the return beam of frequency $\Delta F = F_1 - F_2^I$, counting the number of wavelengths over the same period $\Delta t$:

$$\int_{\Delta t}\left(F_1 - F_2 - F_2\frac{v}{c}\right)dt = N_{F_1-F_2}^{\Delta t} - \frac{F_2}{c}\int_{\Delta t} v dt \tag{5.5}$$

III. the difference between the right-hand parts of Eq. (5.4) and Eq. (5.5) is computed as:

$$\Delta N = N_{F_1-F_2}^{\Delta t} - \left(N_{F_1-F_2}^{\Delta t} - \frac{F_2}{c}\int_{\Delta t} v dt\right) = \frac{F_2}{c}\int_{\Delta t} v dt \tag{5.6}$$

IV. the velocity can be expressed like *v=dL/dt* and Eq. (5.6) becomes:

$$\Delta N = \frac{F_2}{c}\int_{\Delta t}\frac{dL}{dt}dt = \frac{F_2}{c}\cdot L_{\Delta t} \tag{5.7}$$

The relative displacement of the retroreflector during the period $\Delta t$ is thus:

$$L_{\Delta t} = \frac{c}{F_2}\Delta N = \lambda_2^{vac}\Delta N \tag{5.8}$$

where $\Delta N$ is the the difference of the values stored in the two internal registers and $\lambda_2^{vac}$ is beam light wavelength in vacuum (section 5.1.3 will explain how to make the correction when the measurement is not in a vacuum environment).

### 5.1.3 Error Analysis

Unless the measurement is performed in vacuum the beam light wavelength has to be corrected for the index of refraction of air ($\lambda \rightarrow \lambda/n_{air}$). Such index is depending on the on the temperature, humidity and pressure of the environment where the measurement is performed. For example an increase in the air density (high pressure or low temperature) results in a lower light velocity and thus in a smaller laser beam light wavelength. Eq. (5.8) becomes:

$$L_{\Delta t} = \frac{\lambda_2^{vac}}{n_{air}} \Delta N \tag{5.9}$$

On the instrument adopted for this set of measurements the value of the index of refraction of air (which can be expressed also like $n_{air} = c/w = \lambda_{vac}/\lambda_{air}$, being *w* the velocity of light in air [24]) can be changed through a set of thumb-wheels located on the display unit.

The resolution of the instrument is 10 nm and the firm providing the laser source (HP) gives the following values for the accuracy [24]:

- $1\,\mathrm{ppm}/^{o}\mathrm{C}$
- $1\,\mathrm{ppm}/2.8\,\mathrm{mm\,Hg}$
- $1\,\mathrm{ppm}/90\,\%$ change in rel. humidity

Any lateral displacement of the retroreflector (or of the interferometer) with respect to the laser source introduces an error (called *cosine error*) due to the misalignment which causes the measured distance to be different from the actual one. The cosine error is the difference between the hypotenuse and the base of the triangle formed by the measured and the actual path. It can be identified when the the spot of the returning beam on the reflector is shifting laterally while the reflector is moving longitudinally. The relative error can be evaluated as:

$$E = \frac{s^2}{2d^2} \tag{5.10}$$

d = longitudinal displacement of the reflector;
s = lateral displacement of the returning beam spot.

A lateral displacement of the spot of 7.5 mm over 7.5 m of measurement (i.e. the length of the spectrometer magnet) gives a relative error of $5{\cdot}10^{-7}$ . This corresponds to the maximum cosine error in the length determination of the magnet, because the retroreflector mounted on the mapping mole has a diameter of 15 mm.

### 5.1.4 Digital Integrator

The search coil is directly connected to the inputs of the digital integrator. The voltage induced on the coil is first passing through a 10 Hz low pass filter, which is mounted at the input of the differential amplifier (Fig. 5.9).
For the subtraction of the amplifier output offset voltage an internal compensation of the operational amplifier and an additional subtraction circuit is used.
The internal compensation is varied with the front panel potentiometers and the subtraction circuit is supplied by an external source. The amplified coil signal is passed to the *voltage to frequency converter (VFC)* after subtraction of the offset voltage. The VFC has two pulse outputs, one with a frequency which is proportional to the voltage of the input signal ($f = c \cdot u(t)$) and a second which is constant ($f_{ref} = c \cdot U_{max}$). The two pulse trains are fed to a pair of 32 bit binary counters for one measurement period and switched to a second pair of counters for the following period. This method allows a continuous data taking.
At the end of each period the counts of cycles of the reference signal ($N_{ref}$) and the counts of cycles of the coil signal ($N_{sig}$) are subtracted each other,

$$N_{ref} - N_{sig} = N \tag{5.11}$$

$N_{ref}$ and $N_{sig}$ can be written as the integrals of the related frequencies,

$$N_{ref,sig} = \int \left(\frac{dN}{dt}\right)_{ref,sig} dt = \int f_{ref,sig} dt \tag{5.12}$$

and therefore N represent the integral of the signal voltage:

$$N = c\left(\int_{-\infty}^{+\infty} U_{max} dt - \int_{-\infty}^{+\infty} u(t) dt\right) \tag{5.13}$$

The subtraction of the integrated signal and maximum voltage ensures that the relative counts $\Delta N/N$ are independent of possible variation of the conversion factor *c*.
During normal operation the counters are switched and read every 200 ms, in phase with the signal of frequency 500 kHz which corresponds to the maximum voltage.
The instrument has a precision of $1 \cdot 10^{-4}$ of full scale. Four input ranges are available (tuning the gain of the input amplifier) and the resolution is thus changing from 0.3 $\mu$V to 20 $\mu$V. The gain maximum non linearity is $\pm 10^{-6}$ of the full scale, while the gain stability is $9 \cdot 10^{-6}$ of the full scale per $^oC$. In table 5.1.4 [25] the specifications of the noise and offset are summarised for the different gains selected.

**Table** 5.1: Digital integrator noise and offset specification

| Input Amp. gain | Input Range V | Offset $\mu V/^oC$ (max) | Noise $^\star$ $\mu$V (max) | Noise/Full Scale ppm |
|---|---|---|---|---|
| 1 | $\pm$ 5 | 10 | 10 | 2 |
| 4 | $\pm$ 1.25 | 3.5 | 2.5 | 2 |
| 16 | $\pm$ 0.3125 | 1 | 0.6 | 1.92 |
| 64 | $\pm$ 0.078125 | 0.4 | 0.3 | 3.84 |

$^\star$ Peak to peak, in the frequency range between 0.1 and 10 Hz.

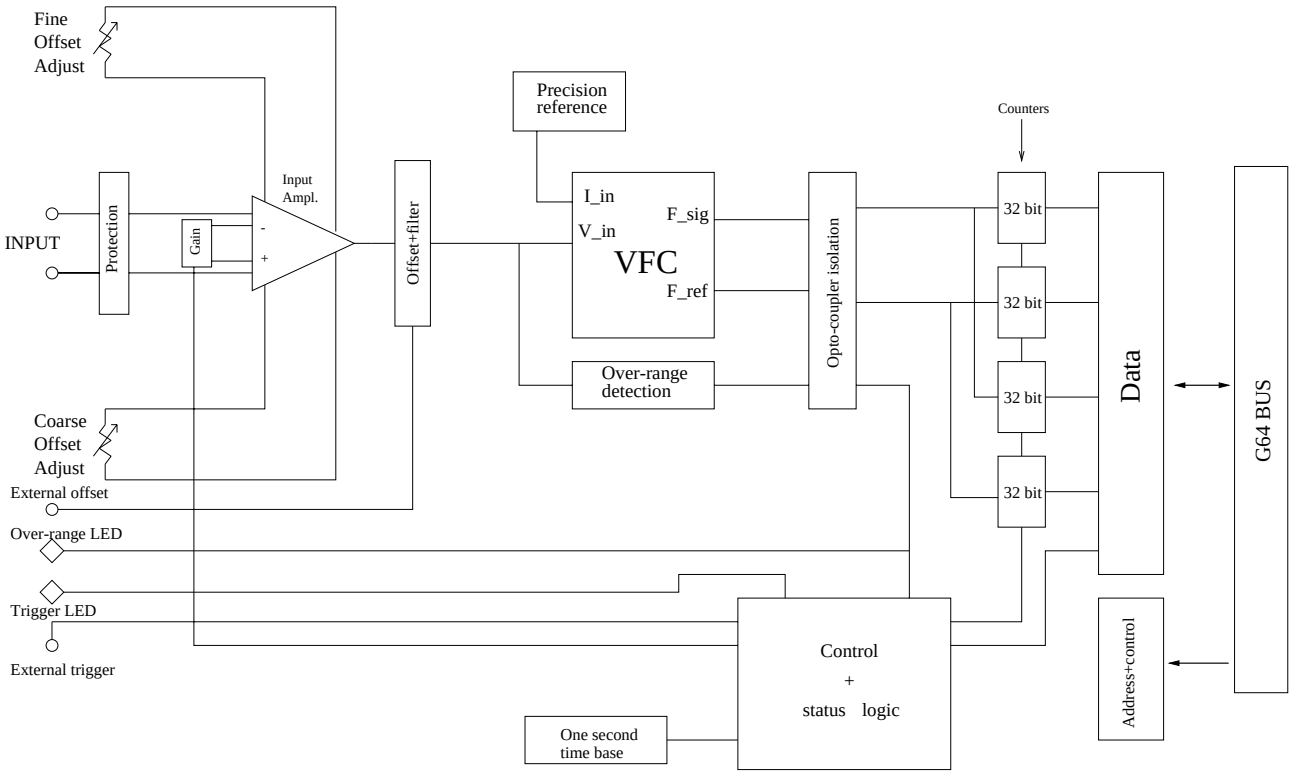


**Figure 5.9**: Block diagram of the digital integrator.

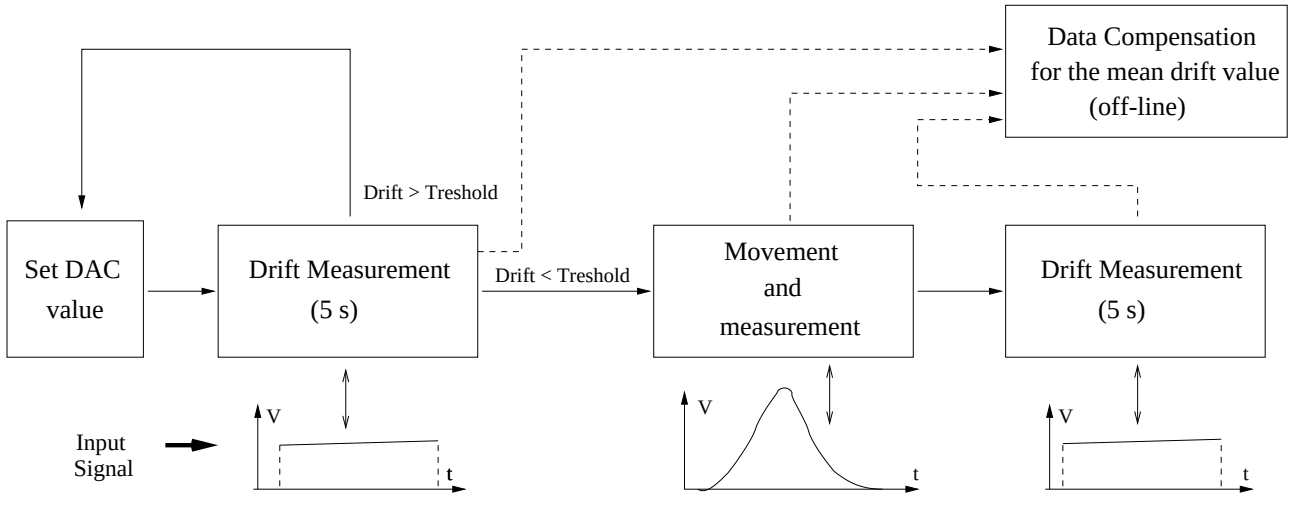


**Figure 5.10**: Diagram of the offset treatment procedure. The signal read by the integrator for each period are indicated.

The integrator was operated mainly with the maximum input amplifier gain, since the signal to be integrated was small. In Fig. 5.11 the induced voltage signal is shown as recorded by a digital scope during the movement of the coil for $\approx 40$ cm in the end-field region of the iron-concrete dipole placed in the laboratory, at a excitation current correspondent to a 100 GeV beam energy.
In Section 5.1.5 the particular cable conection to avoid additional induced voltages is described. During the mappings each step was 1 cm long; the maximum amplitude of the signal was the same

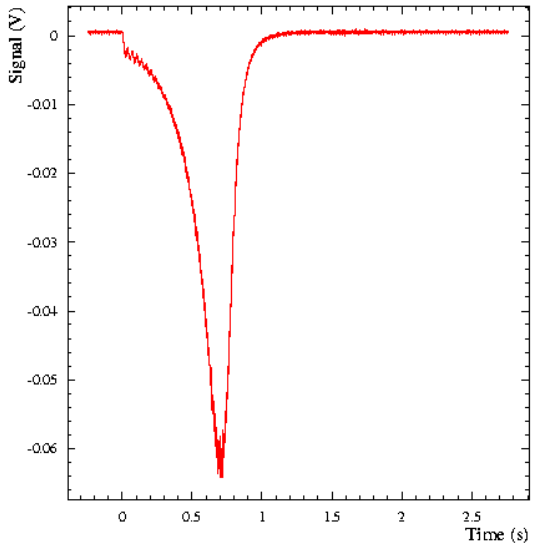


**Figure 5.11**: Voltage induced on the coil.

as for the 40 cm step[6], because $V = d\Phi/dt$.
The drift of the integrator was determined before and after each movement of the coil. The sources of the drift are the dependence of the amplifier offset on the temperature, as well as external sources like the stepping motor, the NMR teslameters, the magnet power converter.
To compensate for drift changes in time, the external offset voltage compensation input is connected to a *digital to analog converter (DAC)*. Repeated cycles were performed before each measurement, in order to move the coil only when drift of the integrator was small enough. The compensation procedure is shown in Fig. 5.10.

To be independent of the absolute accuracy of the integrator[7], a calibration of the system has been performed after every endfield measurement. The field inside the dipole gap (i.e. limit between "central field" and "fringe field") was infact precisly known, thanks to the NMR probes installed on the mole. The difference between this value and the "zero field" value[8] was set equal

[6]The signal amplitude depends on the maximum speed reached by the mole, but after some tests it was chosen for the mapping campaign to be the same as the one used while recording the signal in Fig. 5.11

[7]$\frac{\Delta \int u(t)dt}{\int U_{max}dt} = 1 \cdot 10^{-4}$ , see [25].

[8]The beam pipe extremities outside the magnet core have been shielded in order to lower the field down to a negligible value (see Chapter 3)

to the integral of the induced coil voltage, divided for the coil area:

$$B_{NMR} - B_0 = \Delta B = \frac{\int udt}{A} \tag{5.14}$$

this procedure overcomes all system drifts developing in a time longer than the measurement period (including, for example, possible variation of the coil area).
The instrument is microprocessor based and can be controlled from the front panel or remotely via the IEEE interface bus (GPIB). In the second case all the commands available on the front panel can be programmed. The measurement can be triggered by an external signal, by an internal one or by the GPIB proper command.

### 5.1.5 Cables

The electrical signals coming from the field monitors installed on the mole had to be continuously transferred to the electronics for the data acquisition. In designing the system two type of problems were present,

i. mechanical: the mole was moving forward and backward and the cables had to follow it, a push-pull system was needed;

ii. electrical: several signals had to be transferred at the same time avoiding cross-talk,

   a) the NMRs power supply;

   b) the NMRs RF signal;

   c) the NMRs resonance signal;

   d) the coil induced signal.

The signals a), b) and c) are normally transferred on individual wires along the standard NMR cable, together with other logical signals necessary for the the probe switching and auto-tuning.
The solution was found in using a flat cable with 25 parallel conductors in it. The tracking system has been designed in such a way that no additional elastic pulling or active pushing forces have been introduced, since the flat cable was just driven by the mole itself. Particular care was then put in the cable insulation in order to avoid influences on the magnetic field to be measured and in the single wires protection to prevent possible cross-talks.
Concerning the searching coil signal, the original configuration would have taken to an additional induced voltage due to the loop created by the two conductors. A test was performed putting a short circuit in place of the searching coil, keeping the mole motionless and ramping the magnet current between 0 and 4000 A. The result is presented in Fig. 5.12, where the induced signal, due to the cables loop only, is displayed. This effect was eliminated changing the cable connections, in order to have always two loops of equal dimensions and the induced current flowing in opposite directions. A diagram of the coil connection to the flat cable is shown in Fig. 5.13.

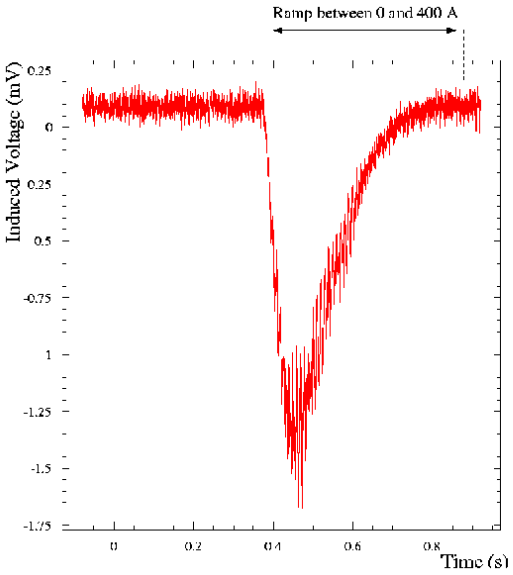


**Figure 5.12**: Induced voltage due to the cables loop in the original configuration.

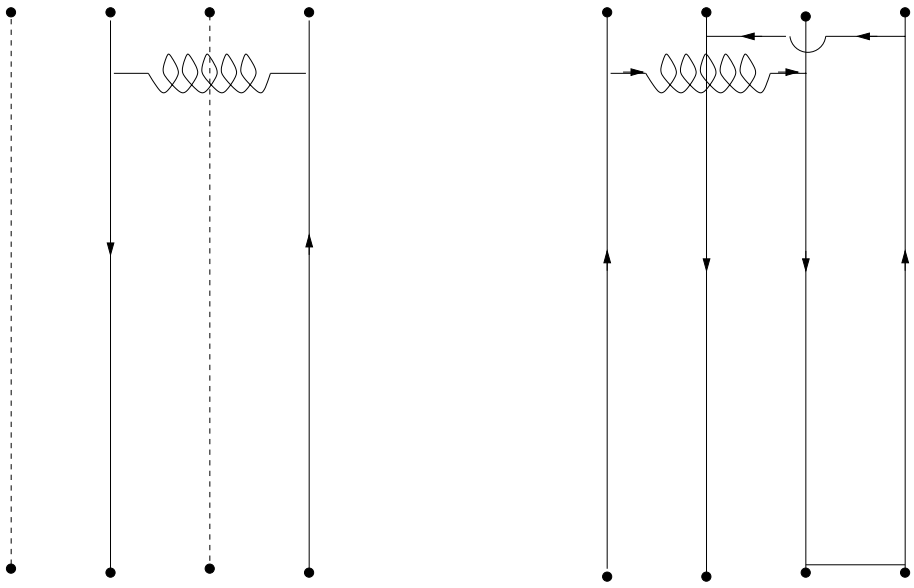

**Figure 5.13**: Original and compensated configuration of the coil connection on the flat cable.

## 5.2 Magnetic Field Monitors

The aim of a mapping is to evaluate the total integral magnetic field characteristic of a magnet, including the fringe regions where the field decreases to zero. In order to guarantee the zero-field conditions outside the magnet, the portions of vacuum chamber located around half a meter away from the magnet faces have been wrapped with a $\mu$-metal material used to screen the external electromagnetic fields.
The field in the dipole core is around two times the field in the iron-concrete LEP bending dipoles:

$$\begin{aligned} E_b = &\quad 22\,\text{GeV} \quad \Rightarrow B \approx 0.047\,\text{T} \\ E_b = &\quad 100\,\text{GeV} \quad \Rightarrow B \approx 0.222\,\text{T} \end{aligned}$$

### 5.2.1 Central Region and Reference Probes

The NMR probes adopted (Metrolab Probe Head 1072, Range Type 1 and Range Type 2) cover magnetic fields between 0.043 and 0.026 T. The resolution is $1{\cdot}10^{-7}$ T (or 1 Hz). The guaranteed accuracy is better than $\pm$5 ppm and the relative accuracy better than $\pm$0.1 ppm in uniform fields [3]. Three teslameters (Metrolab PT2025) and three multiplexers have been used, thus connecting the NMR probes on the three instruments according to the following configuration:

- fixed NMRs type 1;
- fixed NMRs type 2;
- movable NMRs (type 1).

The reference probes of the same range have been read via a multiplexer in order to avoid possible interference when two teslameters operates almost at the same frequency. For a detailed description of the theory behind the NMR probes see Section 4.2.

### 5.2.2 End Field Region

In order to cover the field range not detectable by the NMR probes a search coil has been installed on the mole. The coil was realized at CERN and is made of about one thousand turns around a rectangular frame (2.5$\times$ 1 cm).
The motion of the mole in the end field region, where the field gradient is high enough, induces a voltage between the coil terminals, being (for each step):

$$\Phi = \Delta B \cdot A \tag{5.15}$$

$$\Delta v = -\frac{d\Phi}{dt} \tag{5.16}$$

where $\Phi$ is the flux, $\Delta B$ the field change between two locations and A the coil area. An example of the signal detected during one step is shown in Fig. 5.11.

## 5.3 Stepping Motor

The adopted stepping motor is a standard available at CERN[9]. The motorized wheel has been chosen to fit with the toothed belt and the motor can be operated at 200 or 400 steps-per-turn.
The hardware includes the controller and a resolver read-out system. The available software has been adapted for the mapping mole operation in order to manage the variable parameters like the acceleration and the maximum velocity. The device has been ran via the OS-9 CPU used as interface for the whole automatic measurement procedure.

[9]Over 340 stepping motors are used in SPS and LEP only for beam instrumentation applications

# Chapter 6

# Measurements on a LEP Standard Bending Magnet

The first part of the mapping campaign with the travelling mole took part in a test facility where an iron-concrete magnet of the type MB[1] has been placed for previous experiments. In such environment it was possible to develop and calibrate the whole measuring system. The mentioned previous measurements on the same dipole magnet included a local mapping of the magnetic field along a portion of the iron-concrete core and it was thus possible to compare them with the mole measurements in the same portion.

## 6.1 Position Monitoring

In the first period of work the attention has been payed to the installation and test of the position monitoring with the laser interferometer and to studies on the possible mapping procedures and reliability, at the beginning concentrating on the core region monitoring with the NMR probes installed on the mole. The laser source has been placed on a heavy cubic mortar block in order to keep it in a very stable position. After the installation of the retroreflector (see Section 5.1.2) on the travelling mole, the laser beam has been aligned with the chariot trajectory, in order to keep the signal locked all along the mapping distance.
Due to the high accuracy required on the determination of the integral field $\int Bdl$ , the accuracy of the position monitoring is fundamental. The intrinsic accuracy and resolution are described in Section 5.1.2. The reliability of the system has been checked immediately after the setup of the test bench, performing several reproducibility measurements. The plots in Fig. 6.1 illustrate the result of these tests. The graphs show the absolute reading differences (values as function of the position and distribution) in millimeters between two consecutive scans of the magnet length, with opposite direction of movement of the mole. This gives an idea of how precisely the mole is stopping in the same positions to sample the magnetic field. The mean value of such difference is of the order of $4\,\mu$m $\pm$ $47\,\mu$m which gives a value of $\approx 4 \cdot 10^{-3}$ relative to the used step size (10 mm). This is an evaluation of the mechanical reproducibility of the system: how precisely the chariot is going where the operator wants in spite of all the possible events which can perturb the mole behavior, like instabilities in the stepping motor, inelastic stresses on the toothed belt, etc.
For the energy calibration aims this does not represent a measurement uncertainty. Given that the

[1]The common bending magnets used in the LEP arc sections.

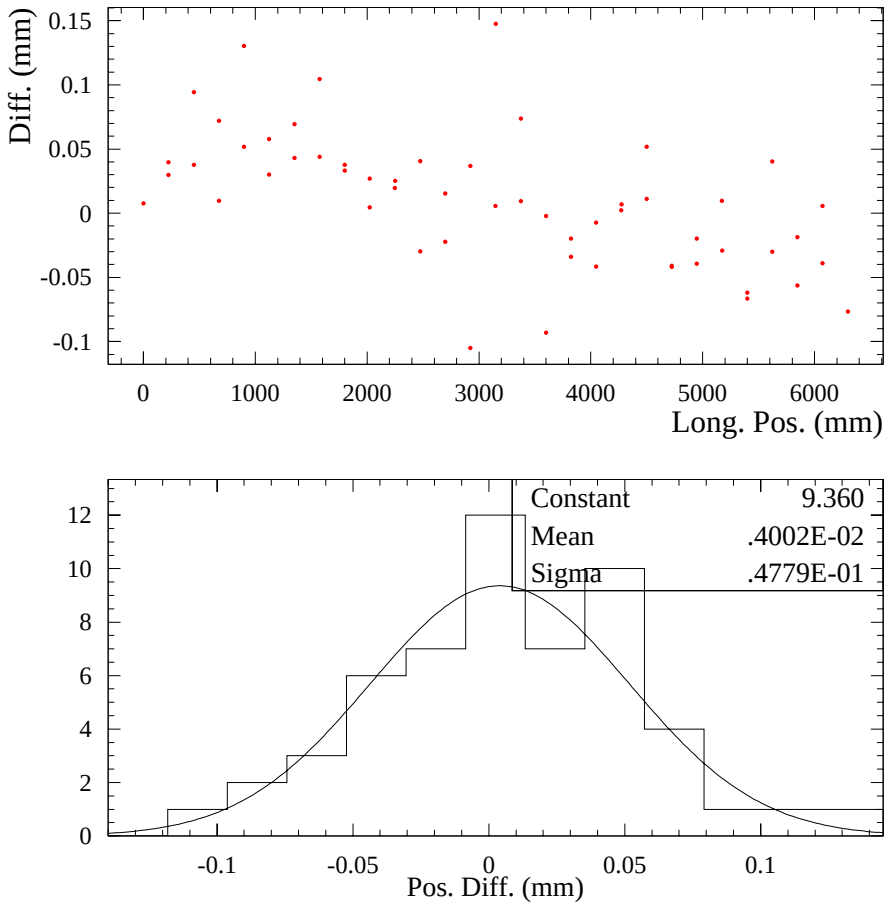


**Figure 6.1**: Test on the position reproducibility.

mapping is taken between two zero-field levels at the extremities of the dipole, the field integral is in fact not influenced by the absolute locations in which the B-field is sampled. For each portion of measurement the integral field is determined by two local B-field times the distance between the two locations. Above it has been demonstrated that the determination of such distance with the laser interferometer is good enough to give an accurate evaluation of the total integral.
At this stage of the measurements an interesting phenomenon was observed. In monitoring the mole position without moving it, a small displacement was detected after the ramp of the magnet excitation current. In Fig. 6.2 the displacement is shown to be of few microns. A few investigations showed that such phenomenon is due to the thermal lengthening (shortening) of the beam pipe in which the mole is placed. After the ramp of the current the temperature is quickly increasing. The dedicated temperature regulation system is then cooling down the magnet, with some oscillations in the first period. After some time the conditions are stabilized, the temperature is smoothly increasing and the beam pipe slightly changing its length in one direction. This is a demonstration of the very high resolution and reliability of the laser interferometer setup. It is worth underlining again how displacements like the one just described does not affect the accuracy on the integral magnetic field, because the magnet core and the laser interferometer do not move, only the vacuum chamber is sliding inside the gap. The important is measuring the B-field in a well-known location, whatever it is.

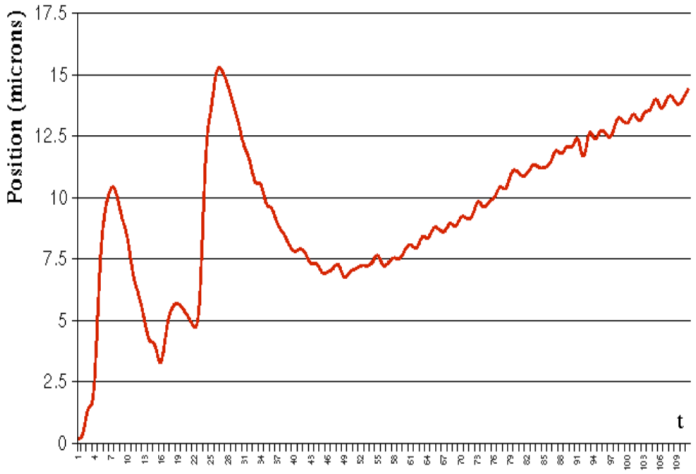


**Figure 6.2**: Measurement of the mole displacement due to thermal gradients of the beam pipe.

## 6.2 Magnetic Field Mapping in the Core Region

The mapping of the magnetic field started with some test measurements in the dipole core, in order to check the setup stability and choose the best mapping procedure. The proper operation of the NMR probes placed on the travelling mole was verified. The first maps were taken keeping the magnet equipped with some flat plates used in previous measurements, placed in three locations in-between the beam pipe and the lower pole face. Such plates are present also in some of the LEP bending dipoles[2] in order to make the magnetic field uniform enough to let the NMR probes (installed there) work properly. At this stage also some *air gap sensors* were mounted along the magnet and their metallic parts were also affecting the field shape.
Comparing Fig. 6.3 and Fig. 6.4 the effect of all these magnetic materials is illustrated. The field is made uniform enough for the probes locking and its magnitude is locally changed. The two plots refer to two different magnet excitation currents, nevertheless the difference in the relative change of the B-field is evident ($\pm 9 \cdot 10^{-3}$ before and $\pm 1 \cdot 10^{-3}$ after the removal of the plates).
During the previous measurements [7] the longitudinal profile of the magnetic field was determined over a length of 3 m. in a portion of its length. A first check of the mole measuring system consisted in comparing such measurements with the new ones at the same locations of the core. The results are shown in Fig. 6.5, in which the two field profiles are superimposed. The correlation between the two is very good. Both measurements show the structure of the magnetic field along the longitudinal coordinate of the beam trajectory. Such structure is due to the different iron packages used in the core production, which identify six different "regions". Three of them were already evident in the previous measurements. The maximal relative discrepancy is $5 \cdot 10^{-4}$ which can be regarded as very good, taking into account the simple test setup of the previous measurements and above all the possible changes in the relative field profile after several degaussing cycles of the magnet core and the possible differences of the environmental conditions.

[2]Typically in the injection region iron magnets.

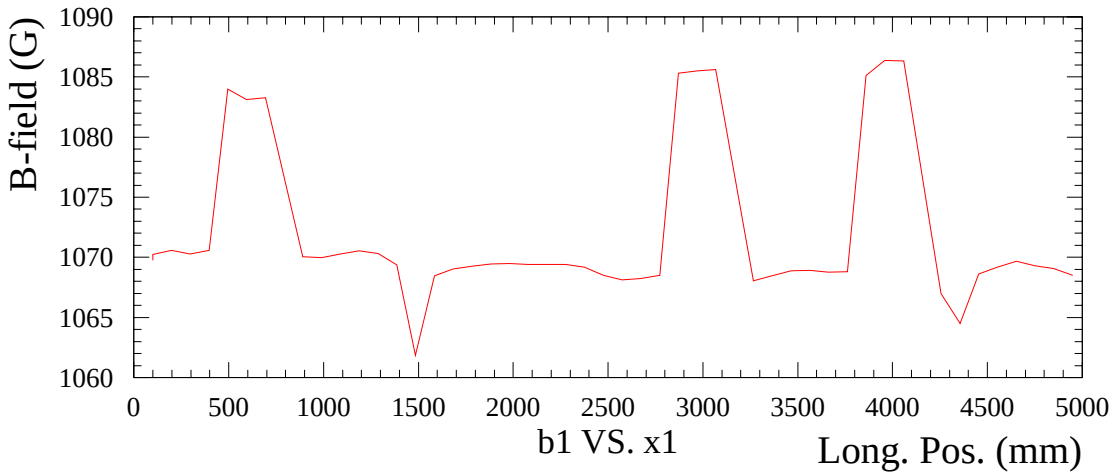


**Figure 6.3**: B-field profile of the iron-concrete magnet, before removing the field plates and the air-gap sensors.

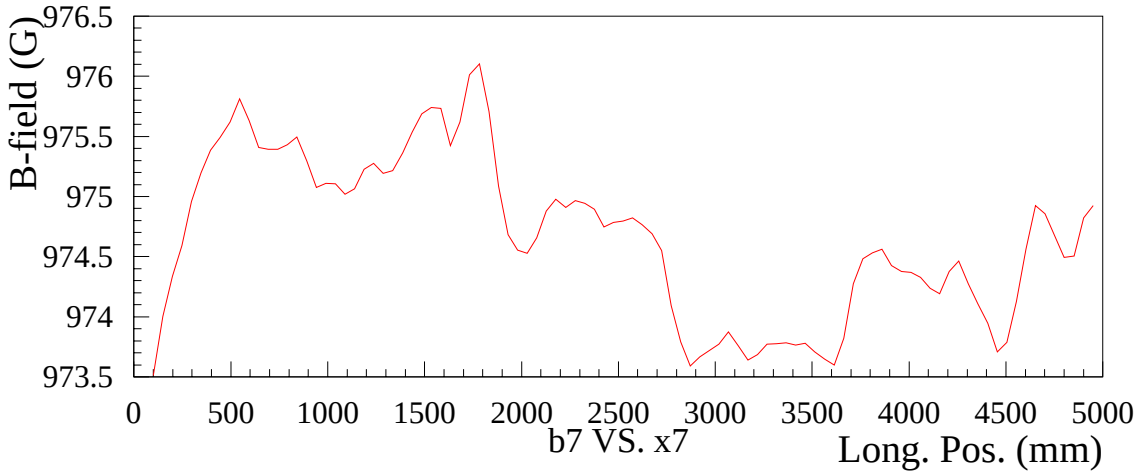


**Figure 6.4**: B-field profile of the iron-concrete magnet, after removing the field plates and the air-gap sensors.

**Measurements reliability** Further test measurements were made in order to demonstrate the dependence of the accuracy on external factors or on the procedure itself.

I. *Temperature dependence.* A number of temperature probes were installed in different locations of the magnet core and coil. Neither local nor mean temperatures revealed evident influence on the integral field values, mainly because such temperatures were kept within small ranges thanks to the dedicated temperature regulation system.

II. *Step size and interpolation*. The integral field is calculated like an approximated sum

$$\int Bdl \approx \sum_{i=1}^{N} B_i \cdot \delta x_i \tag{6.1}$$

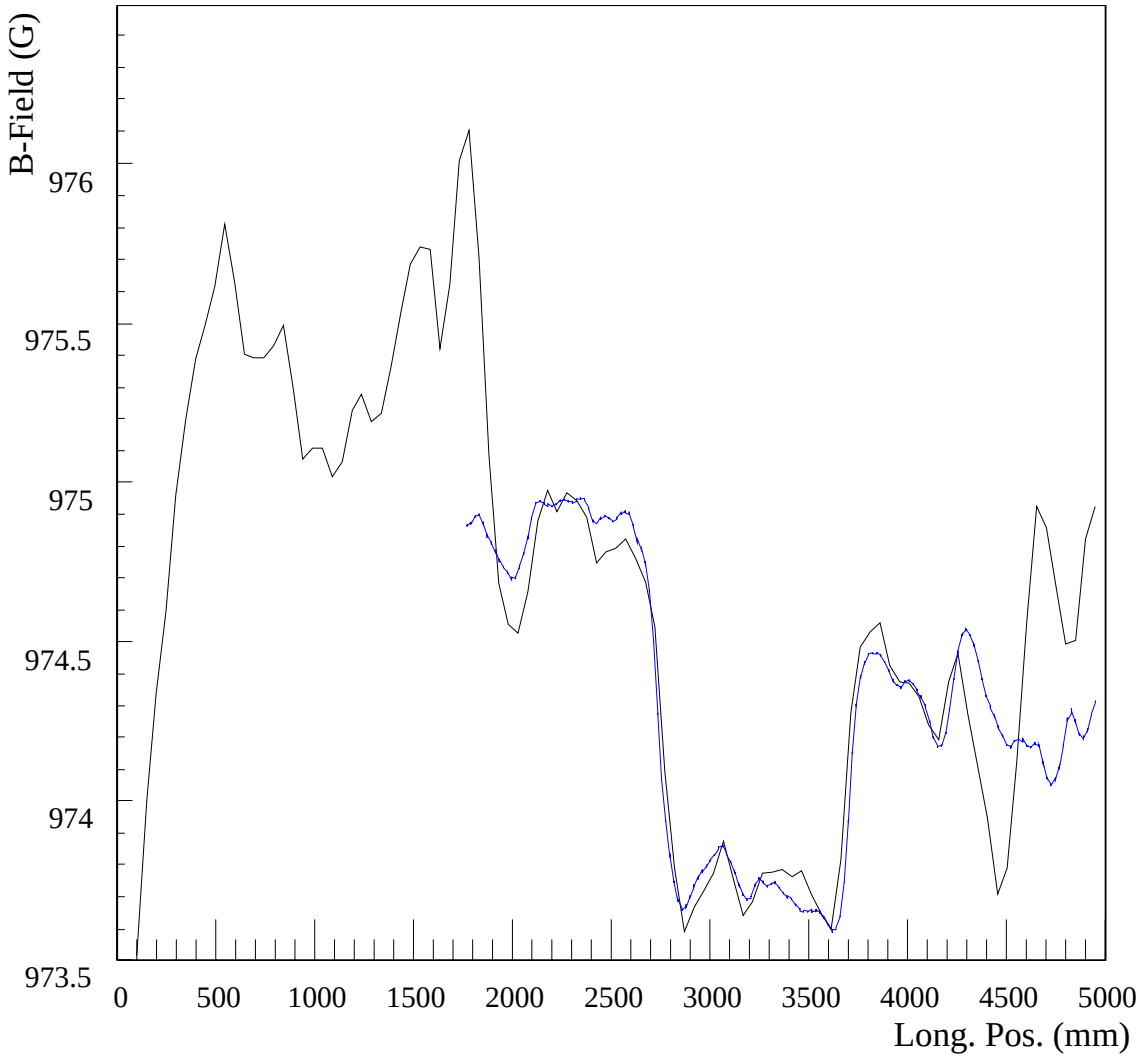


**Figure 6.5**: Longitudinal B-field profiles of the iron-concrete magnet. The previous year measurement extends from 1800 mm to 5000 mm.

This means approximating, for each step, the field integral with the sum of the areas of a triangle and a rectangle Fig. 6.6, by doing a linear interpolation between two consecutive map points. The larger the step size, the larger the difference between the field integral and

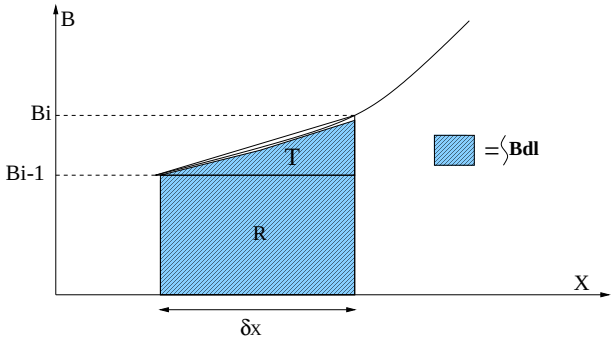


**Figure 6.6**: Integral field calculation by linear interpolation

the sum. Some maps of the central core region using two different step sizes (10 mm and 20 mm) showed a relative difference in the integrals very small, of the order of less than $4 \cdot 10^{-6}$ (see also Section 7.1). The larger step size was thus chosen, in order to reduce the mapping time.

III. *Consecutive maps reproducibility.* A series of maps was then performed to verify the reproducibility on the field integral calculation during consecutive scans with the same conditions. The results of sixteen consecutive maps of the core region are shown in Fig. 6.7. The tendency to increase is likely due to small changes of the magnet core temperature, but the reproducibility of the results is very good, being one division on the plot equal to a relative change of $5 \cdot 10^{-6}$ .

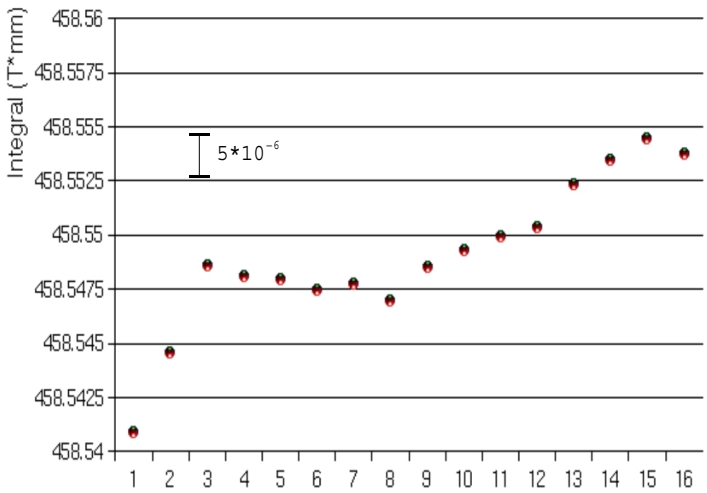


**Figure 6.7**: Calculation of the core region field integral during sixteen consecutive maps.

## 6.3 Fringe Field Mapping

In this section the method implemented to measure the end-field is described. In a region of about forty centimeters, going from the edges of the dipole towards the outside of the magnet, the magnetic field is decreasing from the value corresponding to the nominal energy to what can be assumed as a "zero field" [3] , according to the value monitored by a *Flux Gate* instrument. This kind of instrument has an accuracy of few tenth of mG , but the correspondent error is negligible in terms of the integral field. It was decided to use a *search coil*, since the mole movement of a certain step is enough to have a magnetic flux varying with time when the the mole is running from outside (i.e. zero-field) to inside (i.e. nominal energy) the magnet and in the opposite direction.

The basics of such type of measurement are described in Section 4.1. The measurement consists in integrating the signal induced on the coil, which can be expressed folowing Eq. (4.2), that is equal to

$$\Phi = S \cdot \Delta B \tag{6.2}$$

In this way the integral calculation in the end field region is performed, as for the core region, approximating it with a sum, having, after the integration in time of the voltage signal, the field sampled in a number of points along the longitudinal coordinate.

**Coil calibration**

An example of the signal induced on the coil while moving in the region close to the magnet extremities is shown in Fig. 5.11. The value of the coil equivalent surface was evaluated ramping the magnet between two levels detectable with high accuracy by mean of the NMR probes and integrating the signal induced during the ramp. This experiment was done several times, keeping the mole (i.e. the coil) in a fixed position inside the magnet core. The outcome of this kind of calibration is shown in Fig. 6.8.

**Test inside the magnet**

The accuracy of the search coil was checked moving the mole in the magnet core where the NMRs probes are available as a precise field monitor and comparing their readings with the coil field estimation. After forty steps covering eighty centimeters, the maximum difference between the coil and the NMR measurements resulted to be of the order of 100 mG with a field of 1000 G. Assuming this level of uncertainty for each step in the end field region, the relative error estimate on the fringe field results to be

$$\frac{\Delta \int Bdl}{\int bdl} \approx 1 \div 2 \cdot 10^{-4} \tag{6.3}$$

which is acceptable, weighing this part of measurement only one tenth of the total field integral estimation.

[3] See Section 3.2.1, which explains how this condition was reached by mean of a $\mu$-metal shielding.

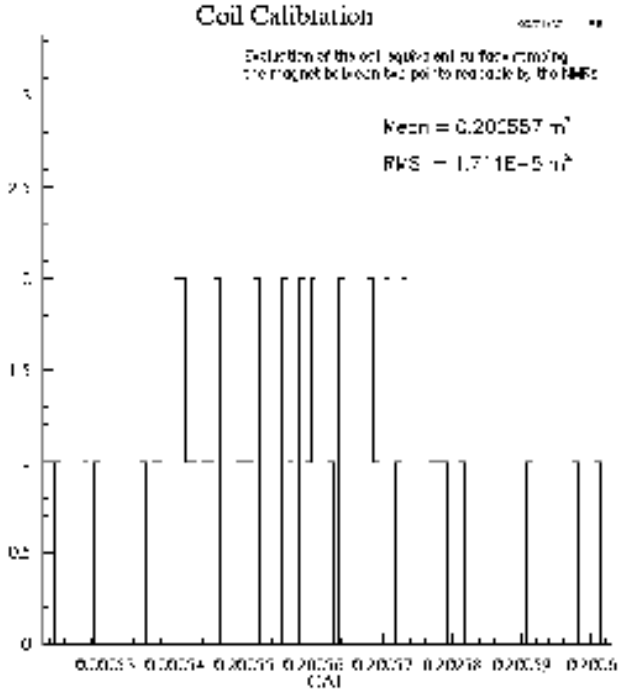


**Figure 6.8**: Calibration of the coil equivalent surface.

**Test outside the magnet**

Like for the sampling frequency of the core magnetic field with the NMR probes, the step size of the search coil movement in the end field region had to be decided. The larger the step size, the larger the amplitude of the induced signal (which is then less sensible to noise), but the larger the error due to the approximation by the linear interpolation.

In order to optimize such quantity, some tests were made moving the mole from outside to inside the magnet core using different step sizes (see Fig. 6.9).
Increasing the sampling frequency the calculated integral should converge to the real one. The convergence was demonstrated to be sufficient adopting a step size of $10$ mm which also corresponds to the coil dimension along the direction of movement.

A further improvement in the resolution of the system consisted in taking each time two maps of the end field region, with the same step size but with the starting point shifted of $5$ mm, half of the step size.

**Setup of the measurement procedure**

Few details about the mapping procedure have been already analyzed, like the choice of the field sampling frequency. During the period spent on the iron-concrete magnet, it was possible developing in detail such procedures. In particular attention was payed in producing an efficient software and optimize the hardware, with the following aims:

i) reduce the average map-time without compromising the accuracy;

ii) reduce as much as possible the possible noise sources;

iii) eliminate all the hardware components with magnetic properties which could have affected the measurements.

At this point, the mapping procedure was defined by a single computer program which was able to manage all the measurements automatically, starting from the magnet ramping to the mole proper movement, the field detection and the data storage. The steps are the following and will be explained in the next chapter:

– magnet conditioning (see Section 7.2.1);

– ramp of the dipole excitation current to the nominal energy level;

– start of the mapping with the two scans of the fringe region with shifted starting point;

– map of the core region with the NMR probes;

– same procedure in the opposite direction.

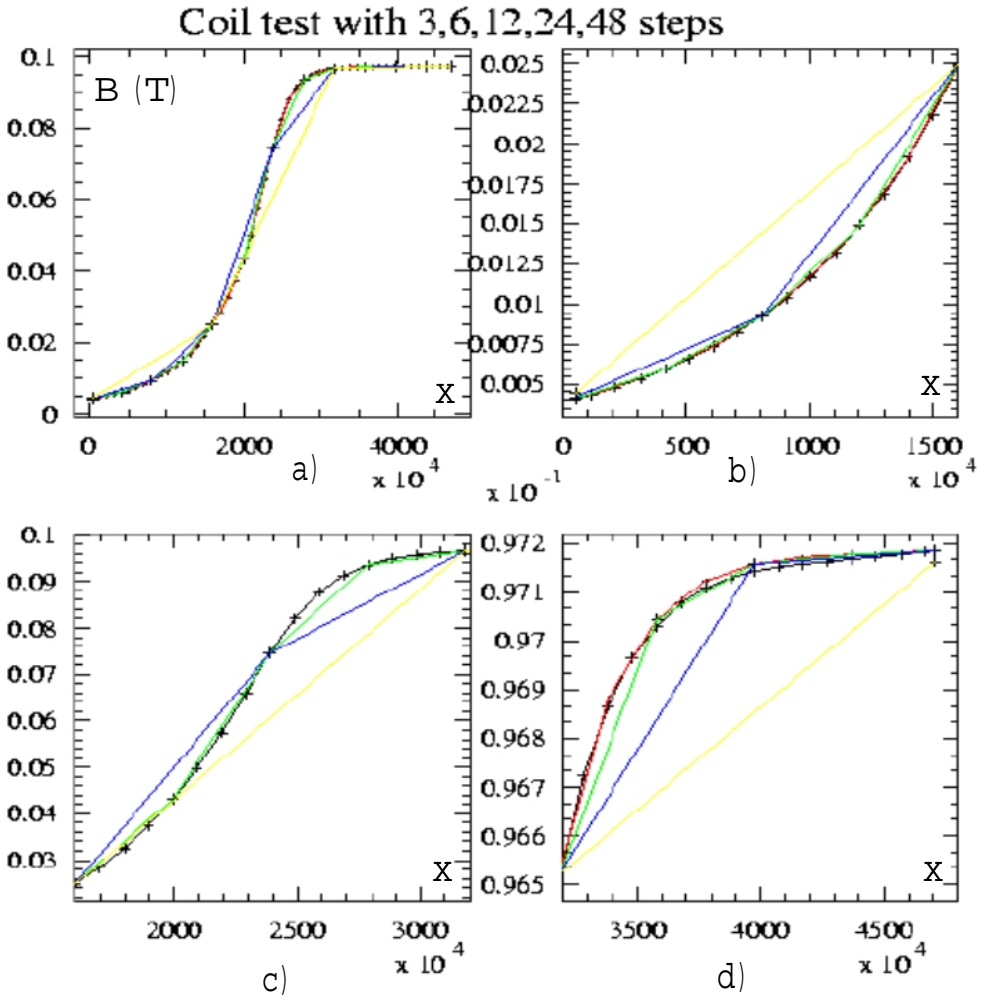


**Figure 6.9**: Test on the end field region sampling frequency. a) shows the field profile. b), c) and d) are zooms on the zones of most interest, where the field profile has a change in its slope and the approximation with linear interpolation is critic.

# Chapter 7

# Measurements on the Spectrometer Magnet

This chapter covers the application of the measurement system to the mapping of the dipole magnet adopted for the LEP spectrometer.
As described above, the dipole was measured in the laboratory by a system based on a movable carbon arm sliding inside the dipole gap (see Section 3.2.3). The aim of this second part of the mapping campaign was

- to cross check the measurements performed with the first method;
- to produce a set of reference measurements to be compared with the foreseen re-mapping of the magnet after the transportation in the LEP tunnel.

Considering the three set of measurements (movable arm in the laboratory, mapping mole in the laboratory, mapping mole in the LEP tunnel) the main possible reasons for different results were:

i. the vacuum chamber insertion after the first measurements in the laboratory;
ii. the transportation of the magnet from the laboratory into the tunnel;
iii. different power supply for the magnet after the installation in LEP ;
iv. changes in the environmental conditions, mainly between the ground level and the underground measurements.

The test bench used in the laboratory for the previous mapping was partially dismounted and a vacuum chamber was inserted in the yoke, to allow the mounting of all the hardware necessary for the mole movement and control.
A certain delay compared to the schedule and some final tests on the end field measurements, reduced the available time in the laboratory to few days.
Therefore it was decided to scan only two LEP energies, 44 GeV and 100 GeV, to have a reference at both low and high energy working points, and then foresee a larger scan in the tunnel measurements.
The main topics of the chapter will be a description of the practical differences between the iron-concrete and the full-iron core dipoles, an overview of the measurements in the laboratory and in the LEP tunnel followed by a comparison between the two and a cross-check with the results from the previously executed maps.

## 7.1 Recover of the Setup used for the Standard LEP Bending Dipole

**Reference Probes**

After some weeks of tests on the iron-concrete magnet, the equipment was moved to the spectrometer dipole. The measurement system was almost the same as before.
The main difference was the presence of the four fixed probes, to monitor continuously the magnet excitation during the mapping. It was decided to use two Teslameters and two multiplexers following the scheme of Fig. 7.1.
In previous tests an interference between the NMR probes was noticed when reading them at

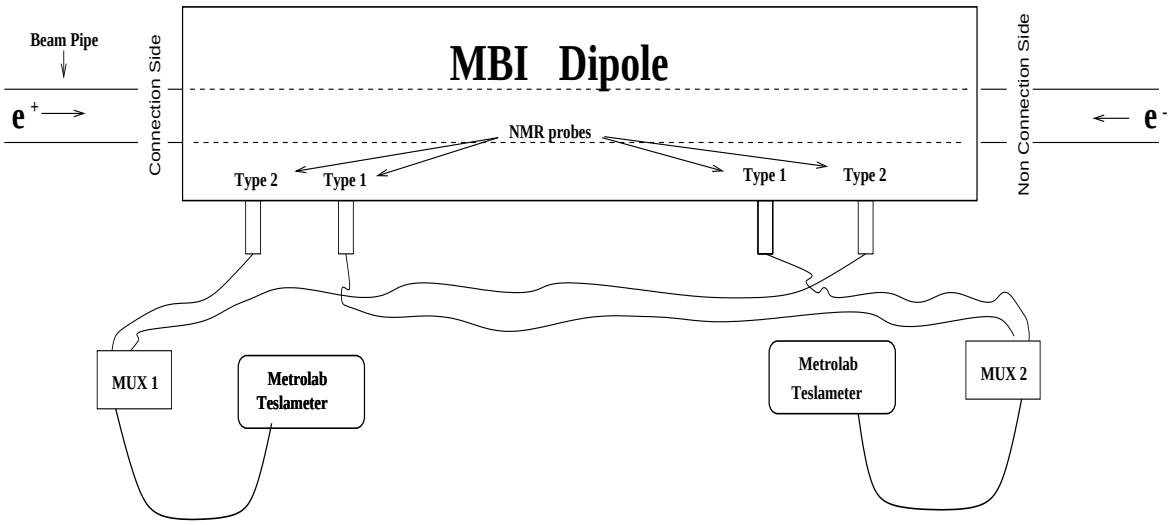


**Figure 7.1**: Layout of the reference NMR probes connection: probes of identical type are connected to the same Teslameter via a multiplexer.

the same time and at an almost equal field. If the local fields are almost identical the spin excitation frequencies are tuned to almost identical values. In such a case a strong cross-talk was observed. To reduce this effect as much as possible probes of identical type were connected to one Teslameter using a multiplexer. The NMR probes placed on the same side of the magnet are connected to different instruments. Depending on the probes type, a certain NMR frequency corresponds to two different magnetic fields, which means that for the same field, type 1 and type 2 probes are locked on two different frequencies. It is thus enough using a multiplexer [1] on the same type probes to avoid having similar frequencies locked at the same time.
The probes were read out every twenty seconds. The software has been optimized in order to address and preset them properly.
These considerations are important also for the spectrometer run, since the positioning of the probes is the same as the one studied for the mapping. The electrical connection chosen in the LEP tunnel consists of only one Teslameter with one multiplexer, since fast sampling is not actually necessary and every additional electronic device needs space and shielding against radiation.

[1] While one channel of the MUX is connected all the other probes' cables are disconnected, the power supply, the NMR signal, the modulating wave for the auto tuning.

Before inserting the vacuum chamber in the gap of the magnet the four reference probes already used for the “carbon arm” measurements were taken away from their supports, in order to avoid possible damages during the pipe installation.
The vacuum chamber is lifted up by 2 mm and thus not centered vertically in the yoke in order to host the probes properly with enough place on the lower pole of the magnet and so avoid mechanical stress. The center of the gap, where the ideal beam orbit is passing, is thus not in the center of the vacuum pipe. For this reason a 2 mm thick plate was inserted between the wheel supports and the central plate of the mole, to come back to a centered mapping position. After the chamber insertion, the four NMR probes were put back in the original position with an accuracy of 0.5 mm (see Section 3.3). This represents a focal point, in order to have a consistent comparison with the previous measurements.

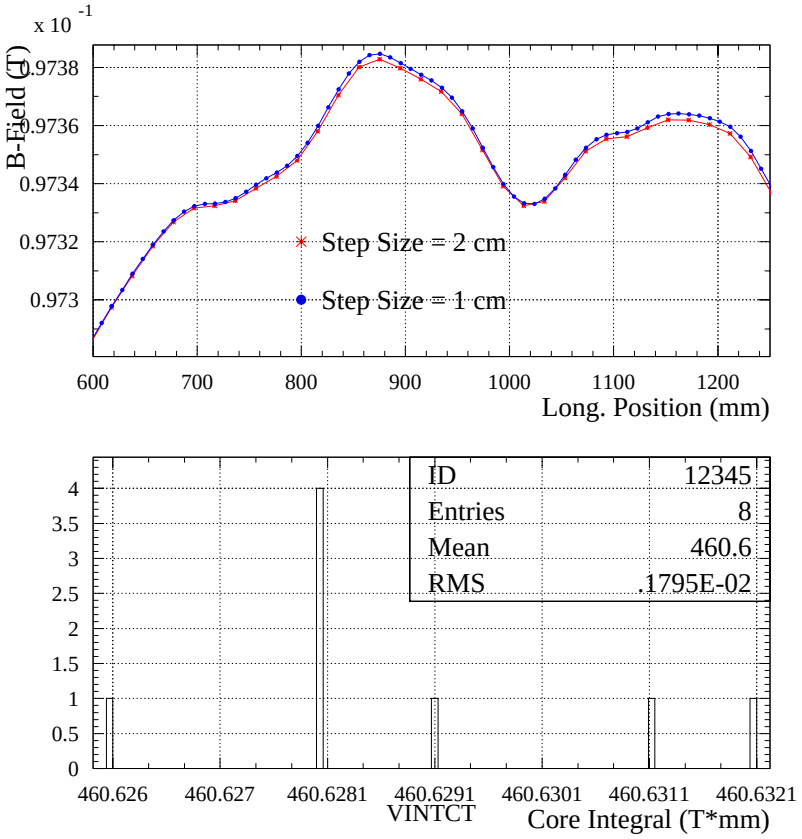


**Figure 7.2**: Comparison of the two step sizes for the core mapping (top) and distribution of the core integral for a set of maps with both step sizes (bottom)

**Fringe Field and Mapping Time**

On the MB magnet, due to limited physical space, only a part ($\approx 40$ cm) of one side end field was monitored. Obviously that was not the case on the MBI magnet, where the mapping was starting and ending in the so called "zero-field" regions[2].
Having a longitudinally longer distance to map, the time required for every map increased. Foreseeing this, which would have been a problem in terms of available statistics, a test was previously performed in the core of the MB dipole, to check whether worsening the resolution in the NMR-monitored region by increasing the step size from 1 cm to 2 cm, would have compromised the accuracy of the measurement.
In Fig. 7.2 there is a zoom of two maps with different step size superimposed and a distribution of the core integrals for eight consecutive maps; the first two (in time) have a 2 cm as step size, while the last six have 1 cm.
The outcome is that no difference is visible, since the RMS on the integrals distribution is of the order of $4 \cdot 10^{-6}$ .
Such analysis lead to the conclusion that the mapping time could be reduced by almost a factor two, since measuring the core field with the NMR probes takes the main part of the total time. In fact, for every step, a switching between the two multiplexer channels is required, each time waiting for the NMR lock.

[2]The zero-field is provided by the $\mu$-metal material, see Section 3.2.1.

## 7.2 Measurements in the Laboratory

The first measurements were performed on the ground level in the former ISR tunnel which was chosen as an ideal location in terms of environmental conditions (temperature stability, humidity, electrical noise etc. . . ).
The mapping procedure was based on the same philosophy as the one used on the MB dipole:

- Forward direction:
  - double end field map of the non-connection side with two shifted starting positions;
  - core map with the two NMR probes;
  - double end field map of the connection side with two shifted ending positions.
- Symmetric procedure for the backward direction.

The nominal conditions of the magnet were established according to Table 7.1.

| ENERGY $[GeV]$ | CURRENT $[A]$ | B-FIELD $[T]$ |
|---|---|---|
| 22 | 105.40 | 0.0476 |
| 41.6 | 199.36 | 0.0900 |
| 44 | 210.99 | 0.0952 |
| 50 | 239.61 | 0.1082 |
| 55 | 263.58 | 0.1190 |
| 60 | 287.54 | 0.1298 |
| 70 | 335.46 | 0.1514 |
| 80 | 383.38 | 0.1731 |
| 90 | 431.31 | 0.1947 |
| 95 | 455.27 | 0.2055 |
| 100 | 480.21 | 0.2167 |
| 103 | 493.61 | 0.2228 |

**Table** 7.1: Nominal Energy - MBI Current correlation

### 7.2.1 Magnet Conditioning

Before every ramp a *degaussing cycle*[3] was performed and once the nominal energy for the map was reached, a cycle of *bending modulation* was done. Both procedures, plus the ramp to the nominal energy were following the standard LEP operation:

- Degaussing Cycle
  $0$ A $\longrightarrow 500$ A $\longrightarrow 0$ A for five times at a ramp speed of $50$ A/s.
- Ramp
  $0$ A $\longrightarrow I_{nominal}$ at a ramp speed of $2.3$ A/s
- Bending Modulation
  $I_{nominal} \longrightarrow I_{nominal} + 3 \cdot 10^{-4} \longrightarrow I_{nominal}$ for 7 times at a ramp speed of $2.3$ A/s

The bending modulation consists of a conditioning cycle, applied to improve the stability of the actual working point [26]. After such repeated excitation, in case of a variation in the power supply or any change in the excitation current, the magnetic field has a significant smaller jump (Fig. 7.3). In fact it happens that after the first small increase of the current during the bending modulation, the magnetic field increases by a relative amount of the order of $5 \cdot 10^{-5}$ , much less for the following cycles and reaches a saturation after the seventh cycle, see [1] Chapter 7. The phenomenon is shown in Fig. 7.3.

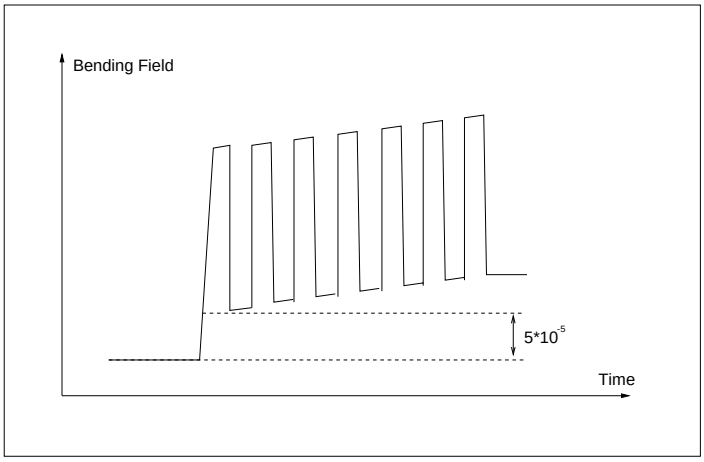


**Figure 7.3**: Bending modulation cycles

### 7.2.2 Reference NMRs Reading

During the measurements, the field was constantly monitored by the four fixed NMR probes. A typical trend of the B-field at the location of the Type 2 probes is shown in Fig. 7.4. For the same time period the field is decreasing in one location whereas it is constant in the other. The local minima and maxima are due to ferromagnetic materials present in the electronics of the probes

[3]Cycle of the coil current in order to make the B-field follow its characteristic hysteresis curve. The outcome is a reduction of the residual magnetic field.

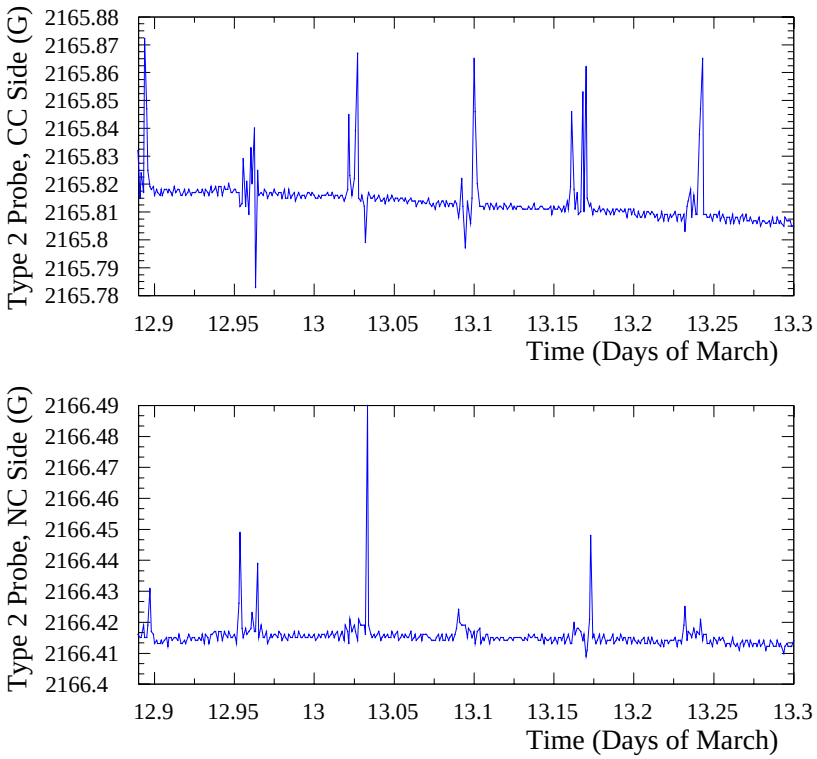


**Figure 7.4**: Behaviour of the two Type 2 Reference Probes during five maps at 100 GeV. The peaks are correlated to the beating between the fixed and moving probes when the mole is passing close to the reference probe.

installed on the mole. When the mole passed by the longitudinal coordinate of a fixed probe[4], the reference value was changing of a maximum $\delta B/B \approx 2.3 \cdot 10^{-5}$ . Such values are considered as unusable and not taken for the integral field normalisation. The histogram of Fig. 7.5 takes into account 3500 "acceptable" NMR readings at 100 GeV.The mean difference is thus[5]

$$B_{NMRref2-NC} - B_{NMRref2-CC} = 6.039 \cdot 10^{-1} \pm 1.21 \cdot 10^{-4} \ G$$

This corresponds to a difference which is of the order of $2.8 \cdot 10^{-4}$ relative to the absolute value of the field. In fact

$$\frac{B_{NMRref2-NC} - B_{NMRref2-CC}}{B} = \frac{6.039 \cdot 10^{-1} \ G}{2165 \, G} = 2.78 \cdot 10^{-4}$$

At an excitation current which corresponds to a beam energy of 44 GeV all the four field monitors are available, see Fig. 7.6. The mean difference (relative) between the two Type 2 probes is $\approx 3.1 \cdot 10^{-4}$ , see Fig. 7.7. During these maps, corresponding to a beam energy of 44 GeV and 100 GeV, the reference probes were not displaced.
Nevertheless the difference in the readings, relative to each other, is explainable with the non linearity behaviour of the dipole fields at different excitation currents. In different locations the

[4] In particular when the head of one probe is less than ten centimeters from the body of the other (see Section 4.2.5.)

[5] The error on the mean is obtained by taking the RMS of the distribution and dividing it by the square root of points considered.

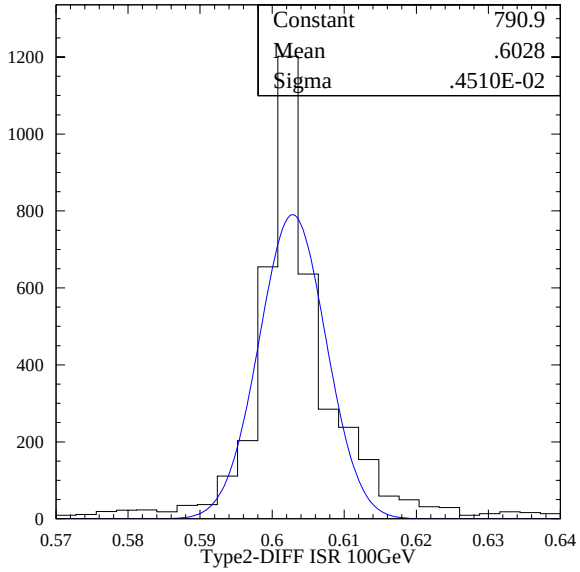


**Figure 7.5**: Difference in the B-field at the two Type 2 NMR locations, 100 GeV.

| | $E = 44\,GeV$ | $E = 100\,GeV$ |
|---|---|---|
| $\frac{Ref2_{CC} - Ref2_{NC}}{<B_{field}>}$ | $-3.10 \cdot 10^{-4}$ | $-2.78 \cdot 10^{-4}$ |
| $\frac{Ref2_{CC} - Ref1_{NC}}{<B_{field}>}$ | $2.31 \cdot 10^{-4}$ | – |
| $\frac{Ref2_{CC} - Ref2_{NC}}{<B_{field}>}$ | $1.84 \cdot 10^{-4}$ | – |

**Table** 7.2: Reference NMRs in the laboratory measurements.

field increase during a ramp is never the same, they have unequal *gains*.
This is actually the reason why one cannot solely trust local point field measurements and requires a calibration from which the integral field can be calculated as a function of the fixed probes. A similar analysis can be done for the Type 1 probes, of course only at 44 GeV, where they still lock. It is worth resuming in a table the conclusions from the reference NMR probes in the laboratory measurements (see Table 7.2), in order to compare further on their status with the one in the LEP tunnel.

### 7.2.3 Fringe Field Measurements

A searching coil was used for the determination of the end-field integral. During the movement of the mole the inducted voltage was integrated by a voltage to frequency converter (see Section 5.1). To optimize the setup the following parameters were adjusted:

a. the stepping motor acceleration and top velocity;

b. the gain of the input voltage amplifier of the integrator;

c. the setting of the voltage to frequency converter;

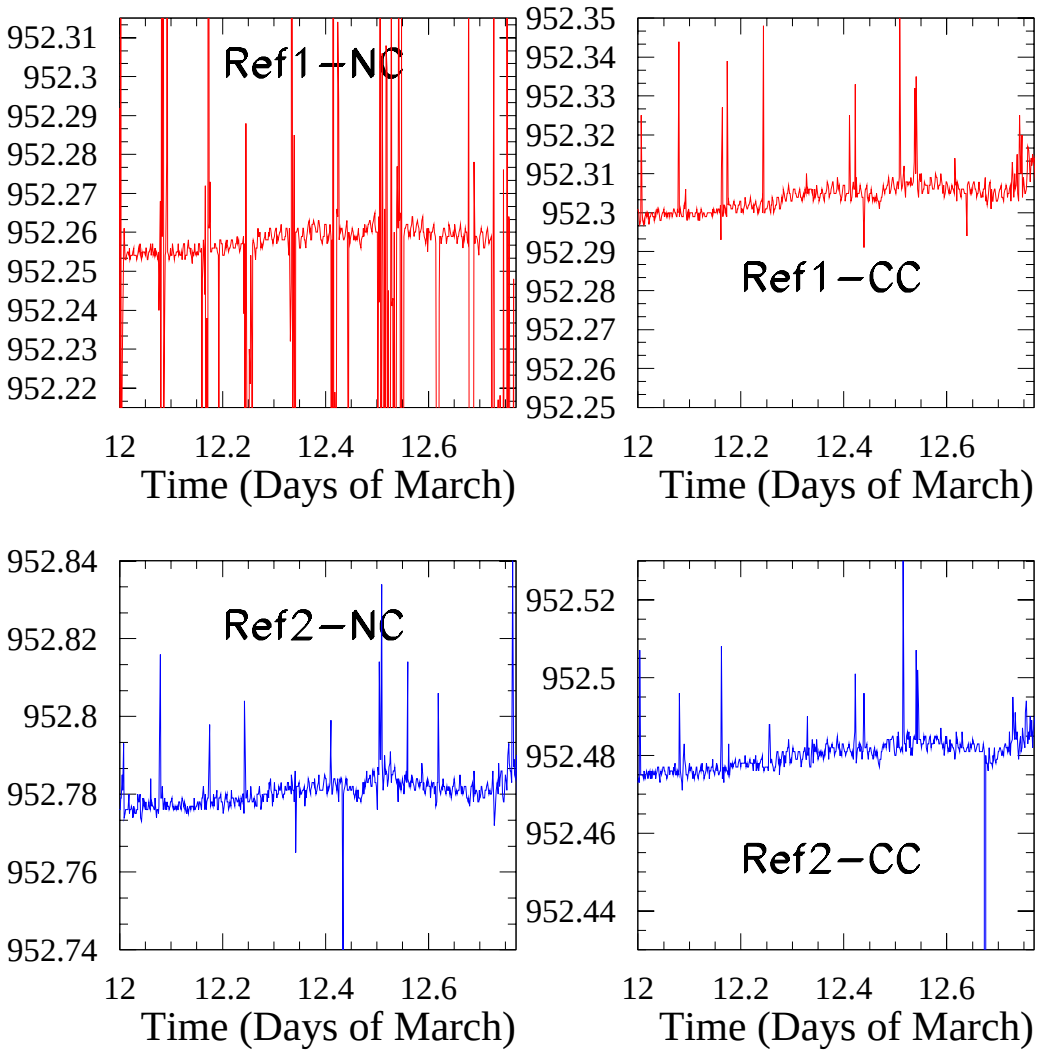


**Figure 7.6**: Trend of the four fixed probes during the maps at 44 GeV. The Type 1 probe on the non-connection side locks in a less effectively way then the others.

d. the integrator analog drift compensation;

e. the integrator digital drift compensation.

The acceleration/deceleration of the coil measurement setup was linearly influencing the voltage on the coil. To reach a high signal to noise ratio the speed change must be maximal. A high acceleration caused a non reproducibility of the mole positions at the nominal steps locations, which could have caused a decrease in the field measurements reproducibility. An intermediate value for this parameter was thus chosen.
Concerning the DAC cycle (see Fig. 5.10), the analog drift compensation was done by measuring the drift before every measuring cycle and changing the input offset voltage of the integrator amplifier as often as needed to be below a threshold. The threshold was set to half the maximum value of the less significant digit and opportunely changed when the gain of the input amplifier was changed. The threshold value resulted in a drift contribution, which was negligible compared

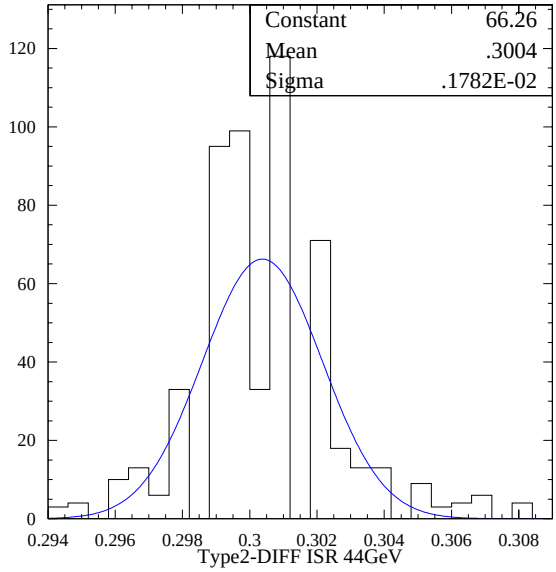


**Figure 7.7**: Difference in the B-field at the two Type 2 NMR locations, 44 GeV.

with the total value of the integrated voltage.
In any case the drift level after each step was monitored and recorded for five seconds. The outcome was, in general, an increase in the drift, so this last value was taken for the signal correction. In Table 7.3 an example of data acquisition for some steps is showed. The threshold for the DAC iteration was set to $5 \cdot 10^{-7}$ V, in fact the numbers in the third column are all below this value. The fourth column nevertheless reveals how the drift systematically rose again after the coil movement.
In Fig. 7.8 the profile of one of the two end fields is displayed for a map at 100 GeV. The following

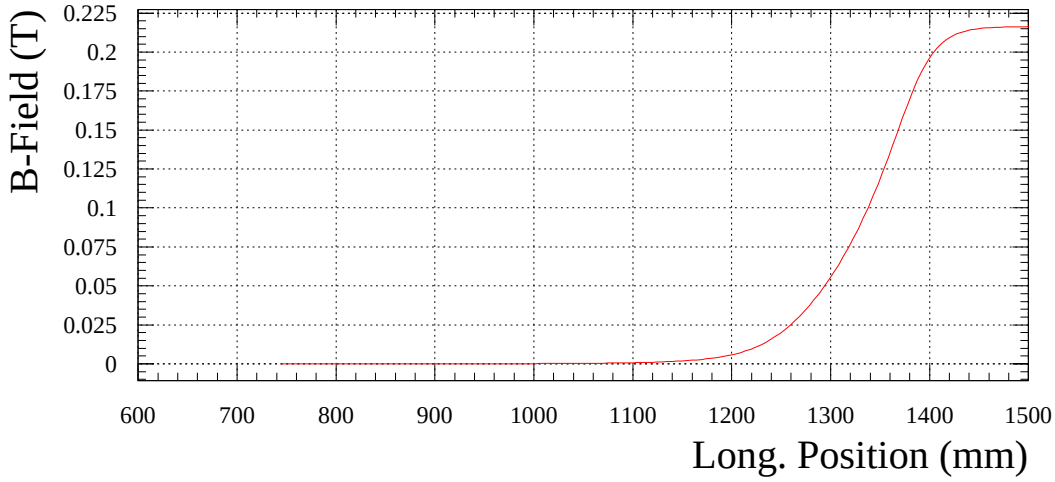


**Figure 7.8**: End field shape in the non-connection side of the magnet.

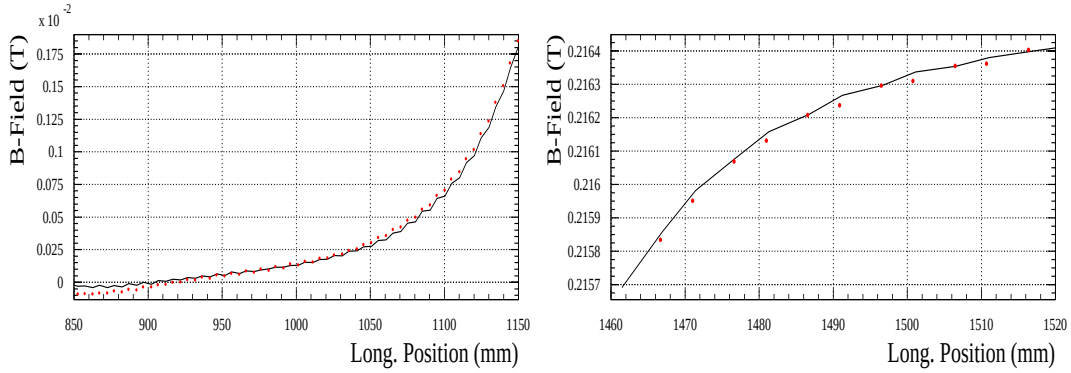


**Figure 7.9**: Zoom of the end field for two different maps, one plotted with a dotted line, the other with a continuous line.

plots (Fig. 7.9) show the overlapping of two typical end field maps, zoomed in the zero-field region and in the last zone measured by the coil before starting using the NMRs.

| Motor Resolver | Integrated Signal $[V \cdot s]$ | Drift after the DAC cycle $[V]$ | Drift after the movement $[V]$ | Initial Position $[mm \cdot 10^5\ ]$ | Final Position $[mm \cdot 10^5\ ]$ |
|---|---|---|---|---|---|
| ... | ... | ... | ... | ... | ... |
| 5474 | 0.0001485 | 0.0000004 | -0.0000010 | 107977064.0 | 108969504.0 |
| 5497 | 0.0001912 | 0.0000004 | 0.0000004 | 108969472.0 | 109957856.0 |
| 5521 | 0.0002505 | 0.0000001 | 0.0000001 | 109957904.0 | 110949008.0 |
| 5543 | 0.0003237 | 0.0000001 | -0.0000005 | 110948928.0 | 111935072.0 |
| 5566 | 0.0004215 | -0.0000004 | -0.0000004 | 111935048.0 | 112926560.0 |
| 5588 | 0.0005379 | 0.0000004 | -0.0000005 | 112926528.0 | 113912976.0 |
| 5611 | 0.0006846 | 0.0000004 | 0.0000004 | 113912976.0 | 114908616.0 |
| 5633 | 0.0008426 | 0.0000002 | 0.0000002 | 114908616.0 | 115897216.0 |
| 5655 | 0.0010228 | 0.0000002 | 0.0000002 | 115897232.0 | 116887528.0 |
| 5676 | 0.0012060 | 0.0000001 | -0.0000006 | 116887568.0 | 117876392.0 |
| 5698 | 0.0014027 | 0.0000001 | -0.0000013 | 117876448.0 | 118870160.0 |
| 5720 | 0.0015800 | 0.0000002 | 0.0000008 | 118870264.0 | 119855448.0 |
| 5741 | 0.0017901 | 0.0000001 | 0.0000001 | 119855488.0 | 120849856.0 |
| 5764 | 0.0019837 | 0.0000000 | 0.0000009 | 120849888.0 | 121839536.0 |
| 5786 | 0.0022223 | 0.0000001 | -0.0000011 | 121839536.0 | 122836328.0 |
| 5809 | 0.0024536 | -0.0000001 | -0.0000001 | 122836320.0 | 123825696.0 |
| 5832 | 0.0027356 | 0.0000000 | 0.0000004 | 123825696.0 | 124816392.0 |
| 5856 | 0.0030329 | -0.0000001 | -0.0000004 | 124816352.0 | 125804672.0 |
| ... | ... | ... | ... | ... | ... |

**Table** 7.3: Example of raw data from the end field map

### 7.2.4 Total Mapping Results

**Measurements at 100 GeV**

The central region of the magnet was monitored with the intrinsic accuracy of the NMR probes. It should be noted that due to time problems, it was decided to carry out most of the maps by reading only one of the two movable NMR probes, thereby saving time by not switching on the multiplexer.
At each energy some "reference" maps were performed with both probes working. Such tests gave a proof of the reproducibility in the two probes readings and of their ratio at each longitudinal location. Along the magnet the values read from one probe can thus be predicted by the ones of the other.
It was therefore possible every time to calculate the integral field along the ideal orbit in the center of the dipole gap, at the same time having two transversally off-centered maps.
An example of thirteen core integrals are displayed in Fig. 7.10 for the same number of maps. During these measurements the temperature was particularly stable. The RMS on the core integrals

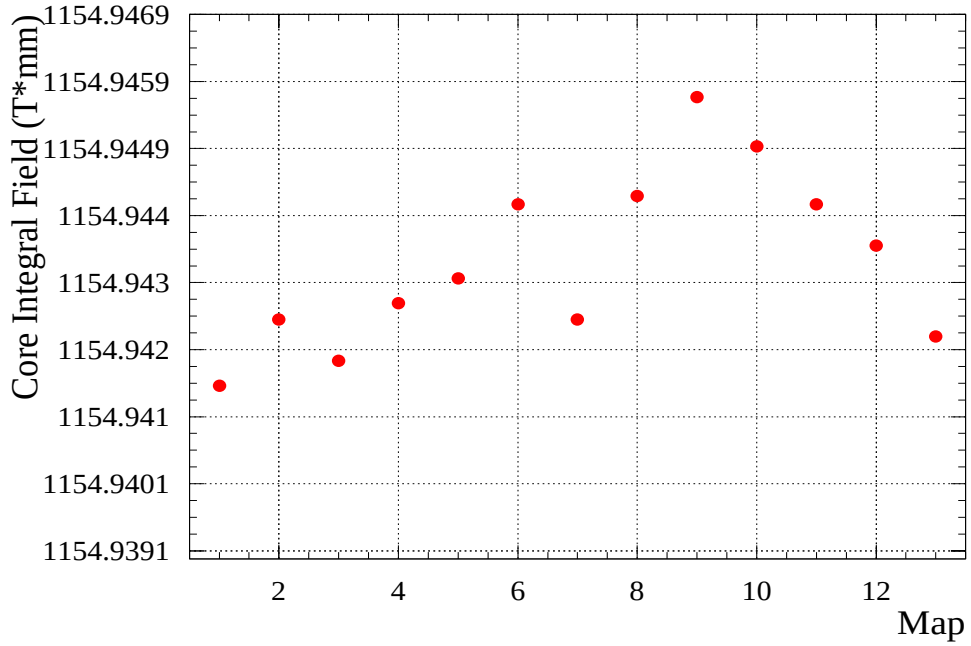


**Figure 7.10**: Core integrals at 100 GeV, laboratory.

is $0.1250 \cdot 10^{-2}$ T·mm which corresponds to a deviation of $\approx 1.08 \cdot 10^{-6}$ relative to the mean integral value. This result is not surprising, but represents the intrinsic accuracy of the NMR probes, when working in ideal conditions.
Analysing the *total* integrals, the reproducibility is reduced by a factor ten, see Fig. 7.11, but is still within the aims of the mapping, the RMS being $0.1988 \cdot 10^{-1}$ T·mm, $\approx 1.77 \cdot 10^{-5}$ relative to the absolute value of the integral. The second energy studied was 44 GeV, for which a set of eight maps was performed. They were realized during the same day, but with a degaussing cycle in between two of them. Again the temperature conditions were stable and a very high reproducibility was

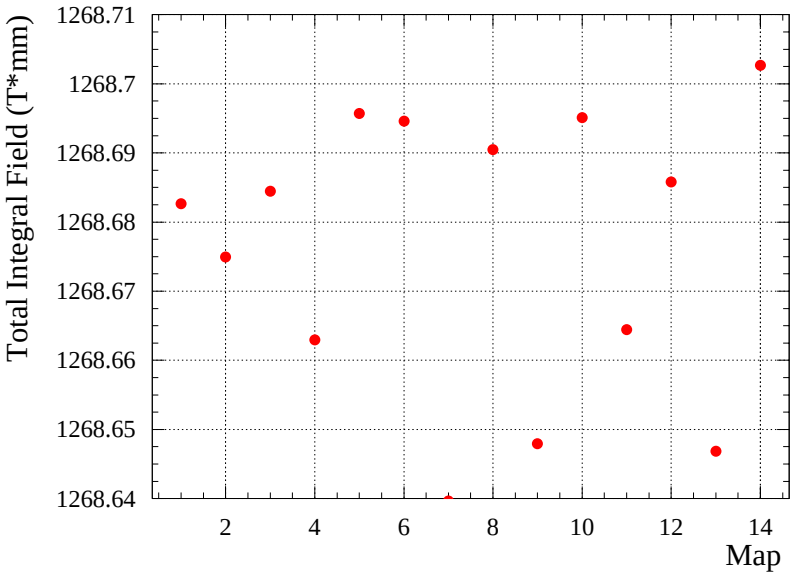


**Figure 7.11**: Total integrals at 100 GeV, laboratory.

obtained. In showing the results of these measurements (Fig. 7.12), no correction for the reference probes was applied. The results lead to the following observations:

- the core integrals show a relative increase in time of $\approx 7 \cdot 10^{-6}$ between the first and the last;
- the total integrals show an oscillation between consecutive maps and a general tendency to decrease;
- the RMS on the total integrals is anyway of the order of $2 \cdot 10^{-5}$ relative to their absolute value.

Therefore some considerations may be done. First of all it is possible to attribute the general increase of the central field to a thermal drift, even if, knowing the negative temperature coefficient of the magnet, one would not expect an unusual decrease of the temperature during the measurement. Actually this is really the case, as revealed in Fig. 7.13 which refers to some interesting temperatures during the measurements under consideration. The core temperature is slightly decreasing, while the water thermal level (and thus the coil temperature) remain quite stable. This behaviour depends strongly on the initial conditions of the magnet. In this case the dipole was previously excited at 100 GeV; therefore the temperature regulation system lowered the core temperature after the degaussing cycle and the ramp to 44 GeV.
The oscillations in the total integrals may be related to some systematics uncertainties which sometimes rose up during the mapping campaign, concerning the forward and backward direction of the end-field measurements. The consecutive maps considered in Fig. 7.11 are performed by moving the mole in opposite directions. Quite interesting is the slight tendency of the total integrals to decrease which means that, at least with this small thermal change, the end-field contribute with a temperature coefficient which has opposite sign of the one in the core region.

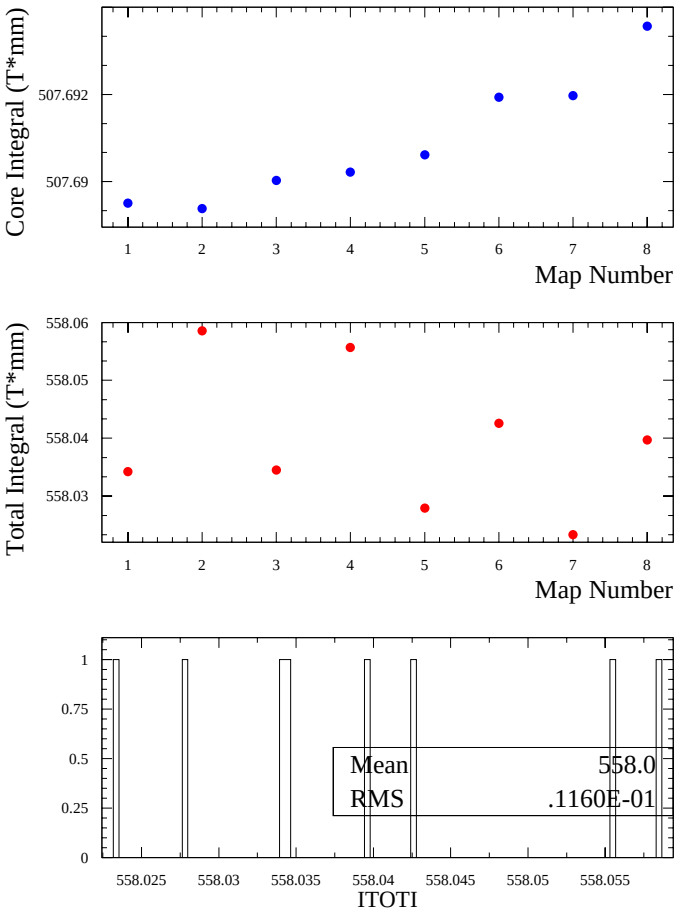


**Figure 7.12**: Total integrals at 44 GeV, laboratory.

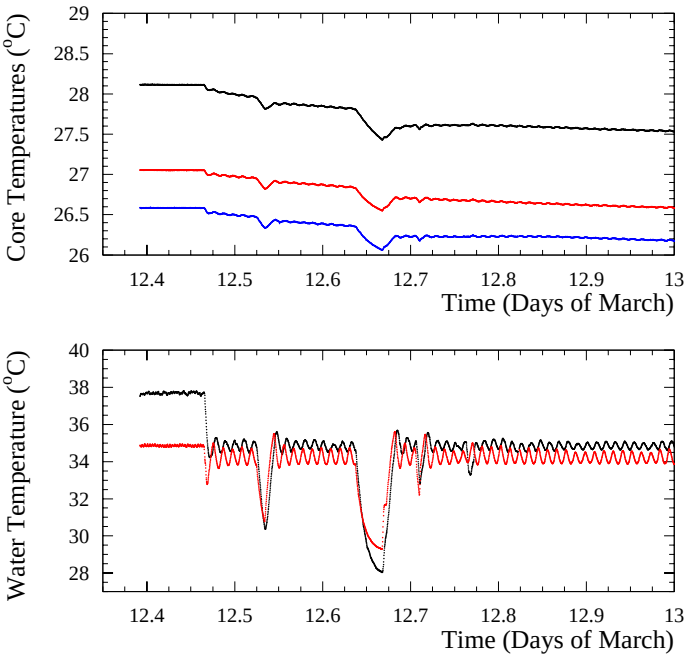


**Figure 7.13**: Thermal behavior during some maps at 44 GeV.

### 7.2.5 Off-centered Maps in the Core Region

As already mentioned, the presence of the two NMR probes on the mapping mole gives two off-centered maps of the magnetic field every time. It is therefore possible to analyse what happens if the beam does not pass through the ideal orbit.
First it is useful to compare the field shape along the dipole length, for the two different transversal coordinates (Fig. 7.14). Then plotting the trend of the difference for the two off-centered scans (Fig. 7.15):

- the difference is neither constant nor statistically distributed;
- the magnetic field shape, which means the magnet structure, seems to be present in it;
- the difference can be considered to have a mean value of $\approx 1 \cdot 10^{-5}$ T which compared to the $\approx 0.2165$ T at 100 GeV counts like a $4.6 \cdot 10^{-5}$ relative change on 1.5 cm of transversal displacement.

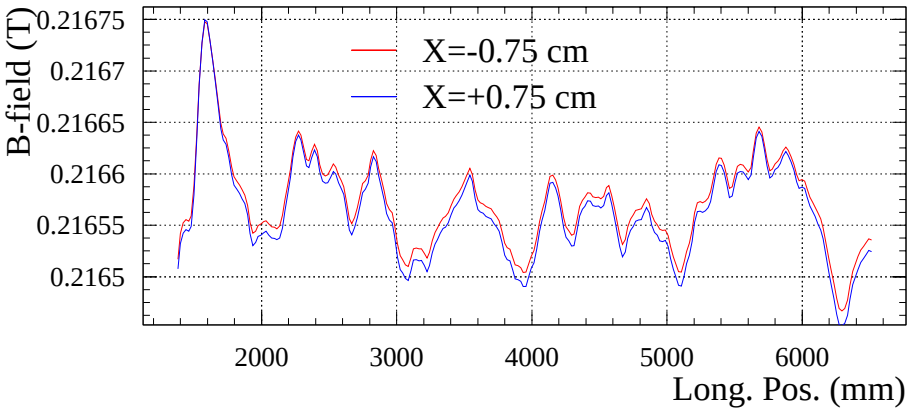


**Figure 7.14**: Two off-centered maps at 100 GeV

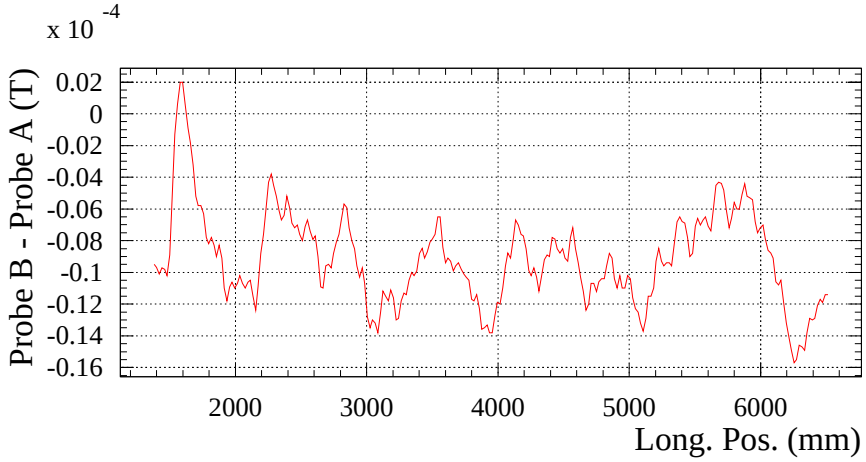


**Figure 7.15**: Local field difference of the off-centered maps at 100 GeV.

The aim is then to check how much this field change is conditioning the total $\int Bdl$ , end regions included. The answer stays in Fig. 7.16, in which the integrals at the transversal position x=0 cm and x=$\pm$ 0.75 cm [6] are shown for six maps at 100 GeV. Looking at the differences between centered

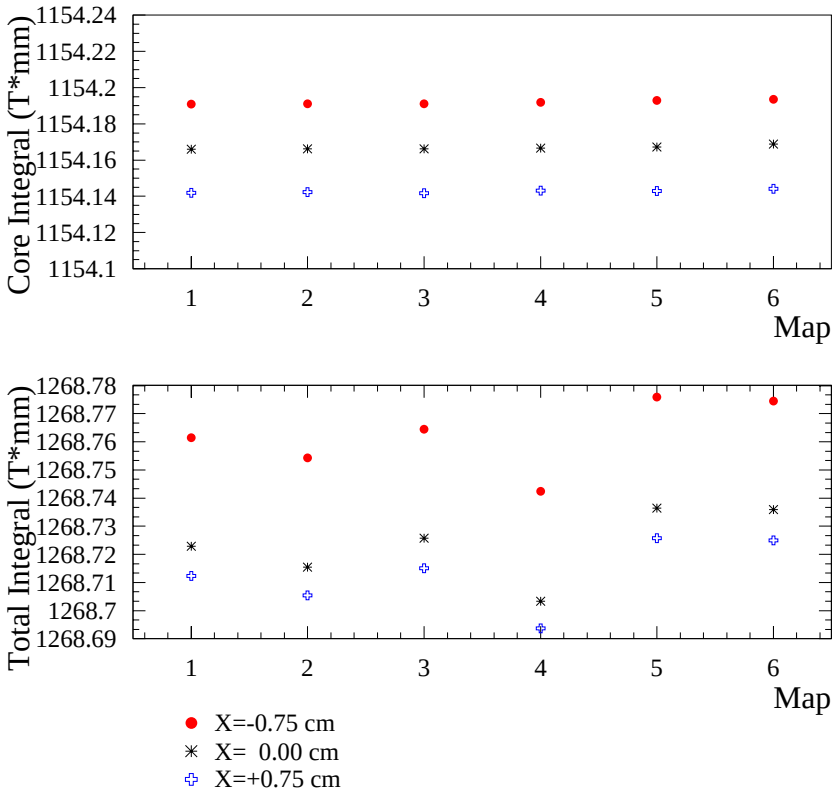


**Figure 7.16**: Core (top) and Total (bottom) Integral Differences on six maps at 100 GeV.

and off-centered core integrals (Fig. 7.17), one sees:

$$
\begin{aligned}
I_{core}^{x=0} - I_{core}^{x=-7.5} &= -0.2533 \cdot 10^{-1} \pm 0.312 \cdot 10^{-3} \\
I_{core}^{x=0} - I_{core}^{x=+7.5} &= +0.2411 \cdot 10^{-1} \pm 0.384 \cdot 10^{-3} \\
I_{core}^{x=+7.5} - I_{core}^{x=-7.5} &= +0.4944 \cdot 10^{-1} \pm 0.495 \cdot 10^{-3} \\
\Longrightarrow \frac{\Delta I_{core}^{\pm 7.5}}{< I_{core}^{100\,GeV} >} &\approx 4.28 \cdot 10^{-5}
\end{aligned}
$$

The last value is, as expected, in good agreement with the relative difference between the local transversal gradient of the field showed previously.
It is not possible to provide transversal scans of the end field, being the induction coil fixed. The actual field monitored by the coil is an average over the coil dimensions, but it was considered acceptable assuming (according to both simulations and local measurements) the field linearly changing over the 2.5$\times$1 cm of the coil. Taking some values from the field calculations and evaluating the integral of one end field at different nominal transversal coordinate (Fig. 7.18) give an estimate of the field behavior. Over the 2.5 cm coil width the relative change on the integral

[6] + means going towards the inside of the ring, - towards the outside.

is $\approx 1.2 \cdot 10^{-4}$ , but the linear trend leads to consider the coil measurement as an average value which is almost equal to the integral in the transversal center. In fact it is clear how in one half of the coil an integral which is smaller than the one seen by the ideal beam orbit is detected, while in the other half a larger field than in the center is measured. Subsequently the two errors cancel each other.

Nevertheless it is useful evaluating how much the total integral changes considering one probe, the other or both (Fig. 7.16, bottom). As for the central field:

$$\begin{aligned} I_{tot}^{x=0} - I_{tot}^{x=-7.5} &= -0.3906 \cdot 10^{-1} \pm 0.277 \cdot 10^{-3} \\ I_{tot}^{x=0} - I_{tot}^{x=+7.5} &= +0.1032 \cdot 10^{-1} \pm 0.386 \cdot 10^{-3} \\ I_{tot}^{x=+7.5} - I_{tot}^{x=-7.5} &= +0.4938 \cdot 10^{-1} \pm 0.475 \cdot 10^{-3} \\ \Longrightarrow \frac{\Delta I_{tot}^{\pm 7.5}}{< I_{tot}^{100\,GeV} >} &\approx 3.89 \cdot 10^{-5} \end{aligned}$$

In the region of interest the central $\int Bdl$ has thus a gradient of $\approx 3.3 \cdot 10^{-6}$ $\frac{\mathrm{T \cdot m}}{\mathrm{mm}}$ at 100 GeV along the transversal direction. Such a slope agrees with the field simulations for the MBI [15]. At 44 GeV the behaviour is the same, still in agreement with the field calculations.

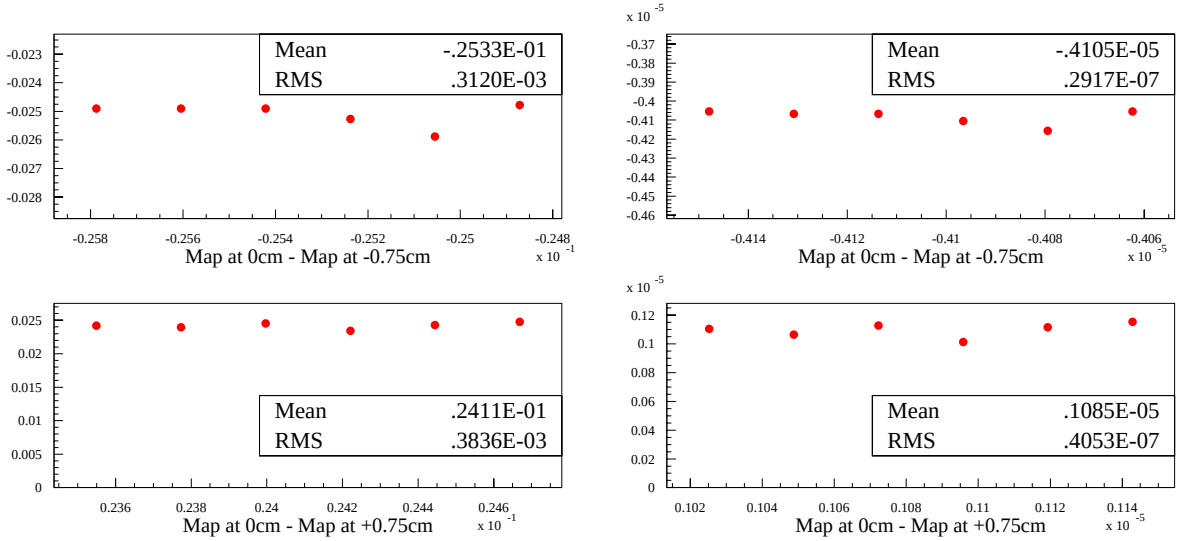


**Figure 7.17**: Differences between centered and off-centered core integrals

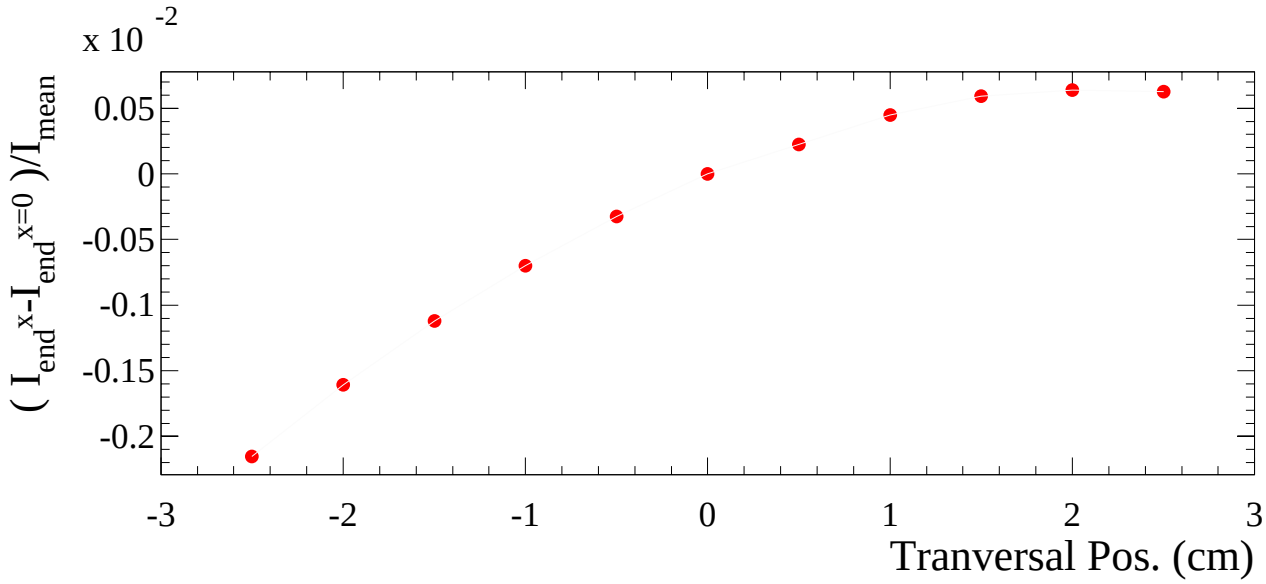


**Figure 7.18**: Simulation of how much the end field integral is changing going off-center transversally.

## 7.3 Measurements in the LEP Tunnel

After the measurements described in the previous section, the magnet was transported to the LEP IP1, lifted down in the tunnel and carried by mean of a crane to the spectrometer location, in proximity of IP3 (Crozet, France).
After the magnet alignment, the same portion of vacuum chamber used in the laboratory was inserted again in the dipole gap and all the equipment mounted and prepared for the last set of maps. Particular attention was taken in restoring as better as possible the conditions of the previous measurements. Hence the same $\mu$ -metal material was wrapped around the pipe in the same location, to guarantee the "zero-field" at equal distance from the magnet edges.
The regulation station for the water temperature was installed in the LEP tunnel and operated in the same conditions of the laboratory measurements (ISR tunnel) and a precise re-positioning of the four fixed probes was carried out after the vacuum chamber insertion. Also the electrical connections were carefully studied in order to have the same ground level connected to the core, the coil, the vacuum chamber and all the electronics used for the mapping.
Two main reasons were left for a possible change in the total integral field:

- a different power converter;
- variations due to some stresses during the transportation.

At the end of this section it will be possible to give an evaluation of such effects.

### 7.3.1 Reference NMRs Reading

The monitoring of the magnetic field in the four chosen fixed locations was carried out with the same procedure as before, running a process parallel to the main one.

**Local Field Change**
During the data analysis an anomaly was found in normalising for the Type 2 probes. The relative difference between the two probes has changed between the two sets of measurements. This is clear at both the beam energies analysed in the laboratory measurements. In Fig. 7.19 there are the distributions of such difference in the LEP and in the ISR tunnels at 100 and 44 GeV.
Looking at Table 7.4 it is possible to conclude that the two probes read field values which changed relative to each other, after the magnet transportation in the LEP tunnel. The relative change amount is $\approx 6.5 \cdot 10^{-5}$ .
Either one or both[7] NMR probes slightly changed position during the replacement in between the two series of measurements, or the magnetic field locally changed, for some reason. This effect can be considered in the data analysis and is not compromising the LEP spectrometer calibration.

[7] The integrals normalisation leads to consistent results assuming that just one probe changed.

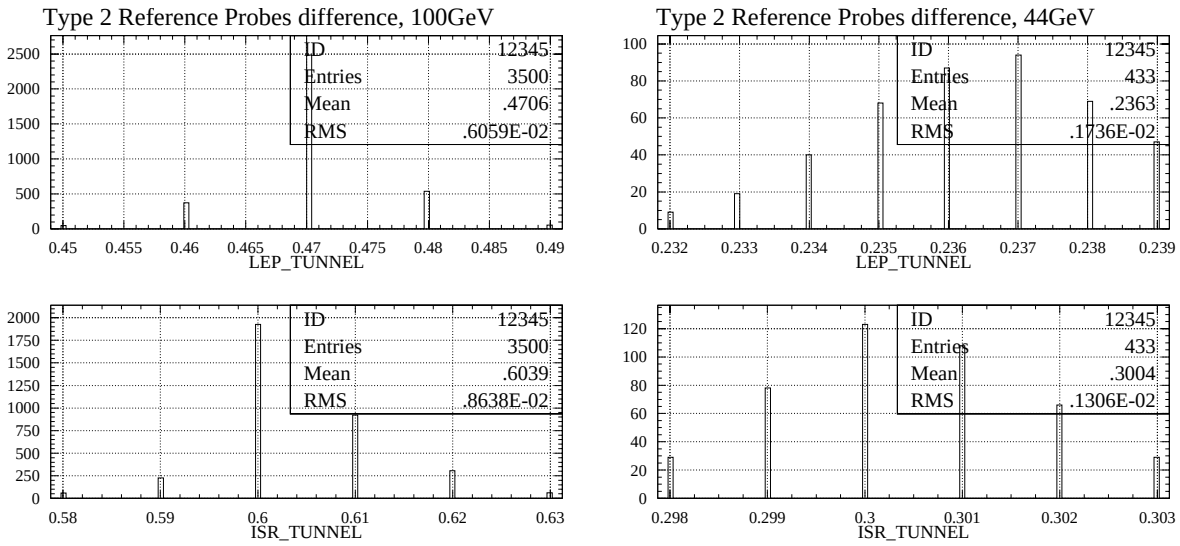


**Figure 7.19**: Distributions of the differences in the Type 2 reference probes at 100 GeV and 44 GeV. Values are in Gauss.

**Table** 7.4: Type 2 reference NMRs differences.

| | FIELD VALUE $[G]$ | NC-CC $^\star$ $[G]$ | COMMENTS |
|---|---|---|---|
| Beam Energy = 44 GeV | | | |
| ISR TUNNEL | $\approx 952$ | $0.3004 \pm 1.3 \cdot 10^{-3}$ | Relative Change: |
| LEP TUNNEL | $\approx 952$ | $0.2363 \pm 1.7 \cdot 10^{-3}$ | $6.7 \cdot 10^{-5} \ \pm 2.3 \cdot 10^{-6}$ |
| Beam Energy = 100 GeV | | | |
| ISR TUNNEL | $\approx 2165$ | $0.6039 \pm 8.6 \cdot 10^{-3}$ | Relative Change: |
| LEP TUNNEL | $\approx 2165$ | $0.4706 \pm 6.1 \cdot 10^{-3}$ | $6.2 \cdot 10^{-5} \ \pm 4.9 \cdot 10^{-6}$ |

$^\star$ NC = Non Connection side, CC = Connection side.

**Temperature Correlation**

During some measurements at nominal beam energy equal to 60 GeV the cooling station parameters were set in such a way that the water temperature started oscillating with a period of about twenty minutes and an amplitude of several degrees. That was an opportunity to study the magnet thermal response. In Fig. 7.20 it is observable how the iron-core temperature and the local magnetic field (measured with one of the fixed monitors) were perfectly following the coil water temperature.

In this case it is possible to calculate a correlation between the water temperature and the local B-field:

$$\begin{aligned} \Delta T^{coil} &\approx 6.5\,(^oC) \\ \Delta B^{local} &\approx 55\,(mG) \\ \rightarrow C_T &\approx 6.5 \cdot 10^{-5}\ {}^oC^{-1} \end{aligned}$$

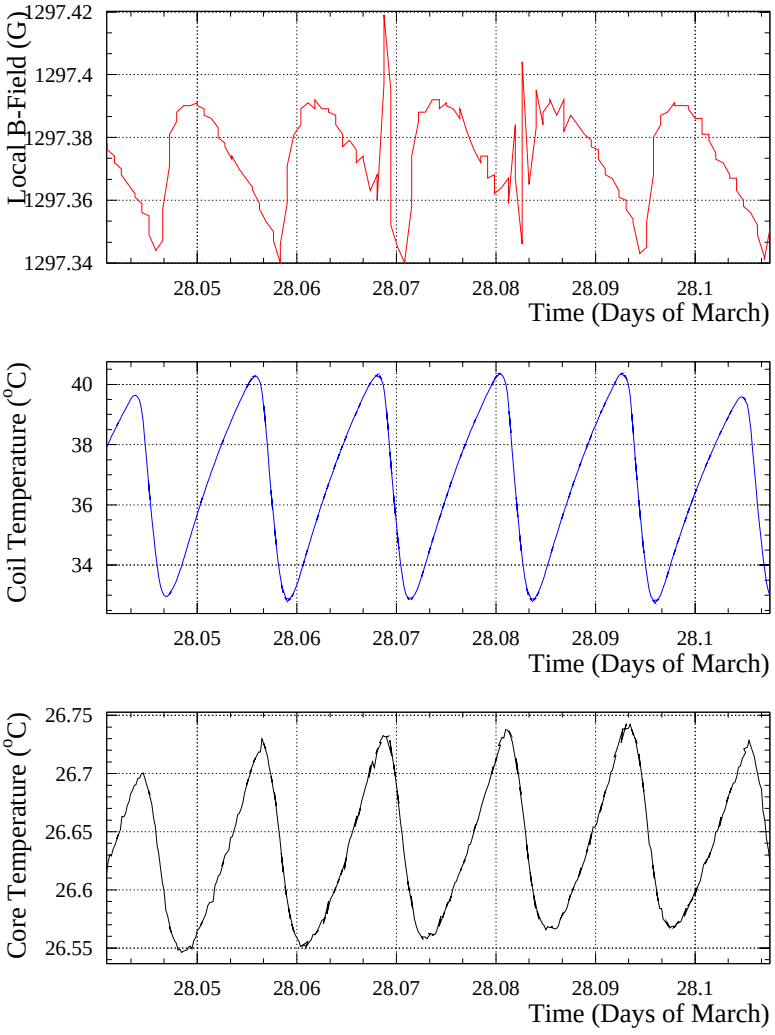


**Figure 7.20**: Local field-Temperature correlation.

### 7.3.2 Total Mapping Results

No changes were introduced in the end field mapping procedure, hence it is possible to pass directly to the total maps analysis. In the LEP tunnel it was possible to perform the measurements scanning more than two energies. In particular 41 GeV, 44 GeV, 60 GeVand 100 GeV have been taken in consideration.
Fifteen maps at 100 GeV are shown in Fig. 7.21, where the good reproducibility of the measurements is deducible by the spread of the total integral values: $\approx 1.9 \cdot 10^{-5}$ .
These maps were performed in different days. The several temperatures monitored during the

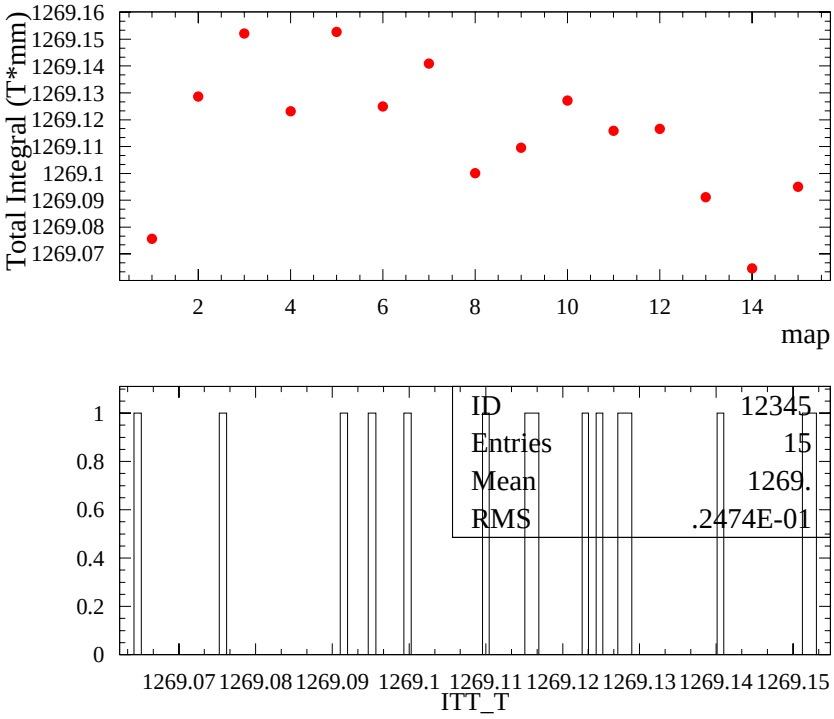


**Figure 7.21**: Total integrals at 100 GeV measured in the LEP tunnel.

measurements did not change of a significant amount during one measurement, but of course could be different in different maps, depending on the magnet previous "history" (maps at another energy, degaussing cycles, thermal stabilization, etc . . . ).
A possible analysis consist in figuring out a mean thermal status of the magnet during the map time. In Fig. 7.23 some temperatures are presented for the fifteen maps at 100 GeV described above.
A number of temperature probes (PT100) has been installed in several locations of the LEP spectrometer. In particular the magnet temperature is monitored in five different sections. For each section the probes are placed inside, above and on the back of the magnet core, like shown in Fig. 7.22.

The results in Fig. 7.21 are computed after a correction, using a temperature coefficient of $-2 \cdot 10^{-5}$ $^{o}\mathrm{C}^{-1}$ which correspond to the typical iron dilatation factor. Such correction is only of the order of $1 \div 2 \cdot 10^{-5}$ , anyway meaningful in this case, due to the accuracy required for these measurements.

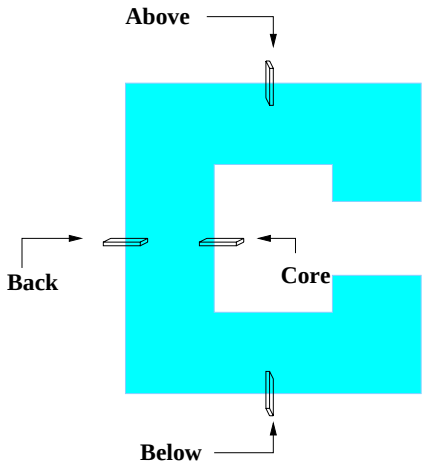


**Figure 7.22**: Temperature monitoring of the magnet.

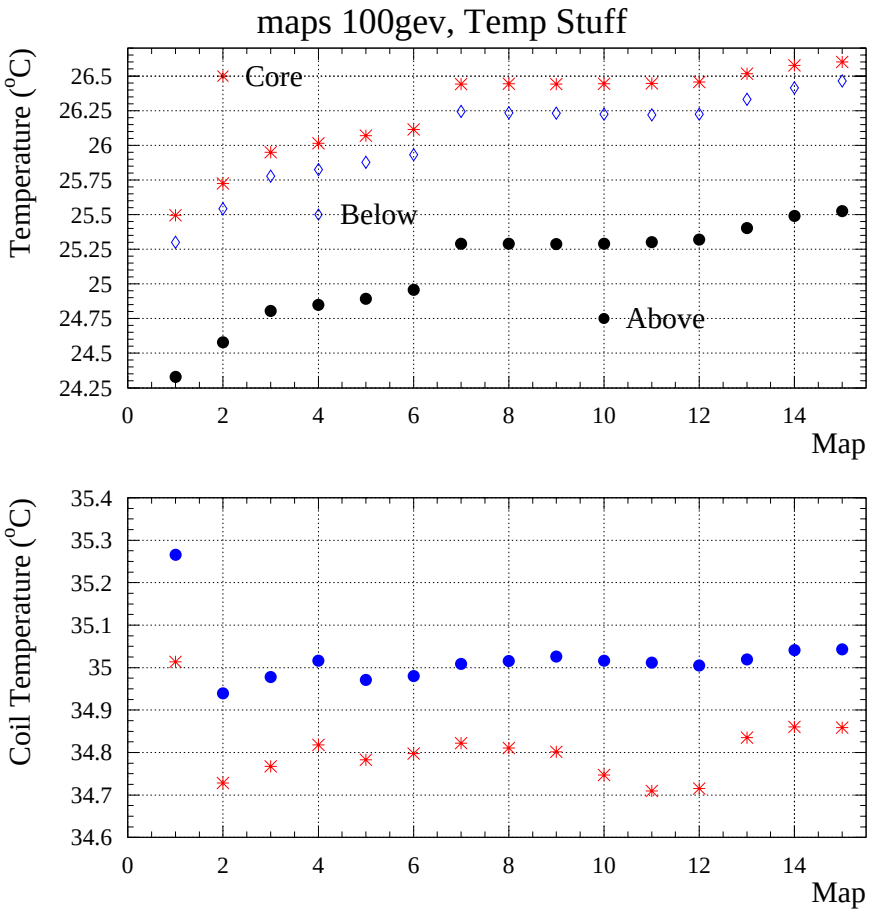


**Figure 7.23**: Temperature behaviour in different locations during the maps at 100 GeV. Each dot represents a mean value during the map time. Core, below and above refer to a magnet section monitoring according to Fig. 7.22

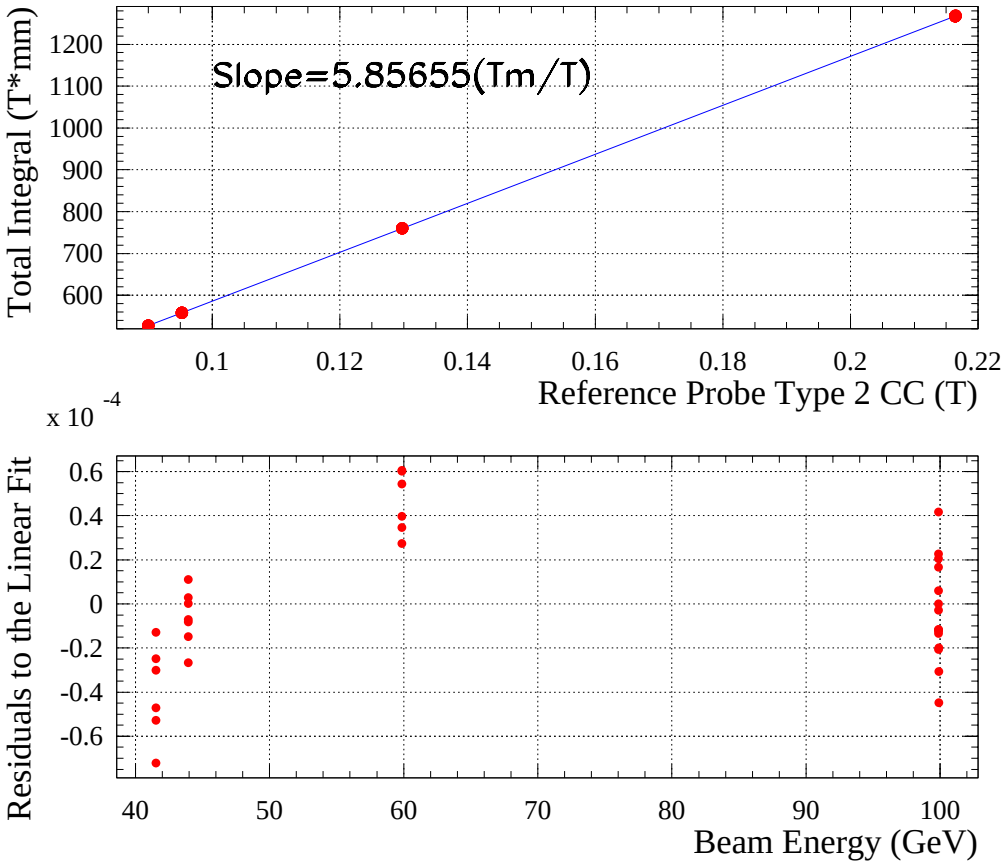


**Figure 7.24**: Linear fit of all the maps performed in the tunnel as function of one of the 4 reference NMR probes (Top). The bottom plot shows the relative residuals to the fit at the correspondent beam energies.

Similar plots can be done for every beam energy level analyzed. The best way to resume all the measurements is showing all the measurements in one plot and performing a linear fit for all the integrals, as function of the fixed NMR probes. In Fig. 7.24 the result of the fit is shown. The residuals represent the relative distance of each map from the ideal fit.
The bended shape of the plot means a non perfect linearity between the local field value and the total integral. This is an already known effect which is not scaring once it is taken into account.
Projecting the residuals to the linear fit on the vertical axis means plotting a distribution of the error in the integral prediction through the reference probes, including the non linearity effect. Such distribution is displayed in Fig. 7.25. The standard deviation is $\approx 3.1 \cdot 10^{-5}$ . The actual error is reduced to the RMS of the field integrals at the single beam energies when the non linearity is taken away. For the beam energy calibration aims, the shape of the residuals to the linear fit suggests to consider a ratio $\int Bdl \, / B_{ref\_probes}$ which is not constant with the beam energy, but following a curve proportional to the residuals to the linear fit.
A similar analysis takes to the same results when referring to the other fixed NMR probes.

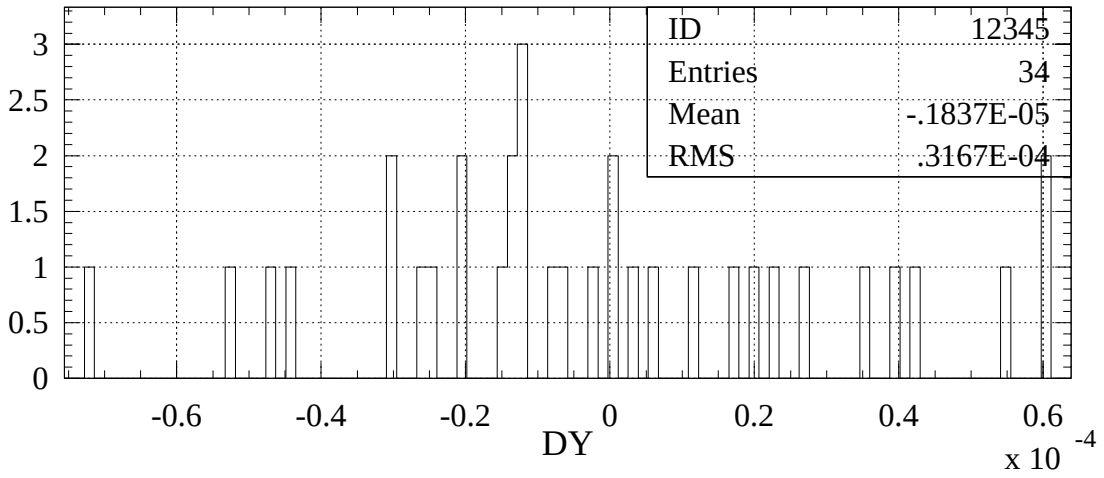


**Figure 7.25**: Distribution of the residuals of the linear fit in Fig. 7.24

### 7.3.3 Off-centred Maps in the Core Region

As in the previous measurements, the presence of two NMR probes on the charriot allowed a constant monitoring of the field in the core region at two different transversal coordinates, 2.5 cm distant. The result and relative considerations are exactely the same as in the laboratory measurements (see Section 7.2.5).
During the LEP tunnel mapping campaign it was also decided to performe a few maps at a *vertical* position displaced with respect to the ideal beam orbit. Two 4 mm thick plates were mounted on both sides of the charriot between the wheels support and the central plate where the NMR probes and the induction coil were fixed. Therefore the field monitors were at a +4 mm nominal vertical position.
Seven vertically off-centred maps at 100 GeV are shown in Fig. 7.27, togheter with the integrals along the ideal beam trajectory. The first three plots are the end field, the core and the total integrals for both the centred[8] and vertically off-centred maps. The plot on the bottom represent the distribution of the difference between the total integrals at the two different vertical coordinates. It is thus possible giving an estimate of the error on the integral relative to a vertical offset of the beam.
On four millimitres:

$$\begin{aligned} \Delta_{mean} &= 1.7 \cdot 10^{-2} \pm 1.9 \cdot 10^{-2} \ (\mathrm{T \cdot mm}) \\ \Rightarrow \Delta_{max}^{relative} &= \frac{1.7 \cdot 10^{-2} + 1.9 \cdot 10^{-2}}{1269} \frac{(\mathrm{T \cdot mm})}{(\mathrm{T \cdot mm})} = 2.8 \cdot 10^{-5} \end{aligned}$$

which leads to a:

$$\Delta_{max}^{vert-offset} = 7.1 \cdot 10^{-6} \ /\mathrm{mm}\,.$$

[8]Seven maps realized on the ideal orbit are taken as “reference”, they lay within the gaussian error of all the maps done at 100 GeV in the centre of the beam pipe.

**Measurement Sensibility on Off-centered Maps**

Few simple geometrical considerations allow a better understanding of the measurement system sensibility to the magnetic field horizontal and vertical gradients.

The NMR probes always detect the real B-field vector magnitude,no matter of its possible misalignment from the ideal vertical dipole field. The plots in Fig. 7.26 show the vector representation of the field in presence of a quadrupole component which introduces a vertical or a horizontal gradient. The horizontal quadrupole component $\partial B_y/\partial B_x$ and the vertical one $\partial B_x/\partial B_y$ introduce the field changes

$$\frac{\Delta B_{nmr}}{B_{nmr}} = \frac{\Delta B_y}{B_1} \tag{7.1}$$

$$\frac{\Delta B_{nmr}}{B_{nmr}} = \frac{1}{2}\left(\frac{\Delta B_x}{B_1}\right) \tag{7.2}$$

respectively, in which $B_1$ is the dipole component. The NMR probe is thus detecting a horizontal gradient, being $\Delta B_n mr \propto \Delta B_y$.

The instrument is instead not sensible to a vertical gradient, being

$$\frac{\Delta B_x}{B_1} \approx 10^{-4} \implies \frac{\Delta B_{nmr}}{B_{nmr}} \approx 10^{-8}$$

In the end field region the search coil detects only the vertical field component, with an accuracy of $\approx 1 \cdot 10^{-4}$ . Up to $\Delta B_x/B_1 = 1 \cdot 10^{-2}$ the effects on the measurement are negligible.

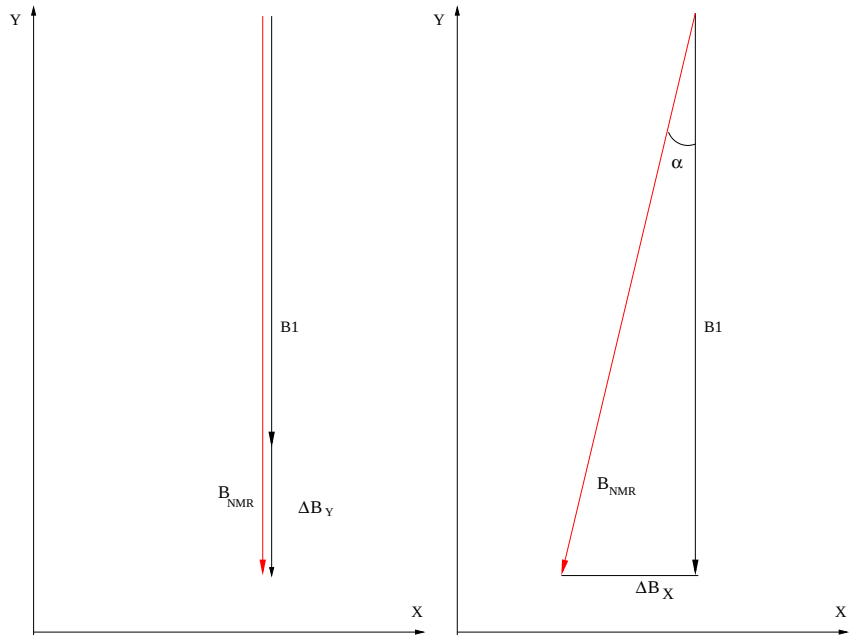


**Figure 7.26**: Field vectors in presence of for a vertical or horizontal quadrupole component.

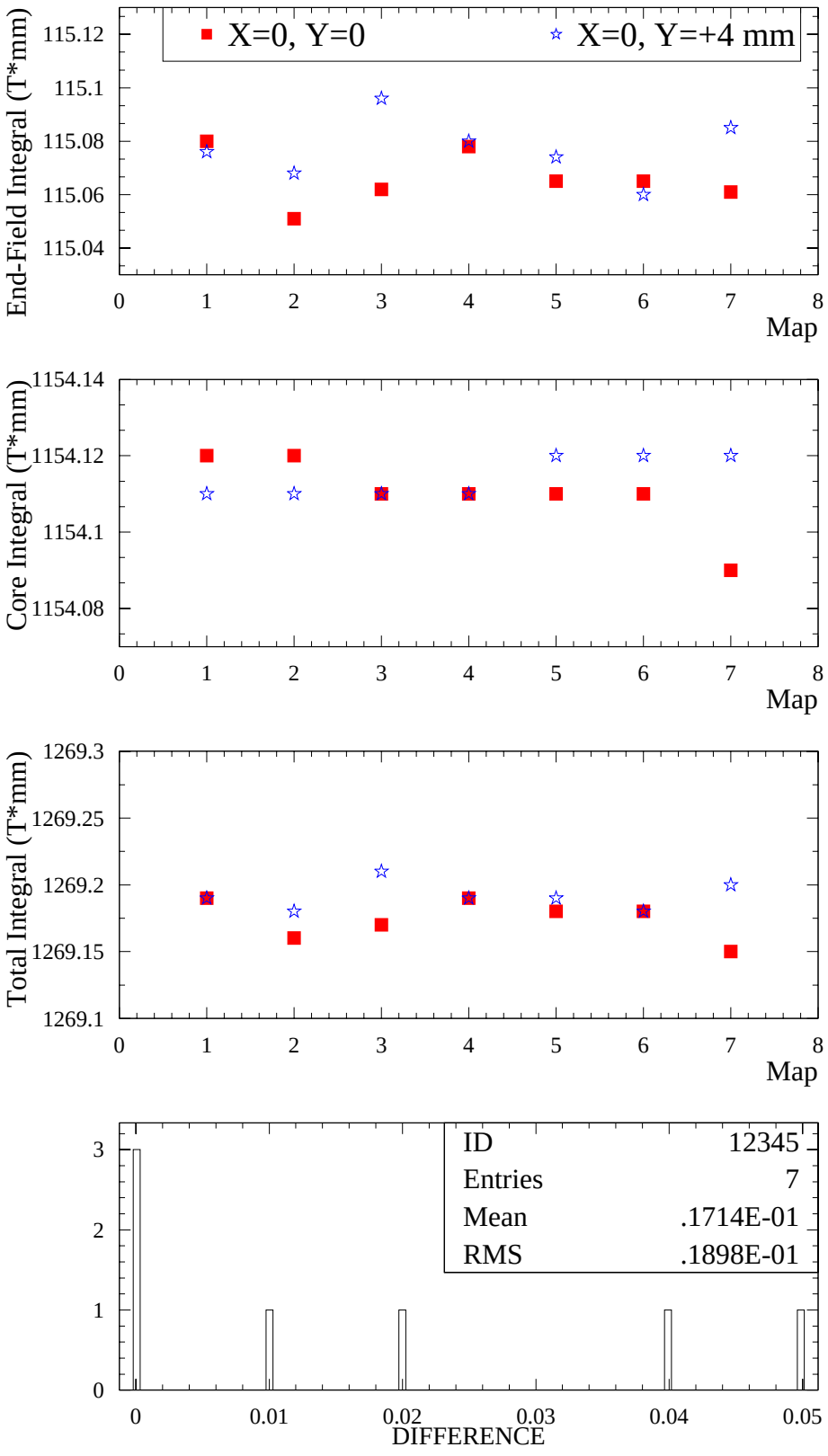


**Figure 7.27**: Effect of a vertical offset of the beam on the field integral

## 7.4 Measurements Comparison

The main purpose of the measurements in the LEP tunnel was to check possible effects of the transportation of the magnet from the test bench at ground level to LEP IP3, where the spectrometer is located.
At the end of the mapping campaign three separate set of maps were available: the measurements performed with the movable arm test bench, the ones executed in the laboratory (ISR tunnel) with the mole running in the vacuum chamber and the last maps done in the LEP tunnel before the end of the machine shut-down.
In comparing the "arm" and the "mole" measurements, it is possible to compare not only eventual changes in the magnet properties due to mechanical stresses or environmental conditions, but also cross-check two kind of measurements consisting in different procedures. The presence of the beam pipe during the "mole" maps must be taken into account as a possible cause of field variations.

### 7.4.1 Mole Laboratory-LEP Tunnel Measurements

It is now possible making some comparisons between the results achieved in each set of maps. First it is possible to check the total integrals at beam energy equal to 100 GeV, trying to fit both the ISR tunnel and the LEP tunnel measurements. Again the linear fit is applied on the total integrals as function of the reference NMR probes average values during each map. In Fig. 7.28 a sketch of the fit and the related residuals is shown.
The order of magnitude of the residuals ($3 \div 4 \cdot 10^{-5}$ ) tells that the two set of measurements do not disagree. If then such residuals are projected on the vertical axis, it is possible to give an estimate of the error committed in predicting the integral reading the reference NMR probes. The distribution of such error is shown in Fig. 7.29. The outcome is:

$$\overline{\epsilon}^{100\,GeV} = (0.88 \pm 2.21) \cdot 10^{-5} \tag{7.3}$$

The same result was obtained considering the other reference probe working at this values of excitation current, the probe Type 2 on the non connection side of the magnet (always referring to the layout described in Fig. 7.1).
An analog approach applied to the beam energies between 41 GeV and 100 GeV gives an overview about the consistence of all the maps executed with the mole setup. Taking again a mean value for the fixed NMR probes for each map, it is possible to fit all the integrals as function of the reference monitors, this time covering all the range of beam energies.
The Type 2 fixed NMR probes were locking at all the energies, so the two of them can be taken as reference for the linear fit. The plots in Fig. 7.30 and Fig. 7.32 display the fits and the related residuals computed for the Type 2 NMR probes, while the plots in Fig. 7.31 and Fig. 7.33 instead show the distributions of the residuals, whose mean values are:

$$\overline{\epsilon}^{All\_En}_{Probe2CC} = (0.18 \pm 2.85) \cdot 10^{-5} \tag{7.4}$$
$$\overline{\epsilon}^{All\_En}_{Probe2NC} = (0.72 \pm 2.71) \cdot 10^{-5} \tag{7.5}$$

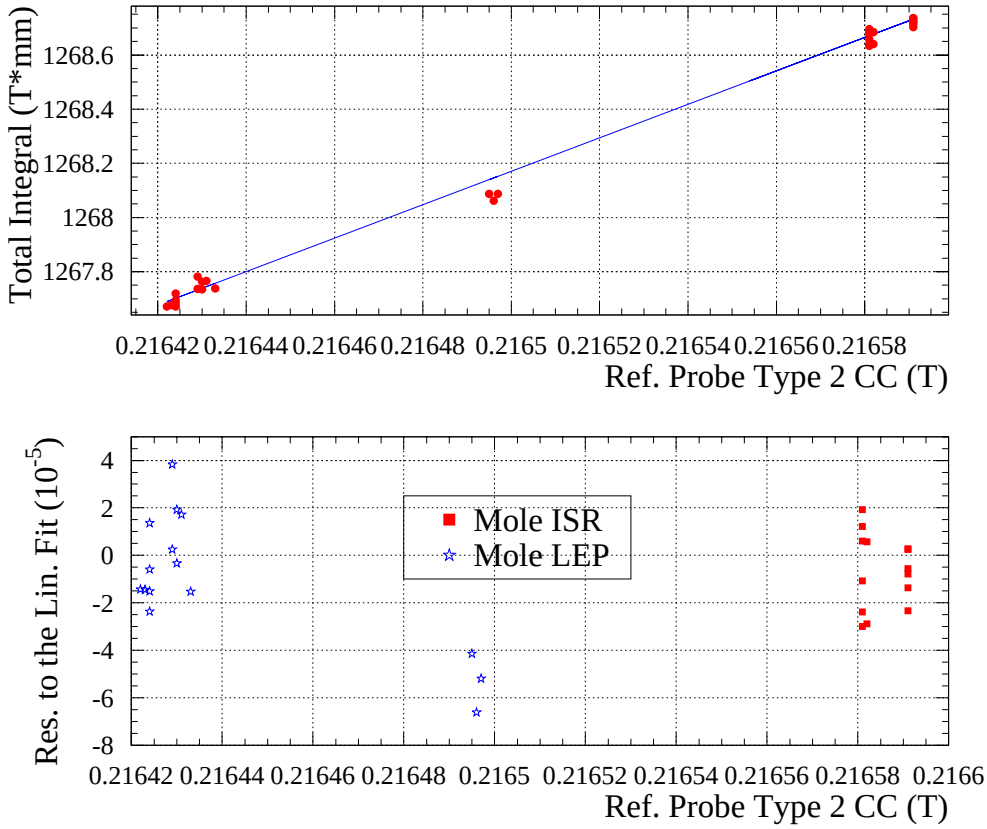


**Figure 7.28**: Linear fit and related residuals for the maps performed in the laboratory and in the LEP tunnel at beam energy equal to 100 GeV.

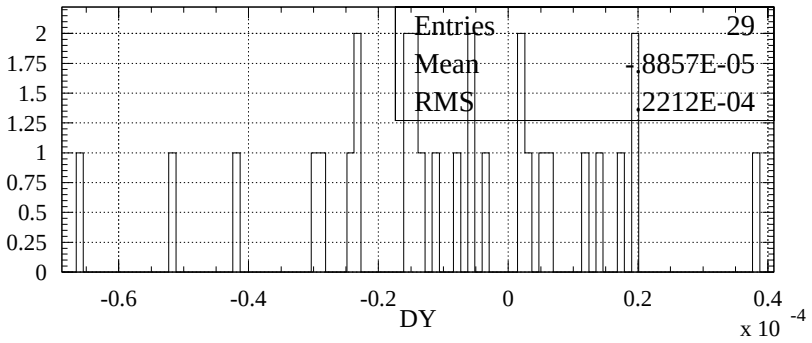


**Figure 7.29**: Distribution of the residuals of Fig. 7.28 as an estimate of the error in the integral prediction through the local B-field monitoring.

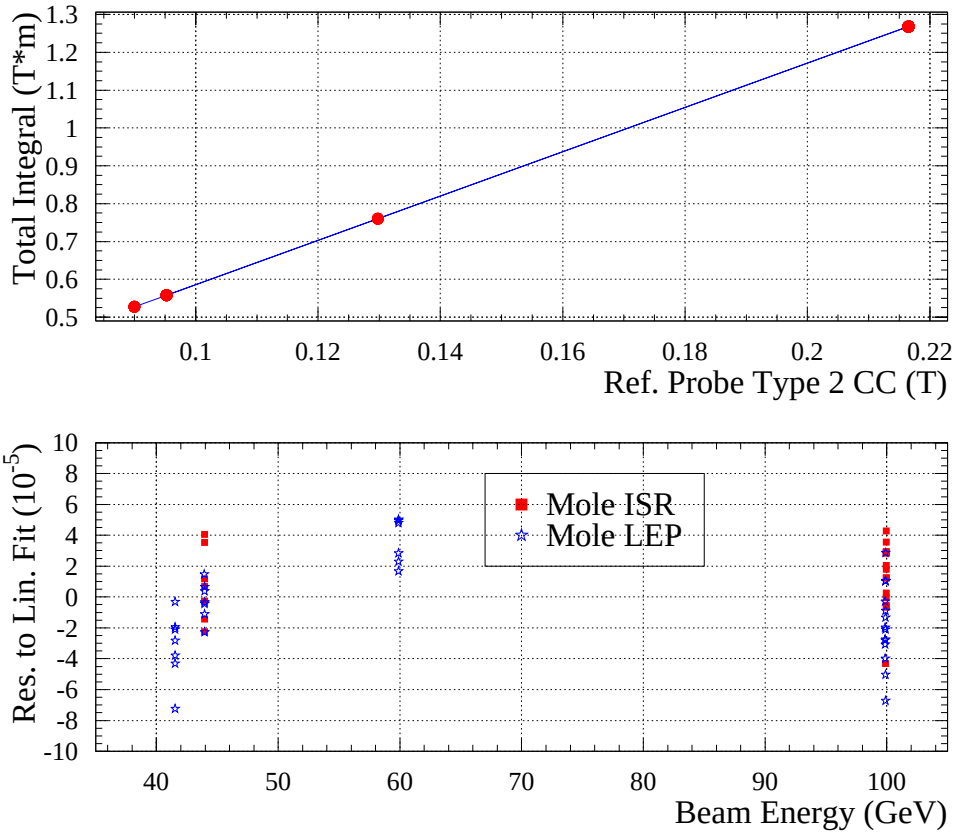


**Figure 7.30**: Linear fit and related residuals for the maps performed in the laboratory and in the LEP tunnel at all the energies, taking the NMR probe Type 2 CC as reference..

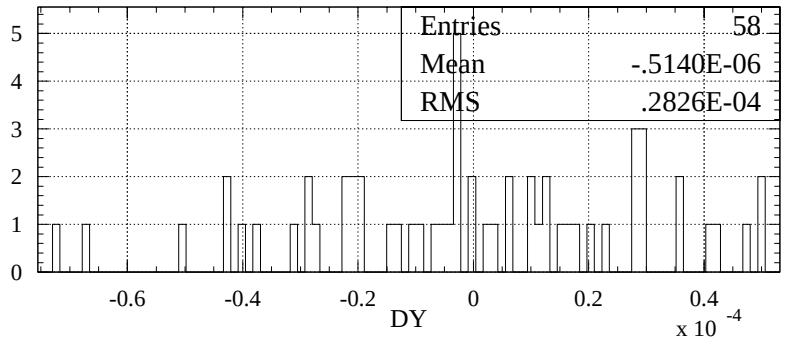


**Figure 7.31**: Distribution of the residuals of Fig. 7.30 as an estimate of the error in the integral prediction through the local B-field monitoring.

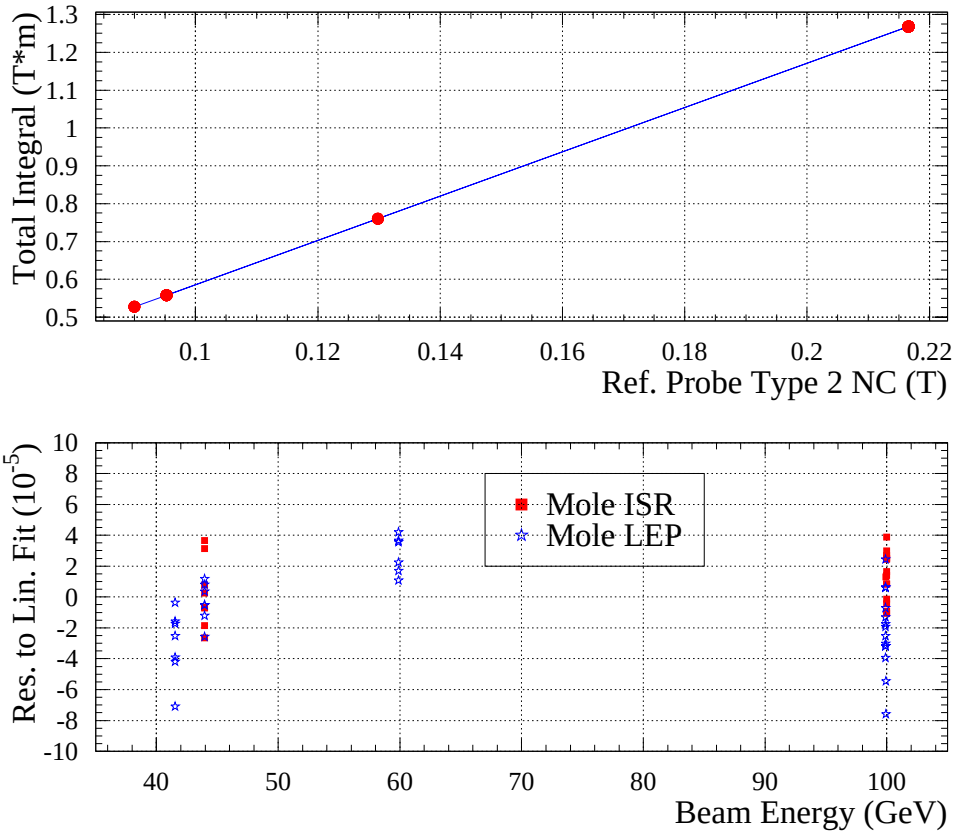


**Figure 7.32**: Linear fit and related residuals for the maps performed in the laboratory and in the LEP tunnel at all the energies, taking the NMR probe Type 2 NC as reference..

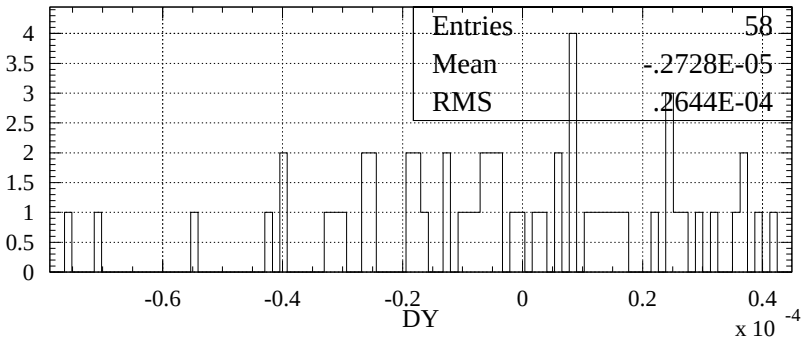


**Figure 7.33**: Distribution of the residuals of Fig. 7.32 as an estimate of the error in the integral prediction through the local B-field monitoring.

### 7.4.2 Arm-Mole Measurements

The ultimate data analysis concerned the comparison between the mole measurements and the maps performed in the laboratory (see Section 3.2.3) before the magnet equipment and displacement in the spectrometer situ. Such analysis is again summarized by computing the residuals of the linear fit *reference probes vs. total integral*. In Fig. 7.34 the linear fit referred to one of the two Type 2 reference NMR probes is presented with a plot of the residuals. The projection of the residuals on the vertical axis provides an information which can be taken as global:
an estimate of the error one commits in predicting the total magnetic field using a calibration based on all the available maps (arm measurements in the laboratory, mole maps in the laboratory and mole maps in situ) at all beam energies.
In Fig. 7.35 the distribution of such residuals is shown. The error can be predicted to be

$$\overline{\epsilon}^{All}_{Probe2NC} = (0.79 \ \pm \ 2.7) \cdot 10^{-5} \tag{7.6}$$

In this distribution two slightly shifted peaks can be noticed. It is an effect that which is due to a group of maps whose residuals are larger, but reproducible. They are a series of measurements performed with the carbon-arm setup in the laboratory during some tests of the temperature regulation system. The cooling water temperature has been forced to be at ten degrees higher than the normal operation conditions.
It is finally worth underlining how this last plot resumes all the efforts put in the mapping of the spectrometer dipole magnet. The results include two different measurement systems (carbon-fiber-arm and travelling mole), two different test sites (laboratory and LEP tunnel) and three different mapping periods. The final value of the error estimate is considered within the requirements for the aims of the LEP beam energy calibration.

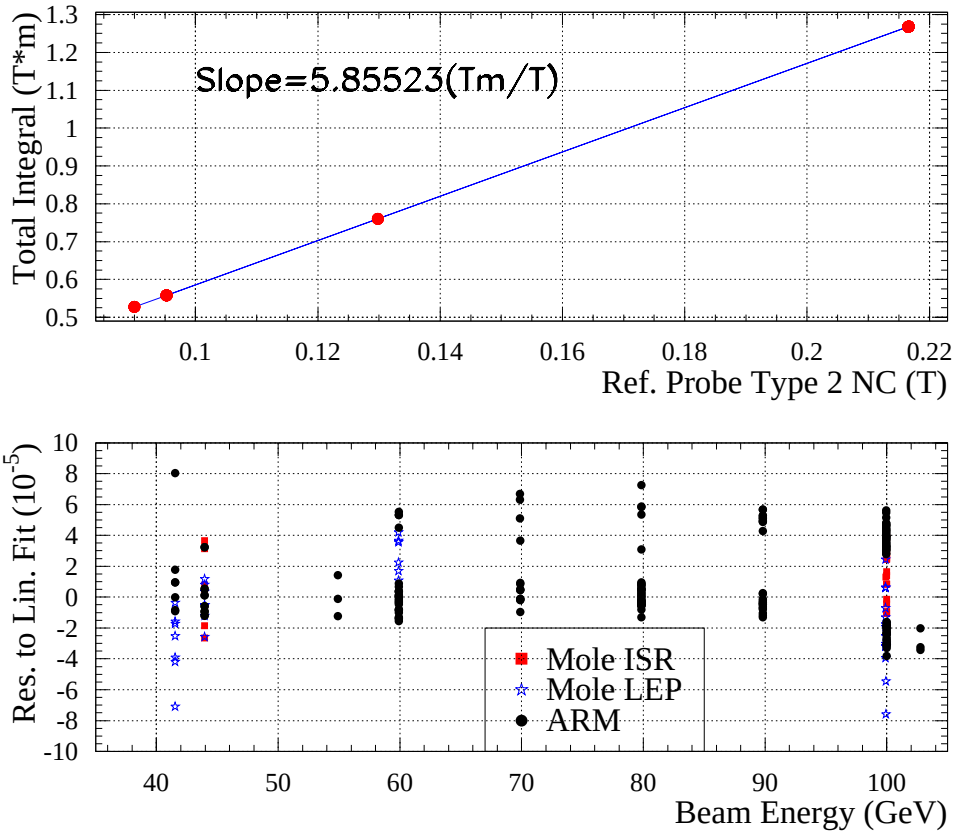


**Figure 7.34**: Linear fit and related residuals for the maps performed with the moving "arm" and the "mole" at all the energies, taking the NMR probe Type 2 NC as reference.

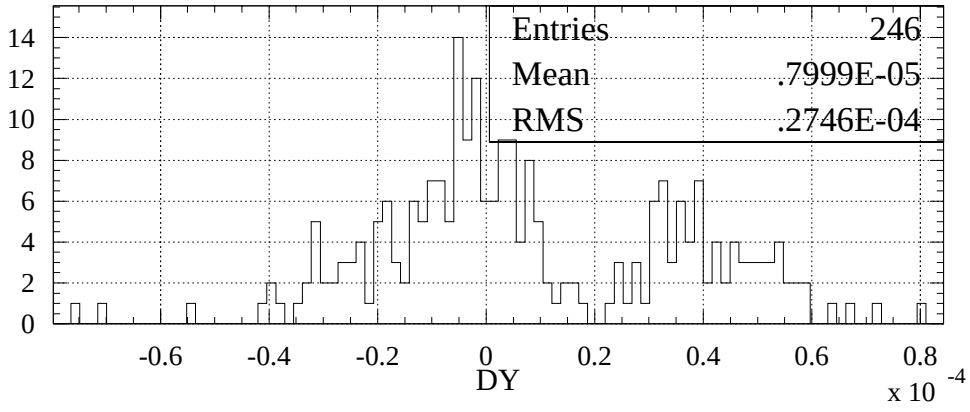


**Figure 7.35**: Distribution of the residuals of Fig. 7.34 as an estimate of the error in the integral prediction through the local B-field monitoring.

# Chapter 8

# Conclusions

This thesis has primarirly dealt with the problem of the beam energy determination in the LEP storage ring at CERN, focusing on the introduction of a new in-line spectrometer.
The spectrometer measurement is based on the determination of the bending magnetic field and of the beam orbit. The accurate determination of the dipole field along the magnet was the primary task for a successful operation of the setup.

A measurement wagon carrying nuclear magnetic resonant probes (NMR) and a search coil was designed and constructed. A laser distance interferometer was used to measure the relative location of the measurement wagon and four fixed NMR probes were used to monitor field variations.

The full automation of the processes and the possibility of transporting the instrumentation from the laboratory to the LEP tunnel made the mapping mole the most importnat tool to determine the stability of the integrated field predictions.

Extensive tests in the laboratory allowed the optimization of the measurement system parameters and of the mapping procedures, in order to reach the highest possible immunity against systematic and stochastic errors.

This setup full automation included accurate instrument recalibration procedures in order to allow uninterrupted measurement durations of several days. The setup was commissioned on a standard LEP dipole magnet to optimise the measurement strategy and so to be able to execute the spectrometer magnet measurements in an limited period of time.
The measurements on the spectrometer dipole were executed with the magnet in the laboratory and in the LEP tunnel. The laboratory measurements were compared with measurements obtained with a completely different setup. The environmental conditions were varied and the full operating parameter range was scanned.
A relative accuracy in the centre of the magnet of few $10^{-6}$ was reached. Including the fringe field contributions, the accuracy dropped to few $10^{-5}$. The comparison of the results from the two different measurement setups and the laboratory and LEP tunnel measurements result in relative differences well below $10^{-4}$.

The final relative uncertainty on the prediction of the total magnetic field integral during the operation of the spectrometer is within $3 \cdot 10^{-5}$, low enough to fulfill the requirements of the LEP beam energy calibration.

The LEP spectrometer is at the moment used as an alternative and independent method for the LEP energy calibration and the preliminary results looks promising.

# Bibliography


[1] M.A. Geitz. Investigation of environmental effects on the LEP beam energy. Thesis, 1996. Physikalische Institute RWTH, Aachen.

[2] C.Bovet et al. A selection of formulae and data useful for the design of a a.g. synchrotron. Technical Report CERN MPS-SI DL/70-04, CERN, 1970.

[3] Metrolab Instruments S.A. High precision NMR teslameters. Technical Specifications, Geneva. Also available @ http://www.metrolab.com.

[4] L.Arnaudon et al. Accurate determination of the LEP beam energy by resonant depolarisation. Technical Report CERN SL/94-71, CERN, 1994.

[5] F.Sonneman. Increase of spin polarisation for energy calibration at LEP . Diploma Thesis, 1998. Physikalische Institute RWTH, Aachen.

[6] The LEP Energy Working Group. Calibration of center-of-mass energies at LEP I for precise measurements of z properties. Technical Report CERN SL/98-12,CERN-EP/98-40, CERN, 1998.

[7] Bravin E. et al. Model of dipole field variations in the LEP bending magnets. Technical Report SL-Note 97-046 BI, CERN, PS/BD, 1997.

[8] L.Arnaudon et al. Effects of terrestrial tides on the LEP beam energy. Technical Report CERN SL/94-07 BI, CERN, 1994.

[9] G. Brun et al. A newly observed effect affects the LEP beam energy. 5th European Particle Accelerator Conference EPAC 96, Sitges, Spain, 1996.

[10] Bravin E. et al. The influence of train leakage currents on the LEP dipole field. Technical Report SL-Note 97-047 BI, CERN, 1997.

[11] Assmann R. et al. Observation of radiative spin-polarization at 60.6 GeV. Proceedings of the Particle Accelerator Conference, 1999, New York.

[12] The LEP Energy Working Group. Evaluation of the LEP center-of-mass energy above the w-pair production threshold. Technical Report CERN SL/98-73,CERN-EP/98-191, CERN, 1998.

[13] J.Prochnow et al. Performance of wire position sensors in a radiation environment. Technical Report Grenoble, IWAA99, CERN, 1999.

[14] The Spectrometer Working Group. The LEP spectrometer project, summary notes of the $18^{th}$ meeting held on August 06, 1998. CERN.

[15] M. Sassowsky. Magnetic field calculations for the LEP spectrometer project. Technical Report SL-Note-99-011 MS, CERN, SL/MS, 1999.

[16] Drawing 02-p81-d1, TESLA Engineering Limited, Storrington, Sussex RH20 3EA, England.

[17] The LEP II team. LEP design report, vol.iii. Technical Report CERN AC/96-01, CERN, 1996.

[18] K.N.Henrichsen. Classification of magnetic measurements methods. CERN Accelerator School, Montreux, Switzerland, 1992.

[19] F.Bloch. Physics Review 70. Stanford University, 1946.

[20] E.M.Purcell et al. Physics Review 73. Harvard University, 1948.

[21] W.Clark. Introduction to magnetic resonance and its application to dipole magnet testing. CERN Accelerator School, Montreux, Switzerland, 1992.

[22] R.Prigl et al. A high precision magnetometer based on pulsed NMR. Brookhaven National Laboratory, 1995.

[23] J.Billan. Materials. CERN Accelerator School, Montreux, Switzerland, 1992.

[24] Hewlett Packard. Laser measurement system operator. Operation Manual.

[25] P.Galbraight. Portable digital integrator. Note Tecnique 93-50, AT-MA/PG/fm, 1993. CERN.

[26] P. et al. Galbraith. Jumps in the magnetic field induced by current spikes. Technical Report CERN SL note/93, CERN, SL, 1993.

# Acknowledgements

I would like to thank Prof. Armando Foglio Para who gave me the opportunity to make this thesis work at CERN and continuously followed up the development of the project.

Dr. Bernd Dehning supervised me at CERN and guided me through all the subjects and problems related to my thesis. He always supported me and has been of fundamental help for the results we achieved, also in spending with me long days and nights in the ISR and in the LEP tunnel.

Very special thanks to Enrico Bravin, from whom started the idea of how mapping the spectrometer magnet. His knowledge about physics, magnetic measurements and computing has been really essential for the performance of our measurements, and I will not forget about how he helped me in settling down at CERN and in the Geneva area.

Giuseppe Mugnai made me feel involved in the NMR maintenance at LEP, giving me the opportunity to learn many things about physics and magnetic measurements.

Thanks to Massimo Placidi, always available to share his great knowledge and experience for fruitful discussions about the energy calibration and LEP spectrometer.

Gian Paolo Ferri, with the help of Denis Azzedine, followed all the “mapping mole” development and utilization, solving with great ability many practical details which could have compromised our measurements.

All the people belonging to the LEP Energy Calibration and Spectrometer groups allowed me to learn many new subjects, and I would like to thank in particular Mike Hildreth, Eric Torrence, Guy Wilkinson and Didier Cornuet who have been specially involved in the mapping campaigns.

At last, but not for importance, I am really grateful to all the friends who lived with me such a great period in Geneva. I cannot avoid mentioning Natalie Pocock, John Matheson, Jan Prochnow, Florian Sonneman and Antonio Vergara. Thanks to them I had the possibility to discuss about CERN, LEP or every-day life, anyway learnig and enjoying the time we spent together.

There is no need to mention the friends who always stayed close to me even if a bit distant from Geneva during my permanence at CERN, because such persons will always know how much important they are for me, forever...

And most important of all, thanks to my parents, for how they always supported me during my studies and every day support me for my life ...